COMPUTATIONAL STUDY OF OXYGEN EVOLVING COMPLEX IN PHOTOSYSTEM II

BY HE CHEN

A dissertation submitted to the

School of Graduate Studies

Rutgers, The State University of New Jersey

in partial fulfillment of the requirements

for the degree of

Doctor of Philosophy

Graduate Program in Chemistry and Chemical Biology

Written under the direction of

David A. Case

and approved by

_____

_____

_____

_____

New Brunswick, New Jersey

October, 2018

ABSTRACT OF THE DISSERTATION

Computational Study of Oxygen Evolving Complex in Photosystem II

by He Chen

Dissertation Director: David A. Case

Photosystem II (PSII) of photosynthetic organisms converts light energy into chemical energy by oxidizing water to dioxygen at the Mn_4CaO_5 oxygen evolving complex (OEC). Extensive structural data have been collected from crystal diffraction, EXAFS studies and electron paramagnetic resonance (EPR), but the protonation and Mn oxidation states are still uncertain. A "high-oxidation" model assigns the S_1 state to have the formal Mn oxidation level of (III-IV-IV-III), whereas the "low-oxidation" model posits two additional electrons. Generally, additional protons are expected to be associated with the low-oxidation model.

We first consider structural features of the S_0 and S_1 states using a quantum mechanics/molecular mechanics (QM/MM) method. We systematically alter the hydrogen-bonding network and the protonation states of bridging and terminal oxygens and His337 to investigate how they influence Mn-Mn and Mn-O distances, relative energetics, and the internal distribution of Mn oxidation states, in both high and low-oxidation state paradigms. Optimized geometries are compared to experimental data and to results from earlier computational studies. The bridging oxygens (O1, O2, O3, O4) all need to be deprotonated (O^{2-}) to be compatible with available structural data; while

the position of O5 (bridging Mn3, Mn4 and Ca) in the XFEL structure is more consistent with an OH^- under the low paradigm. We show that structures with two short Mn-Mn distances, which are sometimes argued to be diagnostic of a high oxidation state paradigm, can also arise in low oxidation-state models. We conclude that the low Mn oxidation state proposal for the OEC can closely fit all of the available structural data at accessible energies in a straightforward manner. Modeling at the 4 H^+ protonation level of S_1 under the high paradigm predicts rearrangement of bidentate D1-Asp170 to H-bond to O5 (OH^-), a geometry found in artificial OEC catalysts.

We then investigate the geometric and spectroscopic properties of the S_2 state, using quantum chemical density functional theory calculations, focusing on the neglected low paradigm. Consistent with experiments, two interconvertible electronic spin configurations are predicted, as ground states producing multiline ($S = 1/2$) and broad ($S = 5/2$) EPR signals, for the low paradigm oxidation state (III, IV, III, III) and W2 as OH^- and O5 as OH^-. They have "open" ($S = 5/2$) and "closed" ($S = 1/2$) cubane geometries. Other energetically accessible isomers with ground spin state 7/2, 9/2, or 11/2 can be obtained through perturbations of hydrogen-bonding networks (e.g. H^+ from His337 to O3 or W2), consistent with experimental observations. Calculated ^{55}Mn hyperfine tensors reveal four scalar (Fermi contact) couplings that are consistent with experiments, and calculated hyperfine anisotropies reveal the severe inadequacy of the magnetic dipolar approximation for hyperfine anisotropies. We conclude that the low Mn oxidation state proposal for the OEC can closely fit nearly all the available structural and electronic data for S_2 at accessible energies.

Following S_3 state under the low paradigm can produce three short Mn-Mn distances and ground state $S = 3$ together with two classes of HFCs, but in separate configurations. We find the direction of Jahn-Teller axis of Mn^{III} determines the related Mn-Mn distances and exchange coupling parameters. S_4 state and O–O bond formation mechanism are studied but no pathway with sufficiently low barrier has been found towards peroxide formation. The rearrangement of bidentate D1-Asp170 from (Mn4, Ca) to H-bond to W1 (H_2O) and Ca indicates the possible role of D1-Asp170 as a proton acceptor during the water oxidation.

Finally, we examine a cobalt cubane cluster in terms of peroxide and dioxygen formations. Complete energy profiles have been calculated.

Acknowledgements

David "Dave" A. Case accepted me as his student when I was at the cross road of my academic career after I left another group. Besides his great academic capability, his passion in science, extreme self-discipline and patience also impressed me a lot and boosted my self-esteem significantly. For those, I am grateful to have had him as a mentor. Deep in my heart, one can not ask for a better one.

G. Charles "Chuck" Dismukes, together with Dave, brought me into Photosystem II. As a "Wikipedia" of PSII, Chuck was always able to enlighten me every time I have a question. He is the one who pushed Dave and me to move forward. Without him, I don't know where I would stand now. It's been a great period of study with him. Oh... I still owe him a manuscript which I should finish as soon as I can.

Darrin York constantly provides useful and straightforward suggestions in our meetings. I always admire the way he expressed his ideas and how he made complex things simple and easy. I thank him for all those and investing time in me.

I want to thank Victor Batista for agreeing to be my committee despite his busy schedule.

I owe some former group members many thanks. Iwen Fu, Pawel Janowski, Jesse Johnson and Hung Nguyen, thanks for your help during my early days to get me started. I thank Jason Swails and George Giambasu for his technical support. I also want to thank Chunmei Liu, Jason Deckman, Shashi Rao and Jonathon Gray for casual chatting which greatly eased my pain in research.

At last, love to my parents, my brother, and my girl friend. They are the ones I could always share my feelings with, either good or bad.

Table of Contents

List of Tables

List of Figures

Chapter 1

Introduction

1.1 Photosynthesis and Photosystem II

As the most widespread and successful metabolism on Earth, oxygenic photosynthesis in plants and bacteria plays a central role and forms the energetic base for most life in nature (Figure 1.1). The overall process can be divided into two sets of reactions: the light reaction and the dark, or carbon fixation reaction. The light reaction uses the light energy as the energy driving force and depends upon the generation of a charge-separated state. The excitation energy, generated by absorbtion of actinic photons by an antenna network, is transferred to the chlorophyll-based primary electron donor, which results in a cascade of dark electron transfers[14] and leads to the ultimate reduction of NADP to NADPH. In the dark reaction, NADPH is used to reduce atmospheric CO_2 for incorporation into simple sugars.

Photosystem II (PSII) is the terminal enzyme in light-dependent water oxidation of oxygenic photosynthesis, and found throughout all higher plants, green algae and cyanobacteria. It contains 19 to 26 subunits and an inorganic cluster, denoted the oxygen evolving complex (OEC). The reaction center photochemistry generates an oxidized tyrosine radical denoted Yz$^{\bullet}$ and reduced semiquinone radical. Yz$^{\bullet}$ is bridged *via* its phenolate oxygen to the OEC, and extracts four electrons from it on successive light flashes. This process results in movements of an electron and a 'hole' (the vacancy left by the absence of an electron). The electron is passed to a modified form of chlorophyll called pheophytin, which passes the electron to a quinone molecule (Figure 1.2). The 'hole' is accumulated at the OEC and used in the dissociation of two water molecules to form molecular oxygen and protons (Eq. 1.1), making PSII the only enzyme on earth that is able to split water by the use of visible light. Despite the necessity of

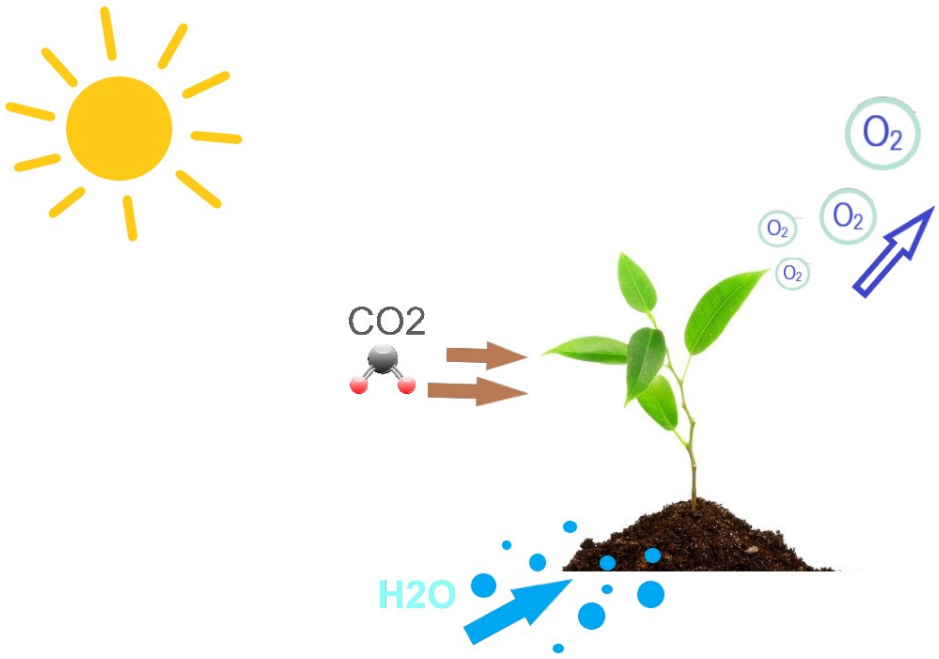

Figure 1.1: Photosynthesis of plant.

oxygen for humans and other aerobes, it is merely a byproduct of photosynthesis. The products that are crucial for the photosynthetic organisms are the protons which help fuel a proton gradient (ΔpH) across the thylakoid membrane that helps provide the energy for ATP production, and electrons which provide reducing equivalents for the carbon fixation reactions.

$$\begin{aligned} 2\mathrm{H_2O} + 4h\nu \rightarrow & 4e^- + \mathrm{O_2} + 4\mathrm{H}^+_{lumen} \\ 2\mathrm{PQ} + 4e^- + 4\mathrm{H}^+_{stroma} \rightarrow & 2\mathrm{PQH_2} \end{aligned} \tag{1.1}$$

1.2 The Oxygen Evolving Complex

The OEC, comprised of $\mathrm{MnOCaMn_3O_4(H_2O)_4}$ (Figure 1.3B), is currently the focus of attention, since it has unmatched high energy-conversion efficiency compared with artificial catalysts derived from cheap and abundant elements[15]. It catalyzes water oxidation, releasing $\mathrm{O_2}$, four protons and four electrons that reduce two molecules of plastoquinone (PQ) to the plastoquinol ($\mathrm{PQH_2}$) (Eq. 1.1). The resulting four successive redox states differ by one-electron each are denoted $\mathrm{S_i}$ (i=0-4), using the nomenclature

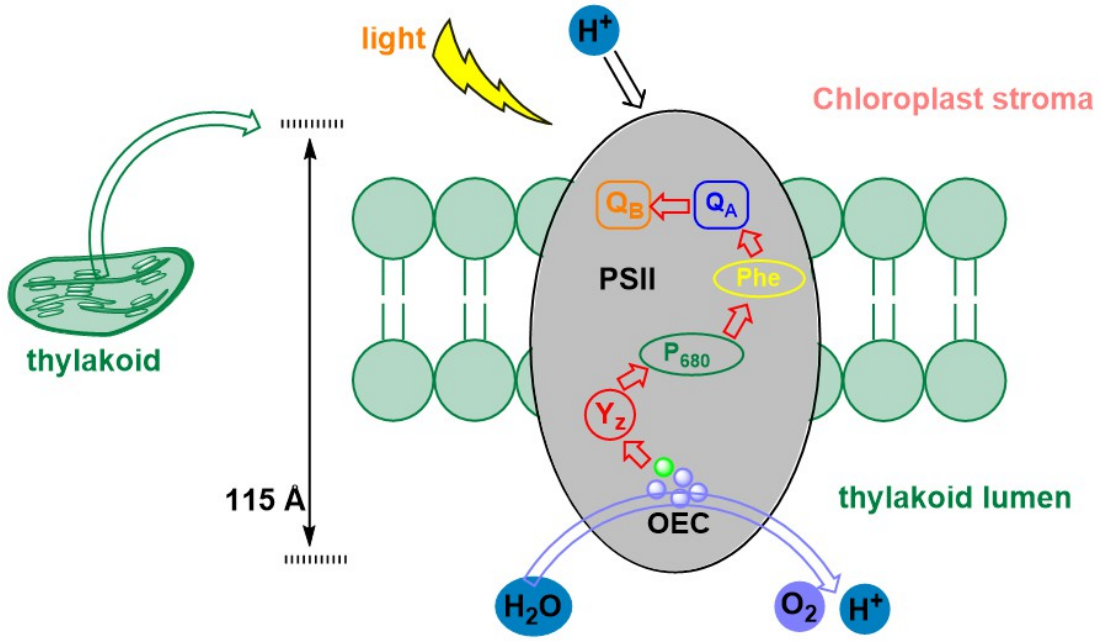

Figure 1.2: Cartoon of the Photosystem II in light reaction. Red arrows connect redox cofactors of the electron transfer chain, including the primary electron donor (P_{680}), the primary pheophytin acceptor (Phe), the primary (Q_A) and secondary (Q_B) quinone acceptors, and, at the center donor side, a a redox-active tyrosine (Y_z) and the oxygen evolving complex (OEC).

originated by Kok *et al.*[8, 9] as depicted in Figure 1.3A. The total number of protons evolved to solution in the cycle is four, but its division among individual S_i state transitions depends upon a number of factors, such as species, pH, temperature and PSII isolation. In *vivo*, the S_0 and S_1 intermediates are dark-stable, while S_2 and S_3 are metastable (few to ten of seconds) and may decay by charge recombination or backward transitions to the dark-stable S_1 state without O_2 production. S_4 is transient and in its productive reaction spontaneously releases one molecule of O_2 and protons upon reforming S_0 to re-initiate the cycle.

A considerable amount of structural data concerning the OEC has been collected from crystallography (XRD)[10, 16, 17, 18, 19, 20], X-ray spectroscopy[21, 22, 23, 24], EPR[25, 26, 27, 28, 29, 30, 31, 32, 33, 34, 3, 35, 36, 4, 37, 38, 39, 40, 41, 42, 6], ENDOR[5, 6, 43] and computational modeling[44, 45, 7, 46, 47]. The XRD structure of the resting S_1 state at highest resolution, 1.9 Å, shows a core comprised of an oxo-bridged heterocubane, $CaMn_3O_4$, that is oxo-bridged to a "dangler" Mn4 connecting the

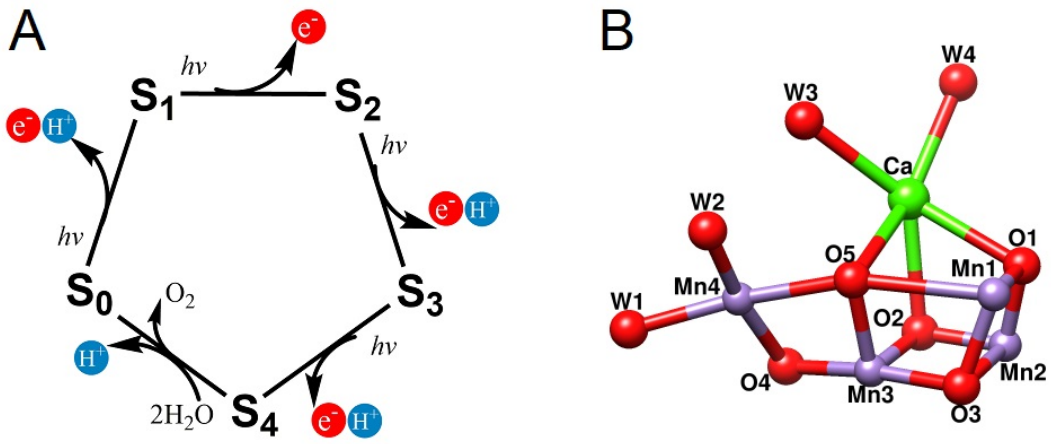

Figure 1.3: (A) notation of the water oxidation (Kok) cycle[8, 9] and (B) 1.9 Å crystal structure of the oxygen evolving complex (OEC) (Mn# 1:2:3:4 using the numbering system of Shen *et al.*[10]).

cuboidal part through one or two oxo bridges (O4 and O5) depending upon conditions (Figure 1B). The structure also reveals four direct water ligands (W1 to W4), two of which are bound to Mn4 and the other two bonded to Ca.

The average oxidation states of the manganese ions have been narrowed to two possibilities, denoted the "high oxidation paradigm" (HOP) and "low oxidation paradigm" (LOP), where the latter has two more electrons (so that the S_1 state has an average formal Mn oxidation state of 3.0). The low paradigm is consistent with photoassembly experiments[48, 49], substrate water exchange kinetics[50], and EPR analysis[32], while the high paradigm (where the Mn ions in S_1 have an average oxidation state of 3.5) is supported by a chemical reduction experiment of PSII particles[51] (in contrast to other experiments[48]), by alternative interpretations of substrate water exchange experiments[52] and by EPR analysis[37]. These alternative oxidation state assignments initially evolved from EPR data of the S_2 state which exhibits a complex multiline signal, representing a spin $S = 1/2$ ground state[25, 32, 4, 6] which was shown to be compatible with magnetic couplings to nMn(III) and mMn(IV) ions, where $n + m = 4$ and n/m is either 1/3 or 3 (refs[32, 53]). Detailed arguments for and against these two alternatives can be found elsewhere[54, 1]. Additional chemical uncertainly arises from the fact that a variety of protonation states are possible for oxygens in the central Mn_4Ca core, and for His337. Much less experimental work has addressed this question

Table 1.1: Short Mn-Mn EXAFS distances R (Å) for the S_1, S_2, S_3 states of the OEC (reconstructed from Ref.[1]).

State	R_{Berkeley}[59]	R_{Berlin}[60, 21, 24]
S_1	2.71, 2.71, 2.79	2.7, 2.7
S_2	2.74, 2.74, 2.74	2.69, 2.74
S_3	2.75, 2.75, 2.79	2.73, 2.73, <2.77

definitively.

1.2.1 Protonation and Oxidation States of the OEC

Although the 1.9 Å XRD data reveals the structure of the catalytic center in great detail, it shows some key differences from theoretical studies[55, 56] and earlier X-ray absorption near edge structure (XANES) and extended X-ray absorption fine structure (EXAFS) spectroscopy[21, 22] data on PSII. X-ray spectroscopies provide geometric structure information in terms of intermetallic distances and extended X-ray absorption fine structure (EXAFS) is believed to be the most reliable data set for the metal-metal separations within the OEC and they are less prone to radiation damage. The EXAFS data sets for different S states are shown in Table 1.1. The EXAFS data sets for S_1 state imply at least two short Mn-Mn distances of about 2.7 Å for S_1[22, 24], which is not observed in the 1.9 Å XRD data. These differences have been ascribed to radiation damage by some groups[46, 56, 57]. A more recent X-ray free electron laser (XFEL) crystal structure by Suga *et al.* reveals the atomic positions of PSII at 1.95 Å resolution[58], and is considered to be more "radiation-damage-free". The 1.95 Å XFEL structure is broadly similar to the 1.9 Å XRD structure, but with some key differences in Mn-Mn distances. In particular, the XFEL structure shows two short Mn-Mn distances, Mn1-Mn2 and Mn2-Mn3, which is consistent with the EXAFS data. Since these Mn-Mn distances are 0.1-0.2 Å shorter than that in the 1.9 Å XRD structure, it is also consistent with less radiation-induced reduction of the Mn ions in the XFEL structure.

Several computational studies have looked at possible protonation and oxidation states of the OEC and compared to the XRD structures in the resting state which is obtained by extended dark adaptation. Knapp and co-workers performed extensive

quantum chemical density functional theory (DFT) calculations to assign the protonation and oxidation states of OEC in the 1.9 Å XRD structure[56]. They screened the structures to reach an agreement with the atomic positions from the 1.9 Å XRD structure and concluded that the 1.9 Å XRD structure is a mixture of states containing reduced forms with the main contribution coming from a non-physiological S_{-3} state (4 electron reduction of initial S_1) in the high paradigm, or a non-physiological S_{-1} state (2 electron reduction of initial S_1) in the low paradigm. These correspond to formal Mn oxidation states of III-III-II-II. On the other hand, Pace and Stranger have argued that an S_1 model in the low paradigm, with oxidation state III-III-III-III (which was not investigated by Knapp), could match the 1.9 Å XRD structure[61].

Neese and co-workers also evaluated models with different protonation and oxidation states with respect to the geometric, energetic, electronic, and spectroscopic properties, and concluded that the entire S state phenomenology can only be accommodated within the high paradigm[1]. They derived their high-paradigm S_1 models from S_2 geometries which were used to explain the two interconvertible S_2 state EPR signals at $g = 2.0$ and $g \geq 4.1$[47]. Their S_1 model has O5 in the form of O^{2-} and the corresponding short Mn-O5 distances don't agree with the XFEL structure (discussed in Chapter 2), leading to a proposal that the XFEL structure may still suffer some photoreduction and/or contain a non-negligible S_0 state contribution. In their examination of S_1 low-paradigm models, they were unable to produce short Mn-Mn distances to match the intermetallic EXAFS-derived distances. Later, Pace and Stranger suggested a S_1 low-paradigm model with O5 as OH^- and oxidation state III-IV-III-II, that was not examined by Neese, and which was able to produce the short Mn-Mn distances consistent with the XFEL structure[62]. A DFT analysis by Shoji also concluded that O5 was most likely protonated in S_1 state[63]. They claimed that the XFEL structures for all the PSII monomers were consistent with a model with O5 (OH^-) and W2 (OH^-) based on the atomic spin density analysis and geometric comparisons to the Mn-Mn and Mn-O5 distances assigned by XRD. However, their discussions were restricted to the S_1 state in the high paradigm.

The debate surrounds the oxidation states of the manganese ions and the protonation states of the ionizable groups within the OEC is still ongoing.

1.2.2 Spectroscopic Properties of the OEC

Introduction to EPR. In the presence of an external magnetic field with strength B_0, the electron's magnetic moment, m_s (determined by the spin quantum number S), aligns itself either parallel or antiparallel to the field, resulting in a specific energy for each alignment due to Zeeman effect[64]. These energy levels lead to the foundations of electron paramagnetic resonance (EPR) spectroscopy, which has been a valuable tool in understanding the oxidation state and chemical environment of paramagnetic substances (characterized by measurements of the g-factor at the center of the spectrum). It depends on the absorption of microwave radiation during electron spin-state transitions of one or more unpaired electrons, i.e. $S \geq 1/2$. Because it involves the detection of unpaired electrons, it is an ideal technique for studying electron transfer systems, such as OEC in PSII. Electron Nuclear Double Resonance (ENDOR) is a combination of electron and nuclear magnetic resonance, whose main application is to resolve hyperfine structure that is unresolved in regular EPR.

We now briefly summarize the experimental data of spectroscopic properties of S_1, S_2, and S_3 states.

S_1 state signals. The S_1 state is diamagnetic ($S = 0$) in the ground state[65], but integer spin excited states of the same spin manifold are accessible. For example, a featureless signal at $g = 4.8 - 4.9$, which is thought to arise from an $S = 1$ state, was reported with width of about 600 gauss[66]. Another S_1 state EPR signal appears at about $g = 12$ with ≥ 18 hyperfine lines with an average splitting of 32 gauss[67], featuring characteristic of a Mn cluster.

S_2 state signals. The S_2 state EPR signals are by far the best characterized of all signals from the OEC. In addition to the multiline signal (mentioned earlier), a higher spin signal centered at $g \approx 4.1$, which has an isotropic appearance with width of 340-360 gauss, is also observed in a variety of sample preparations and has been attributed to $S = 5/2$ or $S = 3/2$ spin states[30, 31, 33, 34, 35, 36]. Experimentally, the $g \geq 4.1$ signals of higher plants varies depending on illumination temperature. For example, at 65 K, the illumination of the $S = 1/2$ state leads to the formation of signals at $g = 10$

Table 1.2: S_i state of dependence of substrate water exchange rates measured by time-resolved membrane inlet mass spectrometry (TR-MISS) in spinach thylakoids and Sr-substituted BBY (reconstructed from Ref.[2]).

S_i state	Ca (thylakoids)		Sr (BBY)	
	k_s,s^{-1}	k_f,s^{-1}	k_s,s^{-1}	k_f,s^{-1}
S_0	~ 10	> 120	—	—
S_1	~ 0.02	> 120	~ 0.08	> 120
S_2	~ 2.0	~ 120	~ 9.0	> 120
S_3	~ 2.0	~ 40	~ 6.0	~ 23

and 6, attributed to a higher spin configuration, $S \geq 5/2$. Warming of the sample above 65 K, in the dark, leads to the loss of the $g = 10$ and 6 resonances with the corresponding appearance of the $g \approx 4.1$ signal[34]. Moreover, the states responsible for the MLS and $g \approx 4.1$ can be interconverted[27, 68, 69]: at around 150 K, the state responsible for the MLS is converted to that responsible for the $g \approx 4.1$ signal upon the absorption of infrared light. This conversion is fully reversible at 200 K[30].

S_3 state signals. Earlier CW-EPR measurements suggest that the S_3 state has a ground spin state of three ($S_{GS} = 3$), which indicates that all the oxidized species are strongly magnetically coupled and the oxidation in $S_2 \rightarrow S_3$ transition likely occurs at the level of the cluster[40]. Both a ligand-centered[70, 71] and a Mn-centered oxdiation[21, 72] for $S_2 \rightarrow S_3$ transition are supported by different groups.

1.2.3 Mechanism of O–O Bond Formation

Although we have high resolution XRD structures of the S_1 state[10, 58], the crystal structures do not identify the two substrate waters that are involved in O–O bond formation. In addition, the possibility that oxo-bridges may be the substrate waters makes it even harder to reveal the mechanism of water oxidation. Based on the substrate exchange data (Table 1.2), mechanisms involving two oxo-bridges are highly unlikely.

Almost all proposed O–O bond formation mechanisms assume HOP. Here we summarize several that are currently in discussion: a nucleophilic mechanism between a Ca bound water (W3) and a terminal oxo (W2) formed during the S state cycle on Mn4[18, 73, 74]; a nuleophilic mechanism between W3 and O5[75, 76, 43]; a mono Mn

mechanism, in which the coupling occurrs between the two terminal water derived ligands on Mn4[77, 78]; radical coupling of W2 with O5[79]; and radical coupling between O5 and a terminal oxyl-radical from a non-crystallographic water, which first bind to Mn1 as terminal hydroxo ligand during the $S_2 \rightarrow S_3$ transition[80].

Cox *et al.* presented a summary of experimental findings regarding substrate water-binding to the Mn_4CaO_5 cluster in PSII[2]. It appears to disfavor the nucleophilic mechanisms in which Ca bound water attacks a terminal oxo or a μ-oxo bridge, since they regarded the slow substrate water involves O5. As a result, the mechanisms are differentiated by the choice of the fast water W_f, either a hydroxo bound to Mn4[52] or a new introduced non-crystallographic water (bound to Mn1) proposed by Siegbahn[80]. These two mechanisms are very similar to each other and the intermediate structures are analogs to the "closed" and "open" or $g \approx 4.1$ and MLS types. The advantage of Siegbahn's original proposal is a lower energy barrier for O–O bond formation. The $g \approx 4.1$ type has the advantage of easy access to water (W2) and groups (e.g. D1-Asp61) that can accept and shuttle away protons during the S state cycles. As it's pointed out[2], if the barrier for inter-conversion between them in S_3/S_4 is small, one may imagine that the "closed" form facilitates substrate binding during $S_2 \rightarrow S_3$ transition and rearranges to the "open" form which allows a lower energy barrier for O–O bond formation[2].

1.3 Motivation and Organization

The fact that all contemporary oxygenic phototrophs characterized to data use an identical OEC (over several billion years of evolution) makes it remarkable and an interesting research problem. More importantly, the detailed knowledge of PSII will provide fundamental design principles for designing bioinspired water oxidation catalysts and bioengineering reaction centers[14, 81], i.e. artificial systems, and hence provides the blueprints for human energy infrastructures based upon the conversion of solar to stored chemical energy. By mimicking the essential components of biological systems, efficient and stable energy conversion technologies may be developed, utilizing earth-abundant materials and operating under mild conditions.

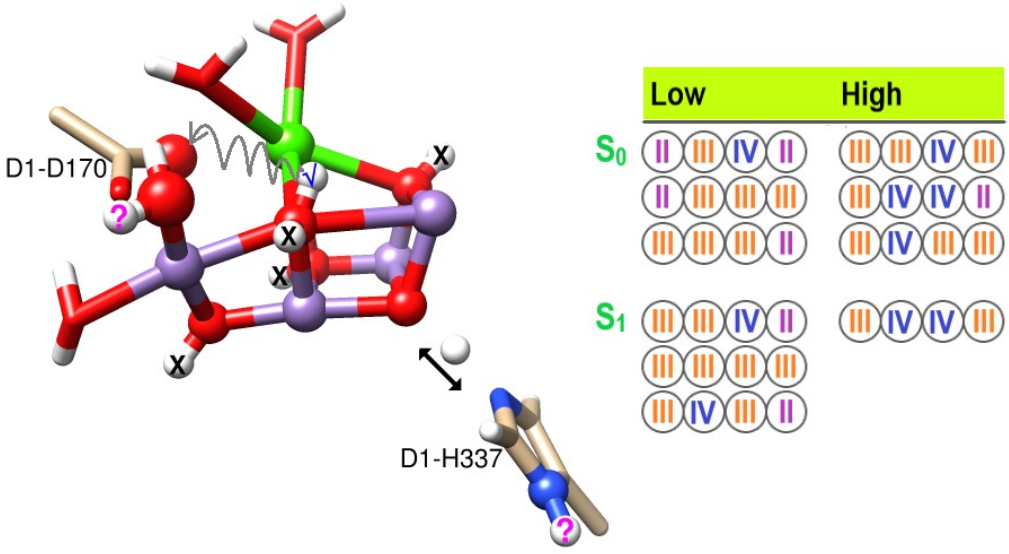

Figure 1.4: Investigation of protonation and oxidation states of the OEC.

This dissertation devotes to understand the fundamentals of the OEC, especially in the protonation and oxidation states and spectroscopy properties.

Chapter 2 intends to resolve the ambiguous protonation and oxidation states of the OEC in PSII. We apply quantum mechanics/molecular mechanics (QM/MM) method on numerous S_0 and S_1 configurations to study the structural features of the OEC. We systematically alter the hydrogen-bonding network and the protonation states of bridging and terminal oxygens and His337 to investigate how they influence Mn-Mn and Mn-O distances, relative energetics, and the internal distribution of Mn oxidation states, in both high and low-oxidation state paradigms (Figure 1.4).

Chapter 3 investigates the geometric and spectroscopic properties of the S_2 state, using quantum chemical density functional theory calculations, focusing on the neglected low paradigm. Various configurations are obtained by modifying the protonation state or position of O5 and protonation state of His337.

Chapter 4 presents results related to higher S state and O–O bond formation. S_3 and S_4 configurations may contain one additional water ligand (O6: H_2O or OH^-). HFCs of S_3 configurations with $S_{GS} = 3$ under the low paradigm are calculated. Various pathways for peroxide formations are examined.

Chapter 5 investigates the peroxide and dioxygen formation mechanism of a cobalt

cubane cluster: $Co_4O_4(OAc)_4(py)_4$. Complete energy profiles are provided. Comparisons have been made with the OEC.

Chapter 6 concludes the dissertation and suggests further directions.

Chapter 2

Resolving Ambiguous Protonation and Oxidation States in the Oxygen Evolving Complex of Photosystem II

2.1 Overview

Photosystem II (PSII) of photosynthetic organisms converts light energy into chemical energy by oxidizing water to dioxygen at the Mn_4CaO_5 oxygen evolving complex (OEC). Extensive structural data have been collected on the resting dark S_1 state from crystal diffraction and EXAFS studies, but the protonation and Mn oxidation states are still uncertain. A "high-oxidation" model assigns the S_1 state to have the formal Mn oxidation level of (III, IV, IV, III), whereas the "low-oxidation" model posits two additional electrons. Generally, additional protons are expected to be associated with the low-oxidation model and were not fully investigated until now.

The number of distinct protonation states of the OEC that could potentially arise (ignoring energetics) for each oxidation state is equal to $n = 2^X$, where X represents the number of ionizable residues in the active site. Considering only the first coordination shell atoms bound to the Mn and Ca ions $X \geq 20$ and $n \geq 2^{20}$. Many configurations can be excluded on energetic grounds or by the structural data.

In light of the large number of possible protonation and oxidation states, it is not surprising that no comprehensive computational analysis has been carried out, nor can we provide that here. Rather, we expand upon the range of possible protonation states previously investigated and apply this to understand the 1.95 Å XFEL and 1.9 Å XRD structures and distances fit to EXAFS measurements. Quantum mechanics (QM) calculations are useful to study the geometry and electronic structure of the OEC, but pure quantum mechanics calculations may lose some important information about the hydrogen-bonding networks around the OEC, which likely plays a crucial

role in proton transfer from the cluster to the bulk water, and which may influence the structure of the OEC core. For this purpose, a combined quantum mechanics/molecular mechanics (QM/MM) approach is favored. This computational approach has been used for the OEC by several groups[82, 83, 84], and has been found to provide a reliable description of hydrogen-bonding networks and protein folding environments. Herein, we use QM/MM models and systematically alter the oxidation states of the OEC and protonation states of oxo bridges, one water ligand (W2) and His337 to investigate the factors that determine the lengths of Mn-Mn vectors. QM-only calculations were also performed on selected intermediates for estimating relative energies.

2.2 Methodology

2.2.1 QM Model

For the pure QM model, the 1.95 Å XFEL crystal structure monomer B (data set 1) was used to construct an original S_1 structure. Preliminary calculations with a model containing only the first sphere residues and four directly bonded waters (labeled W1 to W4) showed large artifacts in terms of the positions of W1, W2 and O5, leading to distortions of the ligand field of Mn4. This implies the additional hydrogen-bonding network influences the geometry of the OEC and points to the need for a larger structural model. Our current model is shown in Figure 2.1, and arguments supporting our choice of protonation steps are provided below. Four Mn ions, one Ca ion, and five oxo bridges form the inorganic core. The structure contains all seven first sphere residues, D1-Asp170, D1-Ala344, D1-Glu189, D1-Asp342, D1-His332, D1-Glu333, and CP43-Glu354, which are directly bound to the Mn_4CaO_5 core. Second sphere residues include D1-His337 (hydrogen bonded with O3) and CP43-Arg357 (weak H-bond interaction with O4 and O2). The structure also contains D1-Asp61, its surrounding structured water molecules, and D1-Tyr161-His190 pair is also included. We assume that all carboxylates are deprotonated, the basic quanidinium of Arg357 is protonated, His332 and His190 have histidines protonated at N_δ, and Tyr161 is protonated (charge neutral). His337 was assumed to be positively charged (HIP in Amber convention) with

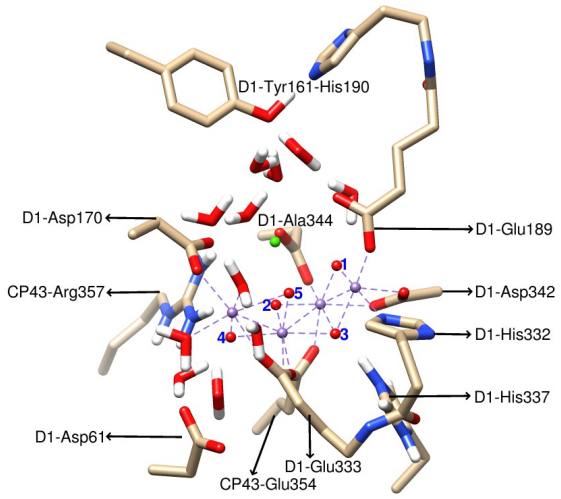

Figure 2.1: OEC S_1 model. Ca green, Mn purple, C tan, O red, N blue, H white; O1-O5 are labeled in blue. Eleven crystallographic water molecules are included and most hydrogen atoms are omitted for clarity.

protons on both N_ϵ and N_δ. Neutral His337, protonated only at N_ϵ, is also investigated in some cases. The alpha carbons of the residues were replaced by methyl groups when possible. Eleven closely associated crystallographic water molecules are also included, four of which are ligands of the cluster and the rest form the hydrogen-bonding network around the inorganic core. Assuming the S_1 high oxidation state with all bridging oxygens in the form of oxide and all terminal water in the form of H_2O, the total number of atoms and net charge will be 213 and +1, respectively.

2.2.2 QM/MM Model

Because the water network plays an important role in both the structure and function of PSII, we maintained the water network and its surrounding protein environment in the QM/MM models using monomer B (data set 1) of the 1.95 XFEL structure. The surrounding waters and amino acids can form strong hydrogen bonds with the waters in the QM region (e.g. D1-Ser169 H-bonds with W1, D1-Gln165 H-bonds with W4, etc.), which are important for the structural stability of the OEC.

The QM/MM model (Figure 2.2A) was constructed applying Batistas approach[82]. In detail, it contains residues with both C-alpha atoms and crystallographic water

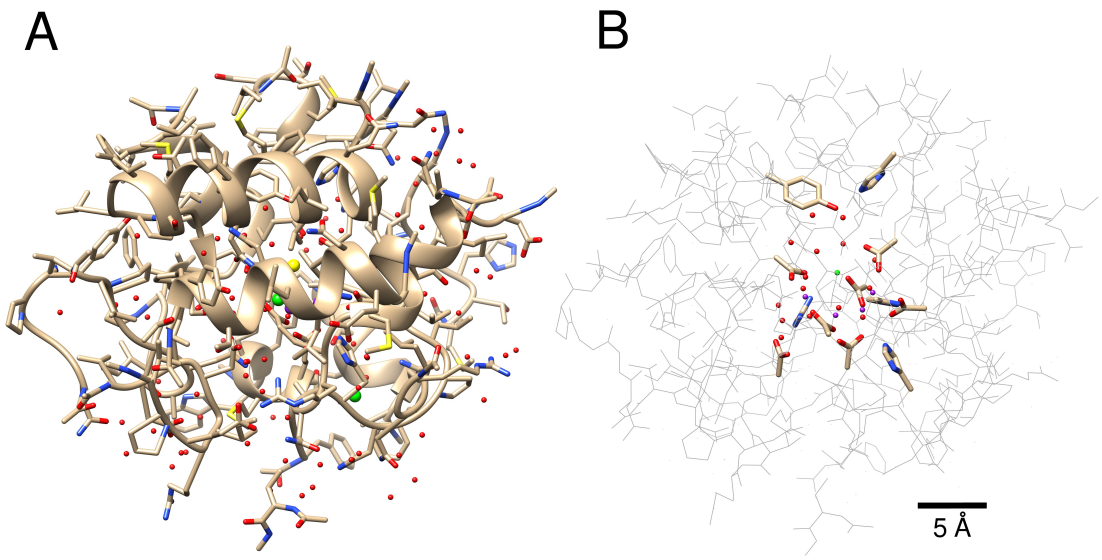

Figure 2.2: Heavy atoms included in the QM/MM model (A) and the QM region (B).

molecules (O atoms) within 15 Å of the closest atoms in the Mn_4CaO_5 cluster plus two chloride ions near the OEC. Where the selection causes a gap of up to two residues in a peptide chain, the missing residues were added to provide continuity. Capping groups (NME or ACE) were added for each chain break, with positions determined by backbone atoms of neighboring residues.

The QM region in this model is a truncated version of the pure QM model described in Section 2.2.1. It has the same metal cluster, crystallographic water molecules and amino acids around, except that the amino acids were cut across carbon-carbon covalent bonds to minimize the QM region size. Depending on the chosen protonation state, the final QM region has about 160 atoms (Figure 2.2B). For the modeled S_1 high oxidation state with all bridging oxygens in the form of oxo and all terminal water in the form of H_2O, the total number of atoms and net charge for the QM region are 161 and +1, while they are 13027 and -4 for the full QM/MM model.

Sets of possible QM/MM models were geometry optimized for S_0 and S_1; the different protonation states of the oxo bridges, water ligand W2 and His337 are summarized in Table 2.1. Since dark-adapted preparations may contain a mixture of oxidation states[46, 56], we investigated both S_0 and S_1. In the high oxidation state paradigm,

Table 2.1: Different investigated protonation states of the OEC. HIE and HIP are AMBER naming convention for histidine, where HIE is histidine with $N_\epsilon H$. HIP is histidine with both $N_\delta H$ and $N_\epsilon H$, and therefore is positively charged.

	Protonation States
W2	OH^-, H_2O
O1, O2, O4	O^{2-}, OH^-
O5	O^{2-}, OH^-, H_2O
His337	HIE, HIP
O3	O^{2-}

we have an average oxidation state of 3.25 for S_0 and 3.5 for S_1, while the low oxidation state paradigm these are 2.75 for S_0 and 3.0 for S_1. Because the geometry optimization of the OEC is virtually independent of the precise nature of the spin alignment[74], which we independently confirmed, we performed the calculations assuming the high spin configurations for each state, although the true ground state of the OEC may be either low-spin or intermediate-spin configurations arising from anti-ferromagnetic intermanganese couplings. The optimized geometries were then compared to the crystal structures. In all cases the spin states of individual Mn ions were fixed to be high spin, consistent with prior EPR data and as expected for Mn ions with this ligand set.

2.2.3 Computational Details

QM calculations

QM calculations were performed with ORCA[85]. Geometry optimizations were carried out with BP86 functional[86, 28], which often yields more realistic structural parameters than hybrid functionals[87]. Polarized valence triple-zeta basis sets (def2-TZVP)[88] were used for all elements except for carbon and hydrogen. For carbon and hydrogen, polarized valence double-zeta basis sets (def2-SVP)[88] were used. The calculations take advantage of the resolution of identity (RI) approximation with the auxiliary def2-TZVP/J Coulomb fitting basis sets[89] as implemented in ORCA. Tight convergence, increased integration grids (Grid4 in ORCA convention) and an unrestricted Kohn-Sham method were used. The influence of the environment was simulated using the

conductor-like screening model (COSMO)[90] assuming a permittivity of 8.0. The alpha carbons were kept fixed at the positions from the 1.95 Å XFEL structure as the backbone constraints so as to maintain the overall protein environment.

Since the hydrogens were not revealed in the crystal structure and were initially added using AMBER, we firstly performed 20 cycles geometry optimization only on hydrogens with valence double-zeta basis set (SV)[91, 92] so as to remove the possible unrealistic positions of hydrogen atoms. Then geometry optimization was performed on the whole structure with settings described above. The geometry optimization assumes high-spin configuration, where all spins are aligned in parallel.

QM/MM calculations

QM/MM calculations were carried out using an extensible interface between the AMBER molecular dynamics (MD) software package and ORCA electronic structure software package[93]. In all QM/MM calculations, the removal of translational, rotational center-of-mass (COM) motion and fast SHAKE routines for waters were turned off. Constant volume periodic boundaries were used. The non-bonded cutoff was specified as 8.0 Å. The structure is solvated with an 8.0 Å buffer of a truncated octahedral box of explicit TIP3P[94] water molecules. Additional Na^+ or Cl^- were added to neutralize the structures. The ff14SB force field[95] was used for the protein. Electronic embedding was applied, which allows for polarization of the embedded QM region due to the presence of the electrical field of the surrounding MM environment by calculating the Coulomb interaction between the charge density of the QM region and the MM point charges. It treats the van der Waals (vdW) interaction between the atoms at the interface of QM and MM regions in terms of an empirical Lennard-Jones (LJ) 6-12 potential[96]. The LJ parameters for the manganese ion are adopted from Zn^{2+}, which are 1.10 Å and 0.0125 kcal·mol^{-1} for vdW radius Rmin/2 and the depth of the potential well ϵ, respectively. The bonded terms, introduced by the QM/MM boundary crossing covalent bonds, are handled using explicit link atoms as implemented in AMBER.

A two-stage minimization (see below) was first conducted. In order to obtain a reasonable optimized QM region, we then performed the calculations for several iterations,

where an iteration entails 1 psec molecular dynamics (MD) simulation on the MM region, followed by 100 cycles QM/MM minimization on the QM region. The details are described below. After alternating the MD simulation and QM/MM minimization for three times, we believe the MM region was already in a reasonably good equilibrium state. Then we did a final QM/MM minimization on the QM region until the root-mean-square of the components of the gradients is smaller than 0.05 kcal·mol^{-1}·Å^{-1}. The final structures of the QM region were used for geometric analysis.

Two-stage minimization: At the beginning, minimization was performed on the MM region, while the QM region was fixed using "ibelly" flag in AMBER. Atomic positions were restrained (with weight 10 kcal·mol^{-1}·Å^{-2}) for the two chloride ions, alpha carbons which are 12 Å away, terminal carbons (CH_3 in NME or ACE) and oxygen of water molecules within 12 Å. 2000 cycles of minimization using the steepest descent method were carried out followed by 3000 cycles using conjugate gradient method. The initial step length is 0.01 and the convergence criterion for the energy gradient is set to be $1.0E-4$ kcal·mol^{-1}·Å^{-1}.

After the initial minimization of the MM region, another QM/MM minimization on the hydrogen atoms was performed by 100 cycles so as to remove improper directions of the hydrogen atoms in the QM region assigned initially. The XMIN method in Amber with Truncated Newton linear Conjugate Gradient (TNCG) was used. We specified the size of the electrostatic cutoff to be 8.0 Å for QM/MM electrostatic interactions, within which the MM point charges were included as external electric field in the QM Hamiltonian.

Iteration: After the two-stage minimization, molecular dynamics (MD) simulation was performed on the MM region while the QM region was fixed. For the Mn_4CaO_5 cluster, partial charges were assigned as follows: Ca = +1.0, O1-O5 = -0.5, and remaining charges are evenly distributed on the four manganese ions. Again, we have two chloride ions, alpha carbons which are 12 Å away, terminal cartons (CH_3 in NME or ACE) and oxygen of water molecules within 12 Å be constrained in Cartesian space using a harmonic potential with weight 10 kcal·mol^{-1}·Å^{-2}. The MD simulation was performed for 0.1 nsec with time step 0.0005 psec. Berendsen temperature control[97] was

used with initial temperature 0 K and final temperature 300 K. Time constant for heat bath coupling for the system was set to be 1 psec. Subsequent QM/MM minimization was performed on the QM region while the MM region was frozen.

The 1 psec MD (with QM region fixed) together with the 100 cycles QM/MM minimization (with MM region fixed) is called one iteration.

2.3 Results and Discussion

We first compared our geometry-optimized structures of the OEC with XRD, XFEL and EXAFS data. We sought to determine the extent to which the protonation and oxidation states of the OEC influence the Mn-Mn distances, position of residues, and root-mean-square-deviation from the crystal structure.

In general, computational models using the high paradigm easily generate short Mn-Mn distances that closely approximate the EXAFS data (Table 2.2), provided they assign O5 as O^{2-} in the S_1 state[61, 98, 99, 100]. However, the optimized Mn3-O5 distance is very short (around 1.8 Å), which is incompatible with both the XFEL and 1.9 Å XRD structures (2.20 Å and 2.39 Å, respectively, Table 2.2). Therefore, to resolve this inconsistency the XRD and XFEL data are often assumed to be in a more reduced state, attributed to radiation damage or a mixture of lower S states (S_0 and S_1). The existence of the mixture of S states may be caused by the extensive (1 week) dark adaption used in an attempt to depopulate higher S states that are unusually stable in PSII crystals, which can lead to a significant fraction of the PSII cores poised in the S_0 state, rather than only S_1. Under the low oxidation state paradigm, models typically have more protons, since O5 could be protonated as OH^- or H_2O[61, 62], which generates the observed longer Mn-O5 distance. However, the low paradigm models have been criticized for producing too long Mn-Mn distances[1]. We found these previous studies[56, 1, 63] were incomplete and hence reexamine this question here. We start with a discussion of the least controversial topic, the protonation states of the three core oxygen atoms, O1 to O3, and O4, which bridges the Mn_3Ca cube and dangling Mn4.

Table 2.2: Key Mn-Mn and Mn-O5 distances [Å] from the diffraction studies: 1.9 Å XRD and 1.95 Å XFEL structures in the dark resting S state, i.e. the "S_1 state". EXAFS derived Mn-Mn distances are listed for comparison.

Parameter	EXAFS (Dau[24])	EXAFS (Yano[23])	1.9 Å XRD	1.95 Å XFEL
Mn1-Mn2	2.69, 2.74	$2\times \sim 2.7$	2.84	2.70
Mn2-Mn3		$1\times \sim 2.8$	2.89	2.71
Mn3-Mn4			2.97	2.87
Mn1-Mn3			3.29	3.25
Mn1-O5			2.60	2.70
Mn3-O5			2.39	2.20
Mn4-O5			2.49	2.33

2.3.1 Protonation States of O1, O2, O3, and O4 in the S_1 State

The 1.95 Å XFEL structure shows an extensive hydrogen bonding network around the bridging oxygens of the OEC cluster. Specifically, O1 and O4 have very short hydrogen bonds with nearby water molecules, which indicates strong local interactions. O3 has a short hydrogen bond with His337. CP43-Arg357, as shown in Figure 2.1, has a positively charged guanidinium side chain that is within $3.0 \sim 3.3$ Å of O2 and O4, which implies weak hydrogen bond interactions with the cluster. The QM region in our QM/MM model is large enough to contain all these hydrogen-bonding interactions and the MM region maintains the protein environment. The nomenclature here refers to the S_i state (number of electrons removed), the Mn oxidation state (low or high paradigm), and the protonation states of O1 or O4. For example, S_0L_O1H (Table 2.3) refers to a configuration in the S_0 state with protonated O1 under the low paradigm.

Protonation state of O1. The distance between O1 and a nearby water molecule (W8) is 2.43 Å in monomer B (data set 1) of the 1.95 Å XFEL structure (Figure 2.3A). Such a short distance implies a strong hydrogen bond interaction between O1 and W8. To investigate the protonation state of O1, we assume that O2, O3, O4 are oxo species, W2 is H_2O and His337 is in the form of HIP (with both $N_\delta H$ and $N_\epsilon H$). O5 is treated as OH, suggested by Suga *et al.* for the 1.95 Å XFEL structure[58]. Since an exhaustive study, which would involve all possible protonation patterns, is computationally too expensive, we only considered a subset with reasonable assumptions. We performed QM/MM calculations on four configurations in S_1 state, with either protonated or

Table 2.3: The bond distances to O1 and O4 [Å] obtained from the XFEL structure and the root-mean-squared-deviations (RMSDs) of the ten atoms of the $CaMn_4O_5$ cluster for eight configurations in S_1. The distances in the XFEL structure are averaged over the two monomers in data set 1.

	XFEL	S_1H_O1	S_1H_O1H	S_1L_O1	S_1L_O1H
O1-W8	2.48	2.74	2.44	3.02	2.60
O1-Mn1	1.82	1.83	1.90	1.85	2.14
O1-Mn2	1.78	1.80	1.96	1.92	2.17
Mn1-Mn2	2.64	2.74	2.85	2.88	3.03
RMSD	0	0.179	0.201	0.204	0.249
	XFEL	S_1H_O4	S_1H_O4H	S_1L_O4	S_1L_O4H
O4-W9	2.59	2.83	2.62	2.67	2.64
O4-Mn3	1.91	1.82	1.95	1.92	1.90
O4-Mn4	1.99	1.83	1.93	1.78	2.11
Mn3-Mn4	2.84	3.02	3.11	3.00	3.14
RMSD	0	0.179	0.175	0.204	0.168

unprotonated O1 and either high paradigm or low paradigm. The bond distances relative to O1 obtained from the XFEL structure and the root-mean-squared-deviations (RMSDs) of the $CaMn_4O_5$ cluster for the four configurations in S_1 are shown in Table 2.3 (top). Configurations with protonated O1 under either the high or low paradigm (S_1H_O1H and S_1L_O1H), in which W8 is modeled as a neutral H-bond acceptor, are able to reproduce the very short O1-W8 distance (2.44-2.63 Å). However, the RMSDs become much larger and the bond distances between the more accurately positioned heavier atoms Mn1-Mn2, O1-Mn1 and O1-Mn2 increase significantly, well above their experimental values (by 0.2 to 0.4 Å longer for Mn1-Mn2). Hence, the latter metrics support the conclusion that O1 is not protonated, and the position of W8 in the XFEL structural model may not be well constrained by the XRD data.

Protonation State of O2 and O3. Our calculations with protonated O2 (OH^-) generated Mn2-Mn3 distances of 2.95 and 3.01 Å for the high and low paradigms, respectively, which are much longer than 2.67 Å in the XFEL structure. Therefore, O2 can be assigned as an oxo species with confidence. O3 is H-bonded to His337 in the XRD structures, based on the short distance of 2.65 Å between O3 and N_ϵ^{His337}. Computationally, O3's protonation state is strongly coupled to the protonation state of His337. With positive His337, there could be proton sharing between O3 and N_ϵ^{His337}, whereas

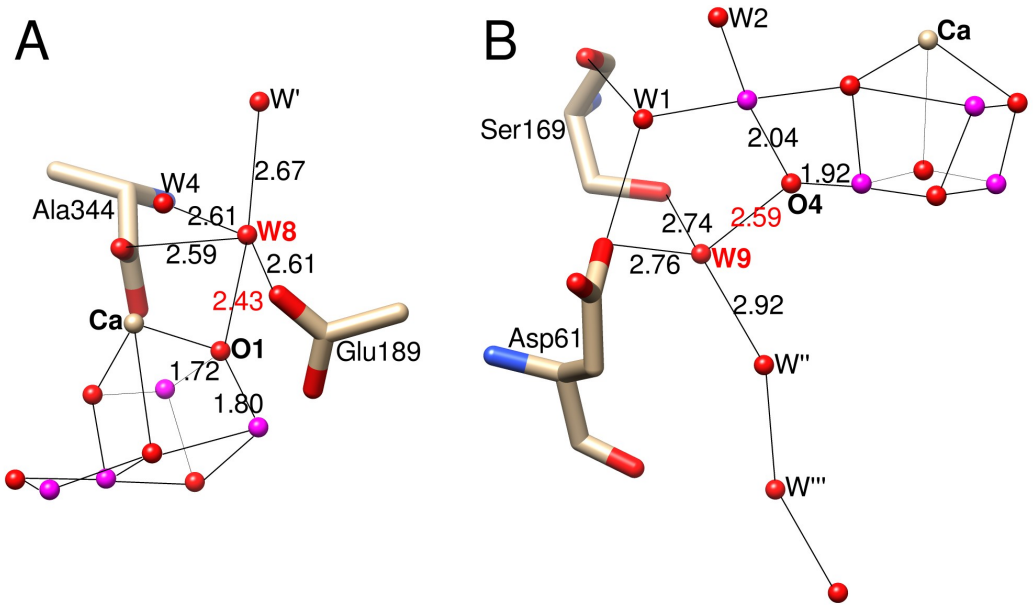

Figure 2.3: Water network around O1 (A) and O4 (B) in the 1.95 Å XFEL structure (monomer B data set 1).

O3 stays unprotonated with neutral His337. Our calculations show that configurations with positive His337 generate short distance between O3 and N_ϵ^{His337} (ca 2.6 Å, in agreement with the crystal structure), while this distance is longer for configurations with neutral His337 (ca 2.8 Å), regardless of the choice of low vs high oxidation states. Hence, we used a positive His337 with double protonation states ($N_\delta H$, $N_\epsilon H$, denoted HIP) unless mentioned otherwise. Implications of neutral His337 will be discussed in Section 2.3.3.

Protonation State of O4. The situation for O4 is analogous to that for O1. We again performed QM/MM calculations for four configurations in S_1 state, with either protonated or unprotonated O4 and either high or low paradigm. The resulting RMSDs and bond distances are shown in Table 2.3 (bottom). The low paradigm models consistently predict the short W9-O4 distance, regardless of O4 protonation state, and consistent with a strong H-bond (Figure 2.3B), whereas high paradigm models can only reproduce short W9-O4 distance with protonated O4. However, models with protonated O4 generate much longer Mn3-Mn4 distances (by 0.2-0.3 A), and as these are the most accurately measured distances, we conclude that O4 is an oxide species (not protonated). Note that model S_1L_O4H has lower RMSD compared to model S_1L_O4. Looking at

Table 2.4: Different Protonation States of S_1 State of OEC Suggested by Different Groups. HIP, HID, and HIE are AMBER naming convention for histidine, where HID is histidine with $N_\delta H$, HIE is histidine with $N_\epsilon H$, and HIP contains both protons.

	Pace[61, 62]	Neese[46]	Batista[82]	Yamaguchi[63]
W2	OH^-, H_2O	OH^-	H_2O	OH^-
O5	H_2O, OH^-	O^{2-}	O^{2-}	OH^-
His337	HID, HIP	HIP	HIP	HIE

Table 2.5: RMSDs (Å) of the ten atoms of the $CaMn_4O_5$ cluster for different configurations compared with the 1.95 Å XFEL structure.

	1H	2Ha	2Hb	3Ha	3Hb	4H
S_0L	0.177	0.138	0.188	0.315	0.167	0.293
S_0H	0.153	0.183	0.202	0.210	0.171	0.242
S_1L	0.173	0.145	0.155	0.187	0.204	0.253
S_1H	0.160	0.154	0.201	0.353	0.179	0.227

the individual oxidation states, we found III-III-III-III for S_1L_O4 and III-IV-III-II for S_1L_O4H. As we show below, for the low paradigm models, the latter pattern of oxidation states match the 1.95 Å XFEL structure better.

2.3.2 Protonation State of O5 in the S_1 State

Although there have been several previous studies focusing on the protonation states of the OEC[56, 1, 63], making comparisons to high resolution XRD[10] and XFEL[58] structures, there is little consensus about the protonation state of O5 in the S_1 state (Table 2.4). We systematically changed the protonation state of O5 in the S_0 and S_1 states under either the low or high paradigms and calculate the optimized structures. Since it is possible to form a hydrogen bond between W2 and O5, the protonation state of W2 is also altered accordingly. Specifically, we investigated protonation states of O5 as O^{2-}, OH^-, or H_2O, and those of W2 as OH^- or H_2O, resulting in six models per oxidation state. The QM/MM geometry optimized structures and comparable energies predicted from QM calculations are shown in Figures 2.4-2.7. The corresponding RMSDs are summarized in Table 2.5.

The nomenclature refers to the S_i state, the Mn oxidation state, and the total number of protons distributed on O5 and W2 (different from Section 2.3.1). For example, in Figure 2.4, the upper left model, S_0L_1H, is a "one-proton model" in the S_0 state

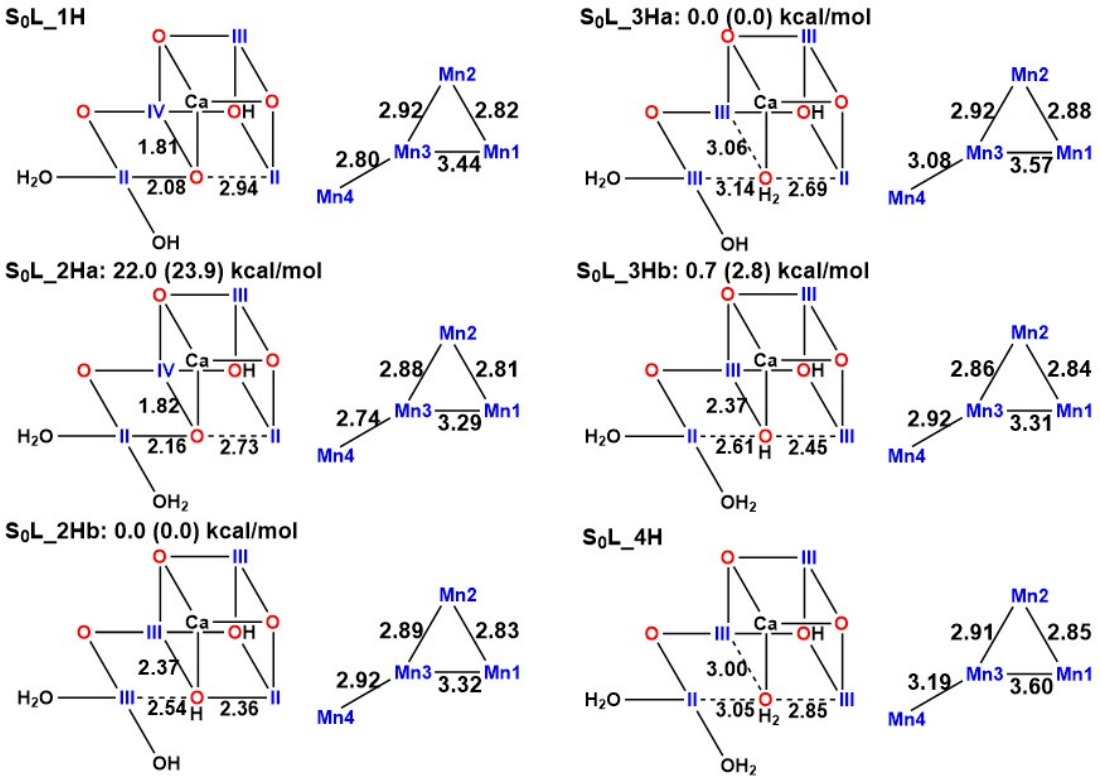

Figure 2.4: Protonation states, Mn oxidation patterns, and Mn-Mn distances [Å] for six energy-minimized S_0L QM/MM models with His337 as HIP. The energy diagrams among isomers are obtained from QM calculations on QM-only models with His337 in the form of HIP (the values in the parentheses are obtained using His337 as HIE).

under low paradigm. For models with 2 protons distributed on O5 and W2, there are two alternatives, named S_0L_2Ha and S_0L_2Hb. S_0L_2Ha has two protons on W2 (H_2O), while S_0L_2Hb has one proton on W2 (OH^-) and the other proton on O5 (OH^-). There are also two alternatives for "three-proton models", in which W2 = OH^-, O5 = H_2O (S_0L_3Ha) and W2 = H_2O, O5 = OH^- (S_0L_3Hb). The S_0L "four-proton model" (S_0L_4H) has both W2 and O5 in the form of H_2O initially. The nomenclature for higher oxidation states is the same and the optimized models are shown in Figures 2.5, 2.6, and 2.7 respectively. Note that O3 is protonated in some models, for example S_0H_1H in Figure 2.6. This is a consequence of a proton transfer from protonated His337 to O3, which happens when the net positive charge on the cluster is lower. Since this proton comes from His337 and the initial state of His337 is the same among all models at this stage, we don't include this extra proton in our naming convention.

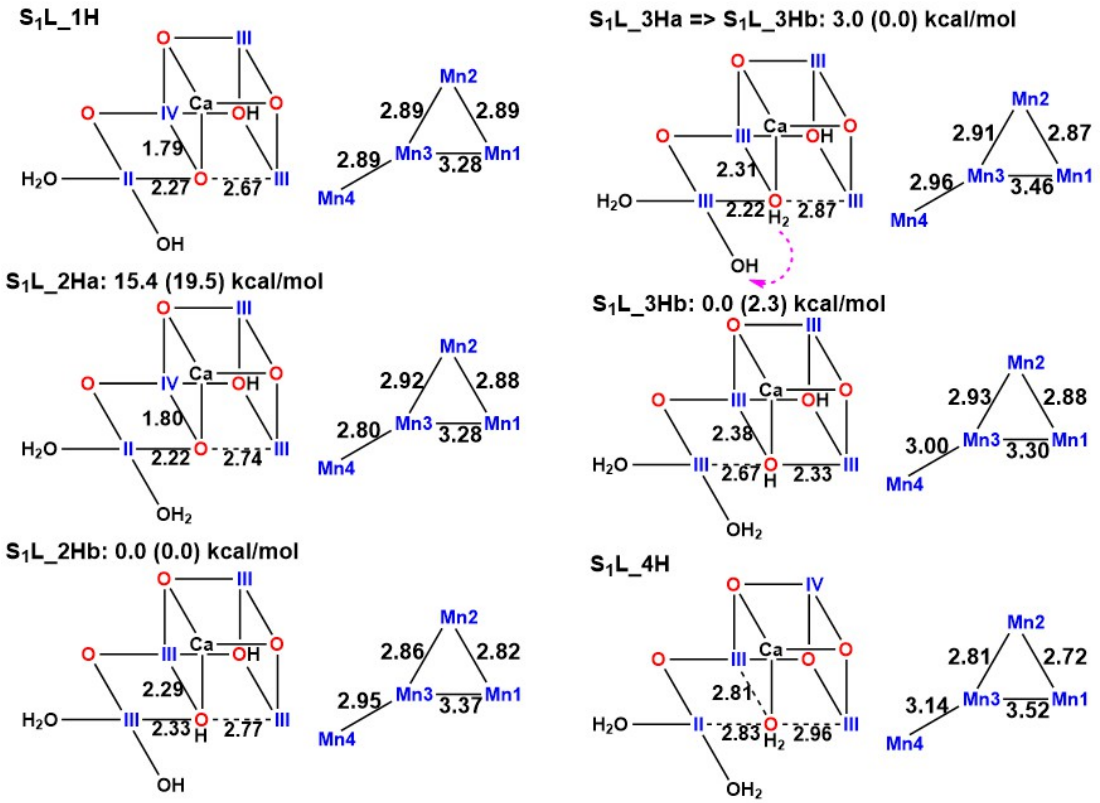

Figure 2.5: Protonation states, Mn oxidation patterns, and MnMn distances [Å] for S_1L models.

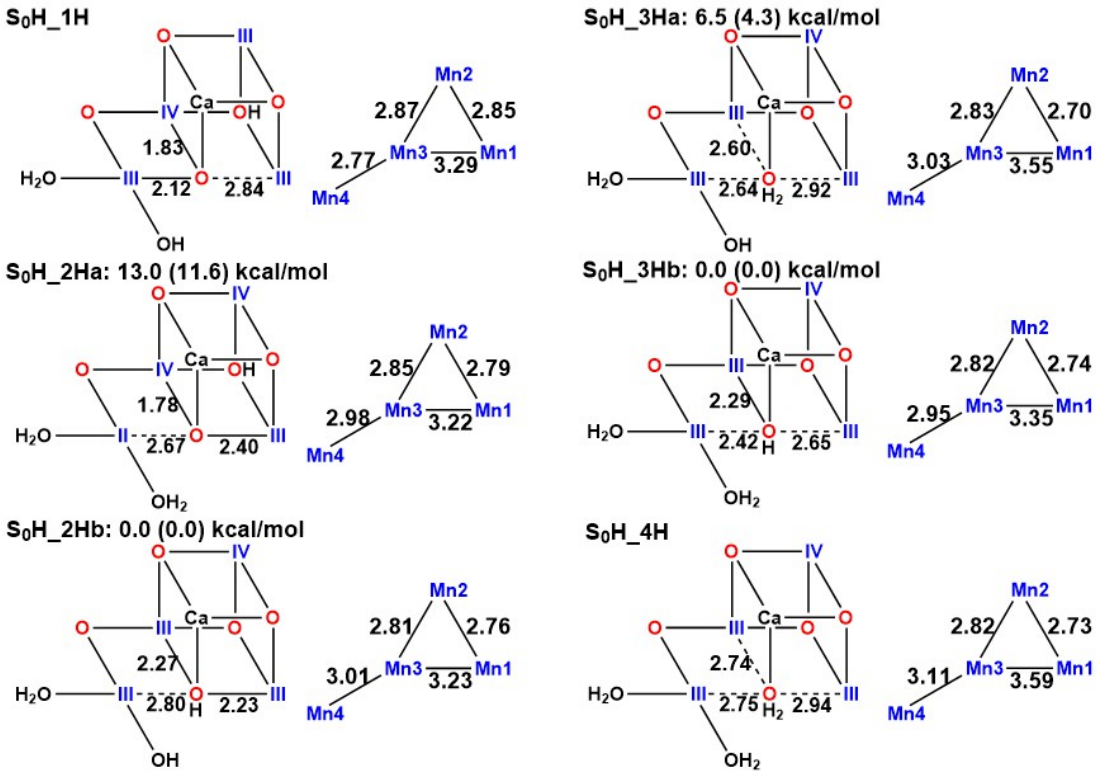

Figure 2.6: Protonation states, Mn oxidation patterns, and MnMn distances [Å] for S_0H models.

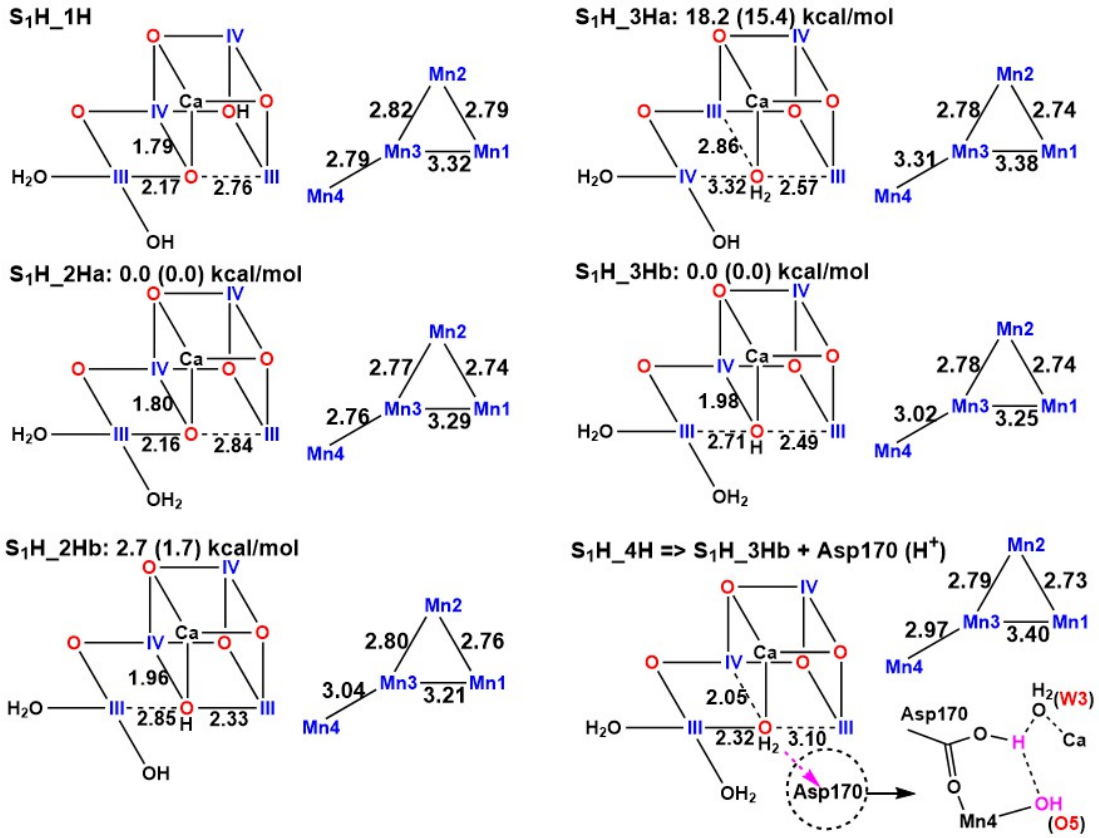

Figure 2.7: Protonation states, Mn oxidation patterns, and MnMn distances [Å] for S_1H models.

Treating O5 as H_2O

S_0L_3Ha and S_0L_4H in Figure 2.4 both have O5 in the form of H_2O. Most obvious are the resulting significantly long Mn-O5 distances compared with the crystal structures. The average distances for Mn1-O5, Mn3-O5 and Mn4-O5 of S_0L_3Ha and S_0L_4H are 2.82 Å, 3.0 Å and 2.88 Å, respectively, which are significantly larger than the 1.95 Å XFEL and 1.9 Å XRD structural data (Table 2.2). The same pattern appears in other models having O5 in the form of H_2O in different oxidation states ("3Ha" and "4H" models in Figures 2.5, 2.6, 2.7). The corresponding RMSDs are also much larger (Table 2.5). Note that the RMSD for S_1L_3Ha is relatively small (0.187 Å). This is because S_1L_3Ha went through a proton relocation from O5 (H_2O) to W2 (OH^-) during geometry optimization, resulting in a configuration having the same protonation state as S_1L_3Hb (Figure 2.5), i.e. O5 (OH^-) and W2 (H_2O). These two optimized configurations correspond to the "open" and "closed" cubane isomers, which differ in the position of O5. Upon optimization, S_1L_3Ha turns into a configuration having relatively shorter Mn4-O5 and longer Mn1-O5 distances, corresponding to an "open" cubane structure, and Mn1 remains pentacoordinate. Similarly, the optimized S_1L_3Hb has relatively longer Mn4-O5 and shorter Mn1-O5 distances, corresponding to a "closed" cubane structure.

Even when W2 (H_2O) is not available as proton acceptor in configuration S_1H_4H, a proton from O5 (H_2O) automatically moves to the carboxylate of D1-Asp170, an adjacent bidentate ligand bridging between Mn4 and Ca in the XRD structures (Figure 2.7). The resulting configuration is similar to S_1H_3Hb, but with a proton bound to monodentate D1-Asp170. The D1-Asp170 remains ligated to Mn4 and the carboxylate OH group H-bonds to both W3 and O5 (Figure 2.7). Similar to the S_1L_3Ha→S_1L_3Hb transition above, the optimized S_1H_4H and S_1H_3Hb structures also show different configurations in terms of "open" and "closed" structures, with S_1H_4H being "open" and S_1H_3Hb being "closed". It's clear that all models with O5 in the form of H_2O either produce unacceptably long Mn-O5 distances (large RMSDs), or automatically transfer a proton from O5 to a nearby base to stabilize the structure. This happens

regardless of the oxidation state paradigm. The inconsistency between the calculated and experimental structures of both the 1.95 Å XFEL and 1.9 Å XRD structures is large enough to conclude that O5 is not in the form of H_2O in the S_1 state.

Treating O5 as OH^- or O^{2-}

Configurations with O5 in the form of OH^- generally produce reasonable RMSDs, unlike O5 (H_2O) (Table 2.5). They reproduce the unusual position of O5, regardless of the choice of low vs high oxidation states. For example, the optimized S_1L_2Hb and S_1L_3Hb (Figure 2.5), which initially differ by the protonation state of the terminal water W2, show the averaged distances of Mn1-O5, Mn3-O5 and Mn4-O5 as 2.55 Å, 2.34 Å and 2.50 Å, respectively. Similarly, the corresponding configurations under the high oxidation state, S_1H_2Hb and S_1H_3Hb (Figure 2.7), produced the averaged Mn-O5 distances as 2.41 Å, 1.97 Å and 2.78 Å for Mn1-O5, Mn3-O5 and Mn4-O5 (note that, the produced Mn3-O5 is much shorter than that in the XFEL structure).

Configurations with O5 in the form of O^{2-}, which also produce small RMSDs (Table 2.5), always generate relatively short Mn3-O5 distance (Figures 2.4-2.7). The average Mn3-O5 distance over all configurations with O5 (O^{2-}), where Mn3 fits only the IV oxidation state, is 1.80 Å, which is much shorter than that in the XFEL structure (2.20 Å in Table 2.2). The same scenario applies to configurations with O5 (OH^-) under the high paradigm, which have Mn3(IV) and Mn3-O5 distance shorter than 2.0 Å (S_1H_2Hb and S_1H_3Hb in Figure 2.7). On the contrast, configurations with O5 (OH^-) under the low paradigm reproduce the Mn3-O5 much better. This is because Mn3 fits only the III oxidation state (S_1L_2Hb and S_1L_3Hb in Figure 2.5), and the asymmetric electronic distribution of the valence $3d^4$ orbitals, called the Jahn-Teller effect, orients the empty d orbital towards O5. Although the Mn1-O5 and Mn4-O5 distances in S_1L_2Hb and S_1L_3Hb (2.55 Å and 2.50 Å on average) do not seem to match the XFEL data (2.70 Å and 2.33 Å, respectively), this is less of an issue because we consistently see "open" and "closed" configurations of the OEC (e.g. S_1L_2Hb and S_1L_3Hb), which correspond to either long Mn1-O5 or long Mn4-O5. Therefore, we conclude configurations with O5 (OH^-) under the low paradigm are our best candidates for the XFEL structure with

respect to the position of O5. Interestingly, pure QM calculations on both S_1L_2Hb and S_1L_3Hb only converged to open configurations (as seen in crystal structures), which also supports our conclusion towards the protonation state of O5. However, S_1L_2Hb and S_1L_3Hb do not agree with the XFEL structure in terms of Mn-Mn distances or reproduce at least two short Mn-Mn, which is a requirement from the EXAFS. This is the topic we will explore in Section 2.3.3.

As a final remark for the protonation state of O5, it seems that the Mn_3Ca cube tends to have more protons on O5 under lower oxidation states. This is somewhat expected since the repulsion between the proton and cube increases as the oxidation level goes up, and confirmed from the relative energies of various isomers. For example, the energy separation between 2Ha (W2: H_2O, O5: O^{2-}) and 2Hb (W2: OH^-, O5: OH^-) isomers with His337 (HIP) $\Delta H_{2Ha-2Hb}$ decreases from 22.0 to -2.7 kcal/mol (Figure 2.4-2.7). This supports the choice of protonated O5 under the low paradigm[61, 62] and also rationalizes the choice of O5 (O^{2-}) in S_1 state under the high paradigm[98, 99, 100].

2.3.3 Low Paradigm Configurations with Short Mn-Mn Distances

We observe that our optimized S_1 structures under the low paradigm actually agree with the 1.9 Å XRD structure better in terms of the Mn-Mn distances, except for S_1L_4H (Figure 2.5) with oxidation state pattern (III, IV, III, II). Note that, the epsilon proton of His337 of S_1L_4H is not transferred to the O3 bridge, which could be a consequence of the electrostatic repulsion caused by excessive positive charge of the cubane cluster introduced by additional proton on O5. In all other S_1L models the bridge O3 is protonated and these models show long Mn1-Mn2 and Mn2-Mn3 distances that are inconsistent with the Mn-Mn distances of the XFEL structure and the EXAFS constraints. We find that the protonation state of O3 influences the Mn oxidation state distribution and first propose a simple scheme under the low paradigm in Figure 2.8A that accounts for the corresponding structural changes seen in the 1.90 Å XRD and 1.95 Å XFEL structures. The Mn-Mn distances in Figure 2.8A are obtained from QM calculations, performed upon QM model (Figure 2.1), assuming positive His337 (HIP) and W2 (H_2O).

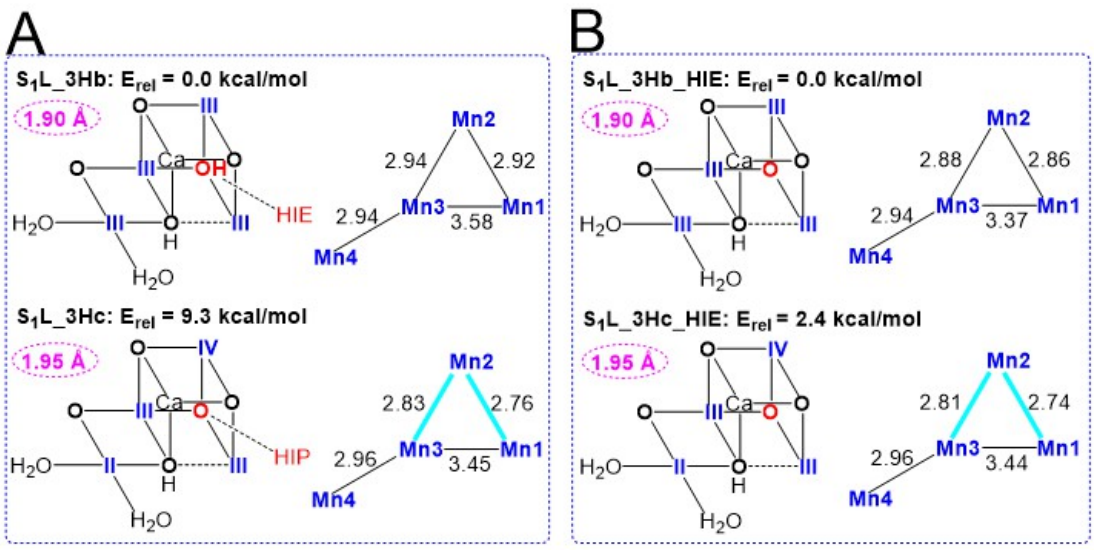

Figure 2.8: Structural and oxidation state distribution changes between 1.9 Å XRD and 1.95 Å XFEL structures under the low oxidation state paradigm can be accounted for by oxidation state redistribution. A) Configurations with His337 (HIP) imply a proton relocation between O3 and His337; B) Configurations with His337 (HIE) have smaller energy separation. The optimized geometries and energies were obtained using QM calculations. The light blue bonds are the short Mn-Mn distances.

Similar to Petrie *et al.*[62], in this scheme, the modeled 1.9 Å XRD structure (S_1L_3Hb in Figure 2.8) has oxidation state pattern (III, III, III, III) while the modeled 1.95 Å XFEL structure (S_1L_3Hc in Figure 2.8) has (III, IV, III, II). In contrast to Petrie *et al.*, the proton relocation in our scheme occurs between O3 and His337 instead of between O5 and W2. The relative energies of these two configurations were examined and the latter configuration has 9.3 kcal/mol higher energy.

To examine the influence of the protonation states of His337 on the geometries, oxidation state distributions and relative energies, we built S_1L QM models with neutral His337 (HIE). Because His337 is now neutral, it is energetically unfavorable to transfer its epsilon proton to O3 bridge. Selected optimized configurations are shown in Figure 2.8B. S_1L_3Hb_HIE and S_1L_3Hc_HIE are analogous to the configurations in Figure 2.8A, i.e. conversion between isomers III-III-III-III and III-IV-III-II, where the latter shows two short Mn-Mn distances. The energy separation is reduced to 2.4 kcal/mol, still with III-III-III-III (S_1L_3Hb_HIE) favored. With W2 (OH^-), similar geometries can be obtained but energy gaps increase to 15.8 and 9.7 kcal/mol with His337 in the

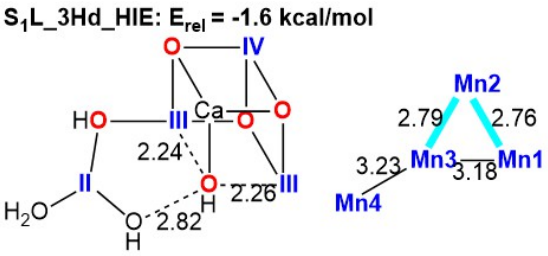

Figure 2.9: An energetically accessible S_1 model under low paradigm with protonated O4 (OH^-) and neutral His337 (HIE); obtained from QM-only calculation. The reference energy is S_1L_3Hb_HIE.

form of HIP and HIE, respectively.

As noted in section 2.3.1, the protonation states of the bridging oxygens also play an important role in determining the Mn-Mn distances. One example is S_1L_4H (Figure 2.5), where O5 is doubly protonated and the configuration converges to III-IV-III-II oxidation state with two short Mn-Mn distances. We extend this concept by examining how, in combination with protonation of His337, the Mn oxidation states and relative energetics are affected. We use O4 (OH^-) while His337 was kept neutral (HIE) (Figure 2.9). The resulting configuration is in III-IV-III-II oxidation state and presents two short Mn-Mn distances, consistent with EXAFS data. Moreover, it has 1.6 kcal/mol lower energy than the III-III-III-III isomer (S_1L_3Hb_HIE).

We see that OEC models under the low oxidation state paradigm are readily able to produce two short Mn-Mn distances with the mixed valence oxidation state (III, IV, III, II), which can be obtained and stabilized by varying the protonation states of His337 (neutral vs. protonated), O5 (as H_2O in S_1L_4H in Figure 2.5) and O4 (as OH^- together with HIE). Since we ruled out the latter two possibilities in Sections 2.3.1 and 2.3.2, the most likely way to generate two short Mn-Mn distances is to use neutral His337 (S_1L_3Hc_HIE in Figure 2.8B).

In summary, we conclude that it is possible to rationalize the geometry changes between 1.9 Å XRD and 1.95 Å XFEL structures under the low paradigm with the same mixed valence oxidation pattern (Figure 2.8), but with different protonation states compared with Petrie's scheme[62]. To explain the geometry differences between them under the high paradigm, we must assume that the 1.9 Å XRD structure suffers from

radiation-induced damage, leading to some reduced S state or even a mixture of different reduced S states. Furthermore, the XFEL structure was proposed to comprise a mixture of S_0 and S_1 states under the high paradigm[1][99]. Our calculations show this requirement disappears when the low paradigm is adopted. Lastly, the low paradigm can account for the presence of two short Mn-Mn distances in the S_1 state simply by invoking the correct protonation pattern as in Figure 2.8. This is a major finding of the present work.

2.4 Conclusions

An extensive water network is crucial for correctly modeling the protonation and Mn oxidation states of the OEC. Internal proton transfer steps and proton release to bulk water during the reaction cycle influence the redox potential of each transition (Si→Sj) and the distribution of individual Mn oxidation states. This leads to a natural regulation of Photosystem II turnover by the external pH of the medium. The QM/MM method we adopted generates plausible water networks and protein environment around the OEC cluster. We examined numerous protonation models under both low and high oxidation state paradigms for the S_0 and S_1 states, more so than reported in previous publications[56, 1].

For the bridging oxygens: O1, O2, and O4, we concluded the protonation states should be considered as O^{2-} in the S_1 state. Otherwise, the corresponding Mn-Mn distances (Mn1-Mn2, Mn2-Mn3 or Mn3-Mn4) would become unacceptably long, which is incompatible with the XFEL structure and EXAFS Mn-Mn distances. The protonation state of O3 should be considered together with His337, because of the strong H-bonding between them. Both proton states of His337, HIP and HIE, can produce the mixed-valence III-IV-III-II isomer, which has unprotonated O3 and exhibits two short Mn-Mn distances. Hence, O3 should be in the form of O^{2-}. The main reason to choose HIE over HIP is to further stabilize the III-IV-III-II isomer.

We examined a number of factors that influence the Mn-Mn and Mn-O5 distances. Models under either low or high paradigms can produce two short Mn-Mn distances, as

seen in EXAFS measurements. On this basis, the low oxidation state paradigm cannot be ruled out. Based on the comparisons of Mn-Mn and Mn-O5 distances, we ruled out the possibility of having O5 as water ligand or O^{2-} in S_1. We conclude that the position of O5 in the XFEL structure is more consistent with an OH^- under the low paradigm. We disfavor high paradigm models because the Mn3-O5 cannot be correctly reproduced with either OH^- or O^{2-}.

The differences between the 1.9 Å XRD and 1.95 Å XFEL structures can be reconciled by oxidation state redistribution possibly with simple proton relocations at His337 under the low paradigm, or by radiation-induced damage assumption under the high paradigm. The protonation states of the bridging oxygens and His337 determines whether elongation or shortening of Mn-Mn distances occurs, which in turn biases the choice between high vs low oxidation state paradigms. Note, however, that high paradigm S_1 models can produce three short Mn-Mn distances[1] (also observed in S_1H_1H and S_1H_2Ha in Figure 2.7), whereas low paradigm S_1 models only have two short Mn-Mn distances. We think it is not a decisive factor, since either two or three short Mn-Mn distances have been suggested by different groups[22, 24]. We conclude that the scheme under low paradigm seems to be more straightforward and natural. These calculations alone do not resolve the debate between the low and high oxidation state paradigms, but the new insights from the present work should be of value to understand the fundamentals of the oxygen evolving complex in Photosystem II. Our conclusions are consistent with the results by Petrie *et al.*[61, 62] and in contrast to earlier reports suggesting that the high oxidation state paradigm is better at fitting the structural data[1, 63, 78].

In Section 2.3.2 we noted that when 4 protons are present in configuration S_1H_4H, which is also the S_3 state under the low paradigm, a rearrangement of D1-Asp170 occurs from bidentate (Mn4, Ca) to bidentate (Mn4, O5 (OH^-)). This is mechanistically significant, as it suggests a potential functional role for the two carboxylate ligands to Mn4 in substrate water deprotonation. This type of chemistry has precedent in synthetic water oxidation catalysts. For example, an analogous H-bonded intermediate occurs in the mechanism of water oxidation by the Co-cubane compound[13], where

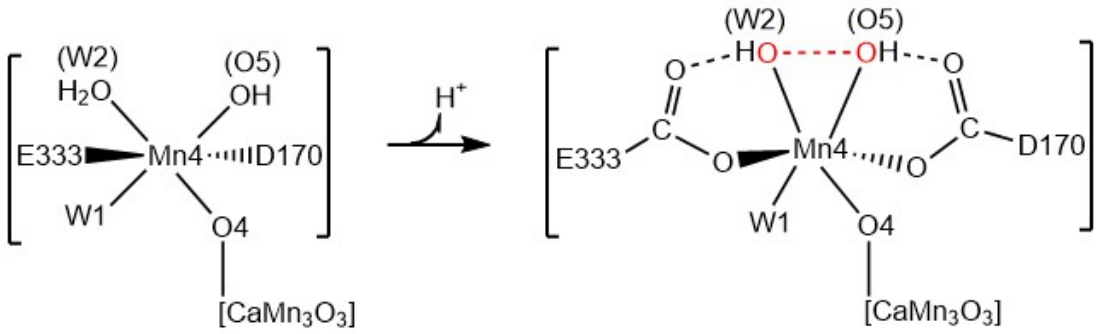

Figure 2.10: Proposed formation of geminal hydroxo-carboxylato in the OEC prior.

two hydroxides (OH^-) insert into Co-O (carboxylate) bonds on the same Co atom by bridging between Co and two carboxylates. This reaction is energetically favored and the resulting geminal hydroxides (μ'-OH^-)$_2$ go on to react to form O2 upon further two-electron oxidation[13]. A crystallographically characterized example of an analogous H-bonded structure occurs in the insertion reaction of methanol with the Mn-cubane, where a molecule of methanol inserts into a Mn-O (Phoshinate) bond[101]. By analogy in the OEC, Mn4 has two such μ-carboxylate ligands (D1-Asp170 and D1-Glu333) and they are potential H-bond acceptors for analogous hydroxide insertion steps that form a pair of geminal hydroxo-carboxylato on Mn4(O5)(W2), involving O5 (OH^-) and following deprotonation of W2 (H_2O) (depicted in Figure 2.10). Future computational studies of the OEC in the S_2 and S_3 states may better assess whether this proven pathway for water oxidation observed in synthetic cubane clusters may be applicable to the OEC.

Chapter 3

Reconciling Structural and Spectroscopic Fingerprints of the Oxygen Evolving Complex Photosystem II: A Computational Study of the S_2 State

3.1 Overview

As mentioned in Section 1.2.2, the MLS and $g \approx 4.1$ are interconvertible under certain circumstances and the $g \geq 4.1$ signals vary depending on illumination temperature. Pantazis *et al.* proposed two S_2 models, which differ mainly in the position of the O5 bridge and where the unique Mn^{III} ion in high paradigm resides, to explain this phenomenon[47]. In one form, O5 is bound to Mn4 with oxidation state III-IV-IV-IV (ordered from Mn1 to Mn4), corresponding to an "open" cubane structure with $S_{GS} = 1/2$ associated with the MLS; in the other form, O5 is bound to Mn1 with oxidation state IV-IV-IV-III, corresponding to a "closed" cubane structure with $S_{GS} = 5/2$ likely associated with the $g \approx 4.1$ signal. This idea was also supported by Guidoni *et al.* through quantum mechanics/molecular mechanics (QM/MM) simulations on PSII, assuming high paradigm[83]. Moreover, the "closed" form was found to have very small energy separation between the ground and first excited states, rendering the energy gap sensitive to perturbations, which in turn was proposed to explain the observation that the $g \geq 4.1$ signals vary depending on illumination temperature[47].

It is of great interest to see whether similar conclusions about S_2 state could be reached under the low paradigm. Terrett *et al.* proposed two low-paradigm S_2 models, distinguished by the relative arrangement of the D1-Asp170 group and associated water ligands in the structure and designated "wet" and "dry"[102]. They proposed a "Coupled Dimer" model of magnetic interaction[102], in which one dimer (Mn1 and Mn2) is anti-ferromagnetically coupled internally, with net spin 1/2, and the other dimer (Mn3

and Mn4) is also anti-ferromagnetically coupled internally, with net spin ≈ 0. Hence, both "wet" and "dry" forms have $S_{GS} = 1/2$. Krewald *et al.* investigated various S_2 configurations with different protonation states of the OEC, where two or three protons are distributed among O4, O5, and W2[1]. The only LOP configuration with $S_{GS} = 5/2$ they obtained has 23 kcal/mol higher energy than the lowest energy configuration with $S_{GS} = 1/2$. Therefore, they claimed that S_2 models in the LOP are not consistent with the EPR data. A recent ^{55}Mn-ENDOR report by Jin *et al.*[6] indicates three Mn^{III} ions are likely present in the functional MLS S_2 state of spinach PSII cores, supporting the LOP. They rationalize the complex spectrum by assuming a dimer-of-dimers exchange coupling topology for the four ^{55}Mn hyperfine tensors: one unusually large highly anisotropic, one medium highly anisotropic, one small highly anisotropic and one very small isotropic tensors. However, Krewald *et al.*[1] reported that they were not able to reproduce these results using either cyanobacterial or plant PSII cores and instead their ^{55}Mn-ENDOR data are consistent with a tetramer-like exchange coupling topology, resulting in similar isotropic hyperfine couplings for all four Mn ions. They do not compute hyperfine tensor anisotropies and completely ignore discussion of the topic. We reexamine this question here, focusing on a wider range of possible protonation states, estimating *via* quantum chemistry calculations the geometric, energetic, and spectroscopic properties of the OEC in the S_2 state.

3.2 Theoretical Background

The theoretical background of the EPR simulation and the calculation of EPR parameters by density functional theory (DFT) methods have been described in many places[103, 104, 105, 64]. Here we summarize aspects that are relevant to exchange coupling parameter, spin-projection coefficient and hyperfine coupling constant calculations.

3.2.1 Heisenberg-Dirac-Van Vleck Hamiltonian

With multiple transition metals, the orientation of the spins on different metals affects the total energy, and can be approximately expressed via the HeisenbergDiracvan Vleck (HDvV) spin Hamiltonian,

$$\boldsymbol{H} = -2\sum_{i<j} J_{ij}\boldsymbol{S}_i\boldsymbol{S}_j \tag{3.1}$$

where J_{ij} is the exchange interaction parameter between $\boldsymbol{S}_i$ and $\boldsymbol{S}_j$. One tractable way to estimate the magnetic interactions among the manganese ions is to construct the broken-symmetry (BS) states within the unrestricted Kohn-Sham DFT method[106, 107], which tries to obtain a wave function that breaks spatial (and spin) symmetry by allowing different spatial orbitals for the two spin quantum states, α and β.

With N centers, there are $2N$ distinct spin configurations, assuming the centers have all spins locally are aligned in parallel fashion, as α and β. Since two configurations are equivalent if the corresponding $\boldsymbol{S}_i$'s are all inverted, the total number of distinct configurations is reduced to $2N-1$, which results in eight states, for whose energies can be estimated by DFT: one high-spin state (where all site spins are aligned in a parallel fashion), and seven BS single-determinant representations (Eq. 3.2).

$$E(S_k) = -2\sum_{i<j} J_{ij}M_{S,i}M_{S,j} + E_0; M_{S,i} = \pm S_i, \sum_i M_{S,i} > 0, k = M_{S_t} \tag{3.2}$$

There are six possible pairwise exchange couplings (indicated in Figure 3.1), yielding states with total spin S_T a good quantum number. These energy differences among the eight DFT states were fit with six exchange coupling parameters and E_0 (an offset value) as adjustable parameters, using a least squares method. Having obtained the exchange coupling parameters, it is straightforward to assign and diagonalize the HDvV Hamiltonian matrix to estimate the energies of the pure (total) spin states, which cannot be obtained directly from single-determinant DFT calculations. Energies, spin states, and molecular properties can then be related to the experiment. As we discuss below, in cases where some of the exchange coupling parameters are much larger than others, one can obtain simpler results that are amenable to more qualitative interpretation.

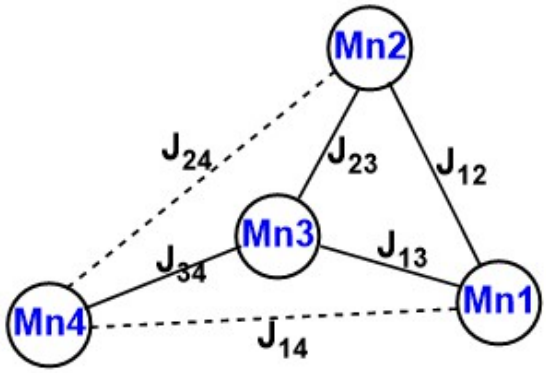

Figure 3.1: Exchange interaction pattern between Mn ions of OEC.

3.2.2 Hyperfine Coupling Constants and Spin Projection Coefficients

Extraction of the magnetic dipolar portion of the individual ^{55}Mn hyperfine tensors and the cluster g tensor are the main goals of analysis of the experimental EPR and ENDOR spectra, as these inform on the oxidation states and electronic spin. The empirical (spin) Hamiltonian appropriate to describe EPR spectra can be written as the sum of terms for the individual spin centers plus the HDvV model for the exchange interaction (Eq. 3.3)[104].

$$\boldsymbol{H} = \sum_i (\beta \boldsymbol{B} \boldsymbol{g}_i \boldsymbol{S}_i + \boldsymbol{S}_i \boldsymbol{a}_i \boldsymbol{I}_i + \boldsymbol{S}_i \boldsymbol{D}_i \boldsymbol{S}_i) - 2 \sum_{i<j} J_{ij} \boldsymbol{S}_i \boldsymbol{S}_j \tag{3.3}$$

where $\boldsymbol{B}$ is the external magnetic field. $\boldsymbol{S}_i$ and $\boldsymbol{I}_i$ are the corresponding spin and nuclear spin operators. $\boldsymbol{g}_i$, $\boldsymbol{a}_i$, and $\boldsymbol{D}_i$ are the Zeeman, intrinsic hyperfine, and zero-field splitting (ZFS) tensors of spin center i. (In what follows, we will assume, as do others[108, 109, 110], that all Mn-Mn couplings are large ($|J| \gg D_i$), i.e. within the strong exchange limit, so that the terms involving $\boldsymbol{D}$ can be neglected.) In the spin-coupled representation (Eq. 3.4), the individual ion spins are strongly coupled to the total spin $\boldsymbol{S}_T = \sum_i \boldsymbol{S}_i$, and this allows the g and hyperfine tensors to be related to the experimental spectra[32], using the vector spin-coupling rule[104].

$$\boldsymbol{H}_{coupled} = \beta \boldsymbol{S}_T \boldsymbol{G} \boldsymbol{B} + \sum_i \boldsymbol{S}_T \boldsymbol{A}_i \boldsymbol{I}_i \tag{3.4}$$

where $\boldsymbol{G}$ is the effective g tensor for the coupled spin state $\boldsymbol{S}_T$ and $\boldsymbol{A}_i$ is the effective hyperfine coupling (HFC) tensor. Hyperfine coupling refers to the interaction between

an unpaired electron and nearby nuclear spins and $\boldsymbol{A}_i$ generally can be represented by the sum of an isotropic part (A_{iso}), which predominately arises from the Fermi contact interaction, and an anisotropic part ($\boldsymbol{A}'$), which is customarily dominated by the electron-nuclear magnetic dipolar interaction in systems without ZFS.

$$\boldsymbol{S}_T\boldsymbol{A}_i\boldsymbol{I}_i = A_{iso}\boldsymbol{S}_T\boldsymbol{I}_i + \boldsymbol{S}_T\boldsymbol{A}'_i\boldsymbol{I}_i \tag{3.5}$$

The effective (cluster) tensors $\boldsymbol{A}_i$ are also related to the intrinsic (atomic) hyperfine tensors $\boldsymbol{a}_i$ via a 3×3 projection matrix $\boldsymbol{\rho}_i$, which depends on the spin at site i, on the exchange coupling constants of the $\boldsymbol{S}_T$ multiplets, and on the ZFS tensors[108, 110]. The complexity comes from ZFS interactions, which admix the pure (total) spin states when ZFS is not ignorable relative to the HDvV exchange energy differences ($\boldsymbol{D}_i/J_{ik}$), resulting in the appearance of anisotropy of $\boldsymbol{\rho}_i$. As discussed in section 3.4, Mn^{III} ZFS is large and this assumption is inaccurate. In this case, because the admixed total spin states are no longer pure spin states (they are not eigenfunctions of $\boldsymbol{S}_T$), the resulting ZFS anisotropy in Eq. 3.4 gets lumped into the hyperfine tensor. This "transfer of ZFS into the hyperfine tensor"[108, 111] means that the cluster HFC tensor will be anisotropic, even if its intrinsic HFC tensor is isotropic. Since the strong exchange limit is adopted, the ZFS terms are neglected and projection matrix $\boldsymbol{\rho}_i$ is reduced to scalars p_i (projection coefficients)[112]. Hence, we have a simplified equation

$$\boldsymbol{A}_i = p_i\boldsymbol{a}_i \tag{3.6}$$

Pantazis *et al.* developed a methodology, which has been applied to several models of the OEC[47, 110, 113], to calculate the HFCs from BS-DFT (detailed descriptions of the theory are in reference[114]). This is also the method we use in the present work. In short, the intrinsic hyperfine tensors $\boldsymbol{a}_i$ are related to the computed hyperfine tensors of the BS state $\boldsymbol{A}_i^{BS}$ [114].

$$\boldsymbol{a}_i = \pm\boldsymbol{A}_i^{BS}\left(\frac{\langle S_z\rangle_{BS}}{S_i}\right) \tag{3.7}$$

where $\langle S_z\rangle_{BS} = M_{S_T}$ is the total M_S of the BS wave function and the sign depends on the formal orientation of the local spin in the BS solution. (One may alternatively take the intrinsic hyperfine tensors from experimental results for individual (non-cluster) Mn

model compounds with similar ligand environments[32, 108], which give qualitatively similar results and hence are not pursued further in the present work.) The projection coefficients are given as the ratio of the on-site spin expectation $\langle S_{z,i} \rangle$ to the total ground state spin S_T.

$$p_i = \frac{\langle S_{z,i} \rangle}{S_T} \tag{3.8}$$

$$\langle S_{z,i} \rangle = \sum_{S_1 M_{S_1} \cdots S_n M_{S_n}} |C_0^{S_1 M_{S_1} \cdots S_n M_{S_n}}|^2 M_{S_i}, i = 1, \cdots, n \tag{3.9}$$

where $n = 4$ for the OEC, and $C_0^{S_1 M_{S_1} \cdots S_n M_{S_n}}$ are the expansion coefficients of the ground spin state corresponding to the lowest eigenvalue of the HDvV matrix after its diagonalization. Note that, the eigenstates obtained this way are normally degenerate; hence we applied perturbation theory to break the degeneracy. The perturbation term is ϵS_z, where ϵ was set to be a small number ($1e-5$). In this way, the solutions are also eigenfunctions to S_z.

The programs for exchange coupling calculation and Hamiltonian matrix diagonalization are shown in Appendix A.

3.3 Methodology

3.3.1 Construction of Structural Models

The S_2 models are derived from the QM model of the S_1 state (see Section 2.2.1).

3.3.2 Computational Details

Geometry optimization calculations apply the same method described in Section 2.2.3.

Broken Symmetry and HFCs Calculations. For the broken-symmetry (BS) calculations and all HFCs calculations, the TPSSh functional[115] was used. Def2-TZVP were applied on all elements. The auxiliary basis sets (def2-TZVP/J) were used for the RI and chain-of-spheres (COSX) approximations for the Coulomb and exact exchange[116]. For broken-symmetry calculations, different spin configurations were generated using the "FlipSpin" feature of ORCA[85]. Manganese isotropic hyperfine

coupling constants A_{iso} were calculated from Fermi contact terms, arising from the finite spin density on the nucleus under investigation. Traceless anisotropic dipolar HFCs were calculated from the dipolar contributions, arising from the interaction of the ^{55}Mn nuclear moment witht the electron magnetic moment distributed across the cluster. The second order contribution to the HFC from spin-orbit coupling was also included, which for the idealized case of pure (total) spin states we find is about a order of magnitude smaller. The triply polarized basis set CP(PPP), which was described to be particularly flexible in the core region and provide results close to the basis-set limit for the isotropic contribution to the HFC[117, 118], was used for manganese, while def2-TZVP were used for the remaining atoms. The integration grid for the manganese atoms was increased to 7 to ensure the numerical accuracy of results.

Transition State Calculation. The transition state (TS) was estimated by relaxed scans along the isomerization coordinate in step size of 0.05 Å. At each step, the structure was optimized assuming high spin configuration. The energy obtained this way was suggested to be an upper bound to the true barrier, since the approximate TS is unrelaxed with respect to the TS mode and subject to backbone constraints[47].

3.4 Results and Discussion

We focus on configurations for S_2 state in the low paradigm and evaluate them in terms of the geometric, energetic, electronic, and spectroscopic properties. We rely on the extended X-ray absorption fine structure (EXAFS), which provides geometric structure information in terms of intermetallic distances and is believed to be the most reliable data set for metal-metal separations within the OEC. The EXAFS data sets imply the existence of two or three short Mn-Mn distances of about 2.7 Å for S_2[21, 24, 59]. One key EPR experimental observation that must be satisfied for S_2 state is the potential to interconvert between the low spin ($S_{GS} = 1/2$) and high spin ($S_{GS} = 5/2$) forms with a low barrier. Two interconvertible high paradigm S_2 configurations have been reported by Pantazis *et al.*[47]. Their **A** and **B** (i.e. "open" and "closed") forms have localized Mn valencies (III,IV,IV,IV vs. IV,IV,IV,III) with ground spin states 1/2 and 5/2, respectively, and differ in the position of O5.

In the present study, we try to explain the EPR phenomenon in a similar way under the low paradigm. Krewald *et al.* investigated various low-paradigm S_2 configurations with W1 in the form of H_2O, His337 in the form of HIP, and two or three protons distributed among O4, O5, and W2[1]. We assume O4 is unprotonated and O5 can be either O^{2-} or OH^-, in agreement with others[63]. As a result, with two protons, we have two protonation configurations O5 (OH^-) + W2 (OH^-) and O5 (O^{2-}) + W2 (H_2O), while with three protons, we only have O5 (OH^-) + W2 (H_2O). States with a neutral His337 are discussed in Section 3.4.4. Note that the same protonation state of the OEC may have different structural isomers, due to different geometries or oxidation state patterns. Moreover, the electronic and spectroscopic properties of the OEC are sensitive to structural difference. Hence, although some of the same protonation states have been considered by Krewald *et al.*[1], different ground spin states are discovered.

The nomenclature refers to the S_i state, the Mn oxidation state (low or high paradigm), and the total number of protons distributed on O5 and W2. Configurations with O5 (OH^-) + W2 (OH^-) are named by S_2L_2H1, plus a letter indicating different geometries or oxidation state patterns. Configurations with O5 (O^{2-}) + W2 (H_2O) starts the labeling with S_2L_2H2. Configurations with O5 (OH^-) + W2 (H_2O) starts with S_2L_3H. His337 is assumed to be positive (i.e. HIP) by default and will be included in the name only if neural histidine (i.e. HIE) is used, e.g. S_2L_3Ha_HIE refers to the same configuration as S_2L_3Ha but with neural His337.

3.4.1 Isomers with O5 (OH^-) + W2 (OH^-)

Five configurations with O5 (OH^-), W2 (OH^-), and His337 (HIP) have been obtained (S_2L_2H1a-e in Figure 3.2). The manganese oxidation states were assigned by the Mulliken spin population analysis (Table 3.1). For each configuration, a series of broken symmetry calculations have been conducted. The exchange coupling parameters and energy level spin ladders are then computed to determine the corresponding ground and first excited states and the energy gap between them.

With the same protonation states, these configurations have different oxidation state

Table 3.1: Mulliken spin populations of Mn ions for geometry optimized models with two protons on O5 and W2, and positive His337 (HIP).

	Mn1	Mn2	Mn3	Mn4
S_2L_2H1a	3.92	2.94	3.88	3.91
S_2L_2H1b	3.94	2.95	3.86	3.91
S_2L_2H1c	3.94	3.85	2.92	3.90
S_2L_2H1d	3.91	3.87	2.93	3.90
S_2L_2H1e	3.92	2.92	2.90	4.78
S_2L_2H2a	3.96	2.91	2.75	4.84
S_2L_2H2b	3.92	2.91	2.85	4.83
S_2L_2H2c	3.94	3.86	2.95	3.88

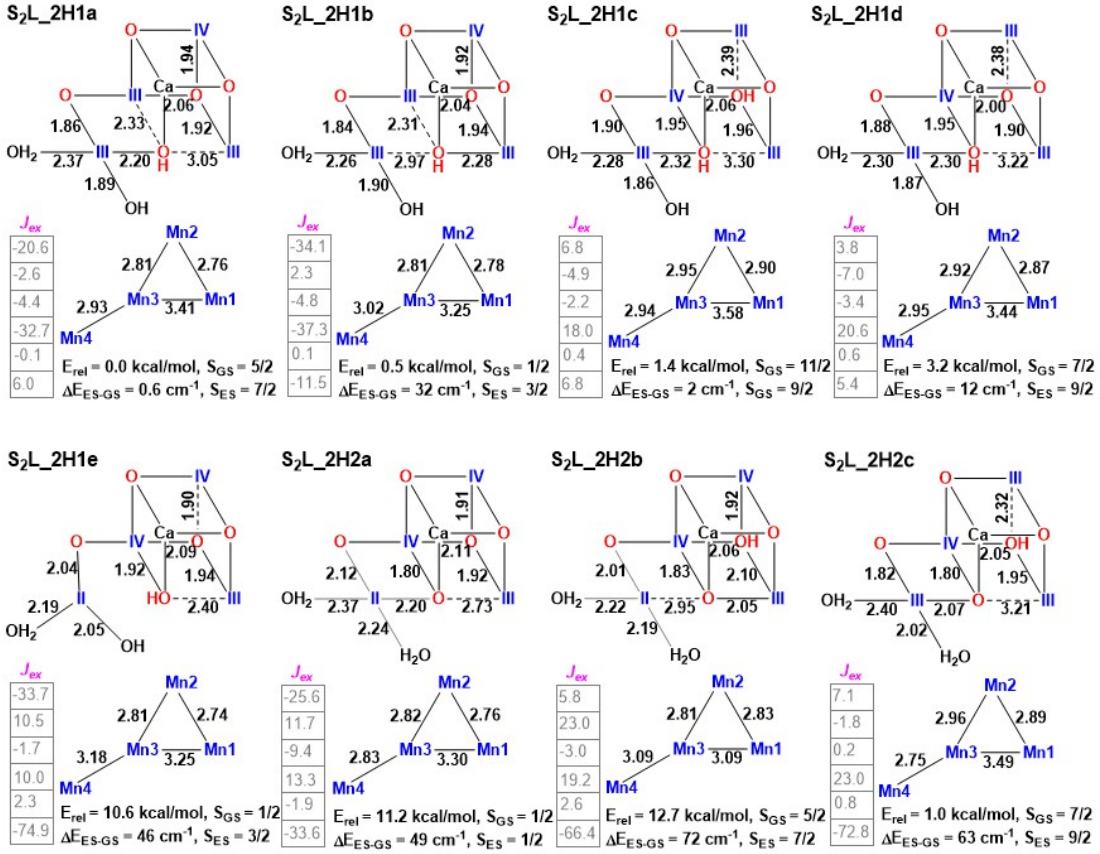

Figure 3.2: Geometries, energetic, and spectroscopic properties of S_2L isomers with various protonation and oxidation states in the low oxidation paradigm. Positive His337 (HIP) is assumed. S_2L_2H1a-e are configurations with O5 (OH^-) + W2 (OH^-). S_2L_2H2a-c are configurations with O5 (O^{2-}) + W2 (H_2O). The values in grey columns are the exchange coupling parameters (cm^{-1}) and ordered as J_{12}, J_{13}, J_{14}, J_{23}, J_{24}, and J_{34}. ΔE_{ES-GS} is the energy gap (cm^{-1}) between the ground spin state (GS) and first excited state (ES). The relative energies are compared with that of S_2L_2H1a.

patterns or geometries. S_2L_2H1a and S_2L_2H1b share the same oxidation pattern (III-IV-III-III), while S_2L_2H1c and S_2L_2H1d share the same oxidation pattern (III-III-IV-III). These four configurations have close energies. The fifth configuration, S_2L_2H1e, contains a Mn^{II} ion with a trigonal bipyramidal ligand field around Mn4 and has much higher energy than others. Note that, S_2L_2H1b and S_2L_2H1d are very similar to the "S_0H-1c" and "S_0H-1b" states studied by Krewald *et al.*[1] with respect to Mn-Mn distances and ground spin states.

In terms of the geometries of these structures, S_2L_2H1a, S_2L_2H1b, and S_2L_2H1e have two short Mn-Mn distances, qualitatively matching the EXAFS data. Although the Mn-Mn distances are slightly larger than the EXAFS data, it is known that DFT methods tend to overestimate Mn-Mn distances, as seen both in our work and studies of other groups[46, 119] (where both BP86 and hybrid functionals are used). As for S_2L_2H1c and S_2L_2H1d, long Mn1-Mn2 and Mn2-Mn3 distances are produced, which is very likely the result of the Jahn-Teller effect of Mn2(III), where the asymmetric electronic distribution of the valence orbitals orients the empty orbital towards O3. S_2L_2H1a and S_2L_2H1b also have slightly lower energy than S_2L_2H1c and S_2L_2H1d. It is clear that low paradigm configurations are able to satisfy the EXAFS requirement with appropriate oxidation state pattern.

Looking at the position of O5 in S_2L_2H1a and S_2L_2H1b (Figure 3.2), we find these two are analogous to the high paradigm "open" and "closed" forms described by Pantazis *et al.*[61]. We denote S_2L_2H1a as the open form and S_2L_2H1b as the closed form, based on the Mn1-O5 and Mn4-O5 distances. In the open form, O5 is close to Mn4 with length 2.2 Å and away from Mn1 (3.05 Å), hence the Mn_3Ca cube is open and Mn1 remains pentacoordinate. In the closed form, O5 is close to Mn1 (2.28 Å) and away from Mn4 (2.97 Å). The energy level spin ladder reveals that S_2L_2H1a and S_2L_2H1b have ground spin states $S_{GS} = 5/2$ and $S_{GS} = 1/2$, respectively. The former may account for the broad EPR signal at $g \approx 4.1$, while the later corresponds to the multiline signal at $g = 2.0$. Note that our open and closed forms under the low paradigm exhibit opposite ground spin states compared to the high-paradigm models studied by Pantazis *et al.*[47]. These states differ in energy by only 0.5 kcal/mol.

We calculated the energy profile to examine the conversion between S_2L_2H1a and S_2L_2H1b (Figure 3.3A). The energy profile clearly indicates a sufficiently low barrier ($\leq$ 1.5 kcal/mol) and the interconversion of the two structural forms under physiological conditions is allowed. Moreover, such a low barrier demonstrates the large flexibility of the O5 (OH^-) and has been interpreted to suggest the possibility of an additional water molecule entering this space perhaps as another substrate water[44, 120]. Figure 3.3B shows the corresponding exchange coupling constants along the reaction coordinate. In general, J_{24} is relatively small, which is expected from the topology of the OEC (the dangling Mn4 is remote from Mn2). Although affected, both J_{12} and J_{23} stay very negative, which indicates strong anti-ferromagnetic interactions. Interestingly, J_{13}, J_{14} and J_{24} show some quite different features. As O5 moves from Mn4 to Mn1, J_{13} and J_{24} cross each other and flip signs, while J_{14} decreases to a minimum and then increases. Moreover, when $d_{\text{Mn4-O5}} \approx d_{\text{Mn1-O5}} \approx 2.5$ Å, which is also the cross point, both J_{13} and J_{24} vanishes. J_{14} reaches the minimum at $d_{\text{Mn4-O5}} \approx 2.6$ Å. This behavior can be explained by the geometric changes along the reaction coordinate, i.e. Mn1-Mn3 decreases, Mn3-Mn4 increases, and Mn1-Mn4 first decreases and then increases (with minimum Mn1-Mn4 distance at $d_{\text{Mn4-O5}} \approx 2.6$Å). Clearly, the exchange interactions depend not only on the protonation and oxidation states, but also heavily on the corresponding Mn-Mn distances, which are altered by the movement of O5. This is fully expected based on how the ligand field strength directly influences electron energies.

Regarding the energy difference between excited states and the ground state corresponding to the $g = 2.0$ multiline signal in S_2 state, the experimental value[121, 122], obtained *via* temperature dependence predicted for an Orbach relaxation mechanism, is 35 cm^{-1}. S_2L_2H1b is very close to this, with $\Delta E_{ES-GS} = 32$ cm^{-1} (Figure 3.2). However, the accuracy of the energy separations is limited by neglect of ZFS contributions, and is likely to be sensitive to the functional used[114].

We also noticed that S_2L_2H1a has a very compressed energy ladder (e.g. $\Delta E_{ES-GS} <$ 1 cm^{-1}); hence, as suggested by Pantazis el al.[47], the ground state may not be considered well-isolated and perturbations, such as illumination temperature changes, may

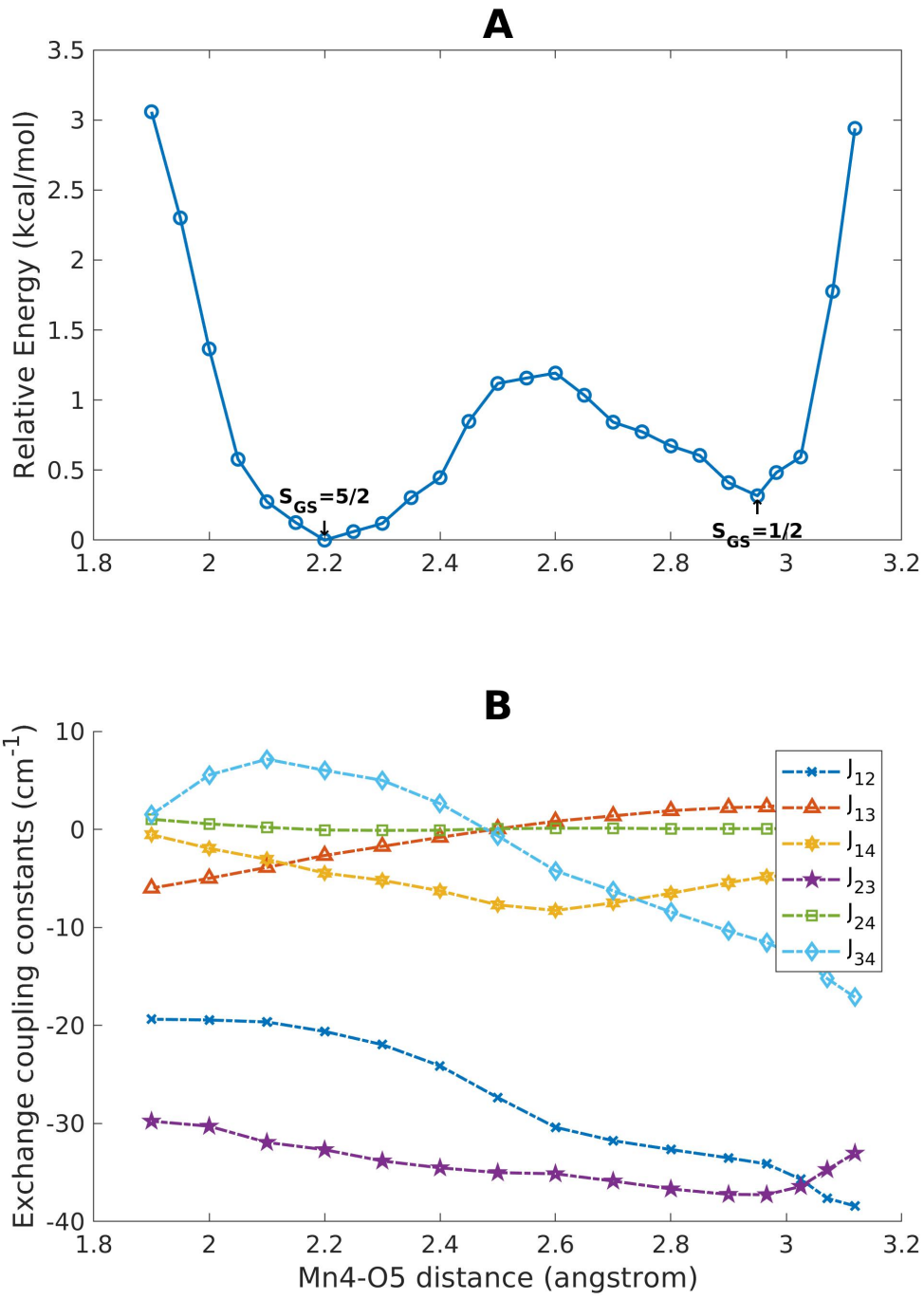

Figure 3.3: Energy profile of interconversion between S_2L_2H1a ($S_{GS} = 5/2$) and S_2L_2H1b ($S_{GS} = 1/2$) and the corresponding J couplings.

change the energy gap, which could explain the observation that the two $g = 10$ and 6 signals vary depending on illumination temperature. Indeed, it turns out the electronic property of S_2L_2H1a is very sensitive to exchange coupling constants. For example, if we alter J_{34} while all other J's are fixed, J_{34} needs to be within the range [3.72, 6.08] (cm^{-1}) in order to obtain $S_{GS} = 5/2$. Alternatively, a more straightforward explanation can be obtained by considering S_2L_2H1c and S_2L_2H1d, which also have relatively compressed energy ladders and different ground spin states, $S_{GS} = 11/2$ and $S_{GS} = 7/2$, respectively. S_2L_2H1c and S_2L_2H1d differ in the position of N_ϵH of His337, which is bonded to O3 in S_2L_2H1c and returns to N_ϵ of His337 in S_2L_2H1d. Perturbations, such as the change of the oxidation state pattern (from III-IV-III-III to III-III-IV-III) or hydrogen-bonding network (movement of N_ϵH from His337 towards O3), could easily lead to different electronic properties. S_2L_2H1c and S_2L_2H1d may also account for the signals at $g = 10$ and 6[34]. As a result, our low paradigm configurations with O5 (OH^-), W2 (OH^-), and His337 (HIP) can readily explain the EPR observations.

3.4.2 Isomers with O5 (O^{2-}) + W2 (H_2O)

Three isomers with O5 (O^{2-}) and W2 (H_2O) have been examined (S_2L_2H2a-c in Figure 3.2). The first two (S_2L_2H2a and S_2L_2H2b) are Mn^{II}-containing and share the same oxidation state pattern (III-IV-IV-II) while the third, S_2L_2H2c, has III-III-IV-III. The N_ϵH of His337 moves to O3 in both S_2L_2H1b and S_2L_2H1c. S_2L_2H2c with $S_{GS} = 7/2$ has very close energy to S_2L_2H1a and can also be considered as a candidate for the $g = 10$ and 6 EPR signals.

A Mn^{II}-containing state in S_2 was previously considered by Krewald *et al.*[1], e.g. "S_2L-3c" in their notation has oxidation pattern (IV-III-IV-II). We examined this configuration and found it has an unreasonable high energy compared to other configurations that have different protonation and oxidation state patterns that we report next. Similar to their results[1], Mn^{II}-containing isomers with six-coordinate ligand fields and two low protonation state all show much higher energies, e.g. S_2L_2H2a and S_2L_2H2b have more than 10 kcal/mol higher energies than S_2L_2H1a-d. However, energy accessible Mn^{II}-containing isomers can be obtained, which is shown in Section 3.4.4. Here,

we examine them to see whether the corresponding analogous "open" and "closed" forms with O5 (O^{2-}) + W2 (H_2O) give the same ground spin states as S_2L_2H1a and S_2L_2H1b. Note that, the broken-symmetry (BS) model[106], which assumes the Mn ions have all spins fully polarized locally, as α or β, of Mn^{II}-containing isomer under the low paradigm is able to get a $S = 5/2$ BS state, i.e. $Mn^{III\text{-}IV\text{-}IV}$ spin up and Mn^{II} spin down.

S_2L_2H2a and S_2L_2H2b differ in the protonation state of O3, caused by movement of N_ϵH of His337, and the position of O5. Geometrically, these isomers match the EXAFS data, with S_2L_2H2a having three relatively short Mn-Mn distances (2.76, 2.82, 2.83 Å) and S_2L_2H2b having two (2.83, 2.81 Å). The S_2L_2H2a has an "open" form with $S_{GS} = 1/2$ while S_2L_2H2b has a "closed" form with $S_{GS} = 5/2$, obtained from the energy spin ladder (Figure 3.2). These structures are candidates for the S_2 MLS and $g \approx 4.1$ EPR spectral forms. The energy profile of the OEC obtained upon moving O5 between Mn1 and Mn4 indicates that interconversion between the open and closed forms has a low barrier, as shown in Figure 3.4. As O5 moves from Mn4 to Mn1, the N_ϵH of His337 is transferred from N_ϵ to O3. The movement of this proton compensates the negative charge of O5 as it moves closer inside the Mn_3Ca cube.

The lowest energy broken-symmetry configurations, corresponding to open (S_2L_2H2a) and closed (S_2L_2H2b) forms, are shown in Figure 3.5. The latter has $S = 5/2$ with Mn1, Mn2 and Mn3 in the cubane coupled by mutual ferromagnetic interactions, giving the Mn_3Ca cubane a high-spin $S = 5$. The Mn_3Ca cubane subspin then couples antiferromagnetically with the dangling Mn4, resulting in total spin state $S_T = 5/2$. Moreover, among all the basis functions for constructing the corresponding HDvV Hamiltonian matrix, these two BS states (with $M_{S_T} = 1/2$ and $5/2$) have the lowest energies and are used for later HFC calculations.

These Mn^{II}-containing open and closed forms (S_2L_2H2a and S_2L_2H2b) have the same ground spin states compared to the HOP study by Pantazis *et al.*[47], which are opposite to those of S_2L_2H1a and S_2L_2H1b. The differences between S_2L_2H1a/b and S_2L_2H2a/b include the protonation state of O5, and the oxidation state pattern, both of which may change the exchange couplings significantly. For example, S_2L_2H1a/b,

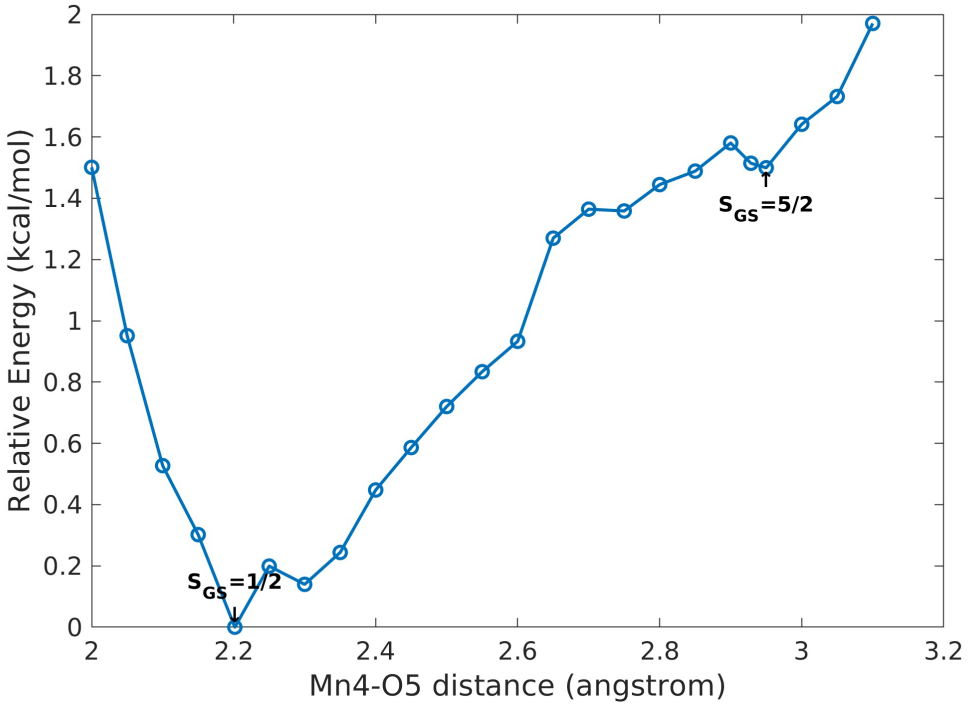

Figure 3.4: Energy profile of interconversion between S_2L_2H2a ($S_{GS} = 1/2$) and S_2L_2H2b ($S_{GS} = 5/2$).

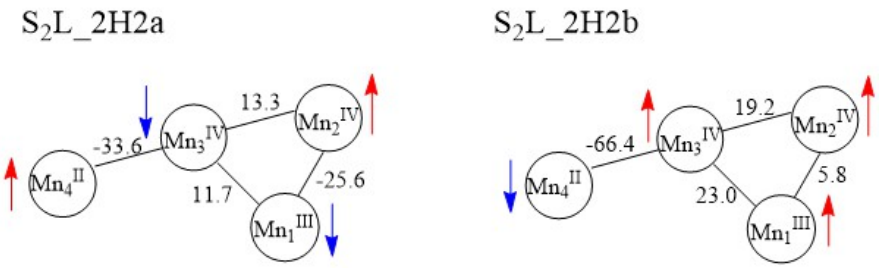

Figure 3.5: Computed nearest-neighbor exchange coupling parameters (cm^{-1}) and lowest BS configurations of S_2L_2H2a and S_2L_2H2b.

with Mn3(III), are the only isomers with large negative J_{23} (Figure 3.2), which implies anti-ferromagnetic interaction between Mn2 and Mn3, while the rest have positive J_{23}. Different exchange couplings then may predict quite different electronic properties, as we see here.

3.4.3 Isomers with Three Protons on O5 and W2

With three protons distributed on O5 and W2, the protonation states are fixed as O5 (OH^-) and W2 (H_2O). For configurations with protonated His337 (HIP), five optimized structures are shown in Figure 3.6. Generally, the geometries are similar to the corresponding 2-proton configurations (S_2L_2H1a-e in Figure 3.2). However, the "open" and "closed" forms (S_2L_3Ha and S_2L_3Hb) have ground spin states $S_{GS} = 7/2$ and $S_{GS} = 1/2$, respectively, i.e. $S_{GS} = 5/2$ is not recovered. However, because the "open" form (S_2L_3Ha) also has a compressed energy ladder with $S_{ES} = 5/2$ and very small $\Delta E_{ES-GS} = 2$ cm^{-1}, the $S = 5/2$ state could easily be the ground state in very similar conformers, perhaps with changes in the hydrogen-bonding network.

3.4.4 Isomers with Neutral His337 (HIE)

We now examine S_2 isomers with neutral His337 (HIE). For 2-proton configurations with His337 (HIE) (Figure 3.7), they are very similar to the corresponding geometries with those in Figure 3.2 and are not further investigated. Note that, with neutral His337, the $N_\epsilon H$ proton does not transfer to O3, therefore starting configurations that differ in the protonation of O3 vs. $N_\epsilon H$ converge into one single equilibrium structure, e.g. S_2L_2H1c_HIE and S_2L_2H1d_HIE converge to the same configuration, labeled as S_2L_2H1c/d_HIE.

For 3-proton isomers with neutral His337 (HIE), which have the same number of atoms and electrons with the isomers in Figure 3.2 and hence can be compared energetically, the optimized geometries and electronic properties are summarized in Figure 3.8. The relative energies are obtained by comparing to S_2L_2H1a. S_2L_3Hc_HIE and S_2L_3Hd_HIE converge to the same configuration, labeled as S_2L_3Hc/d_HIE. This structure has no short Mn-Mn distances and so can be rejected based on EXAFS data.

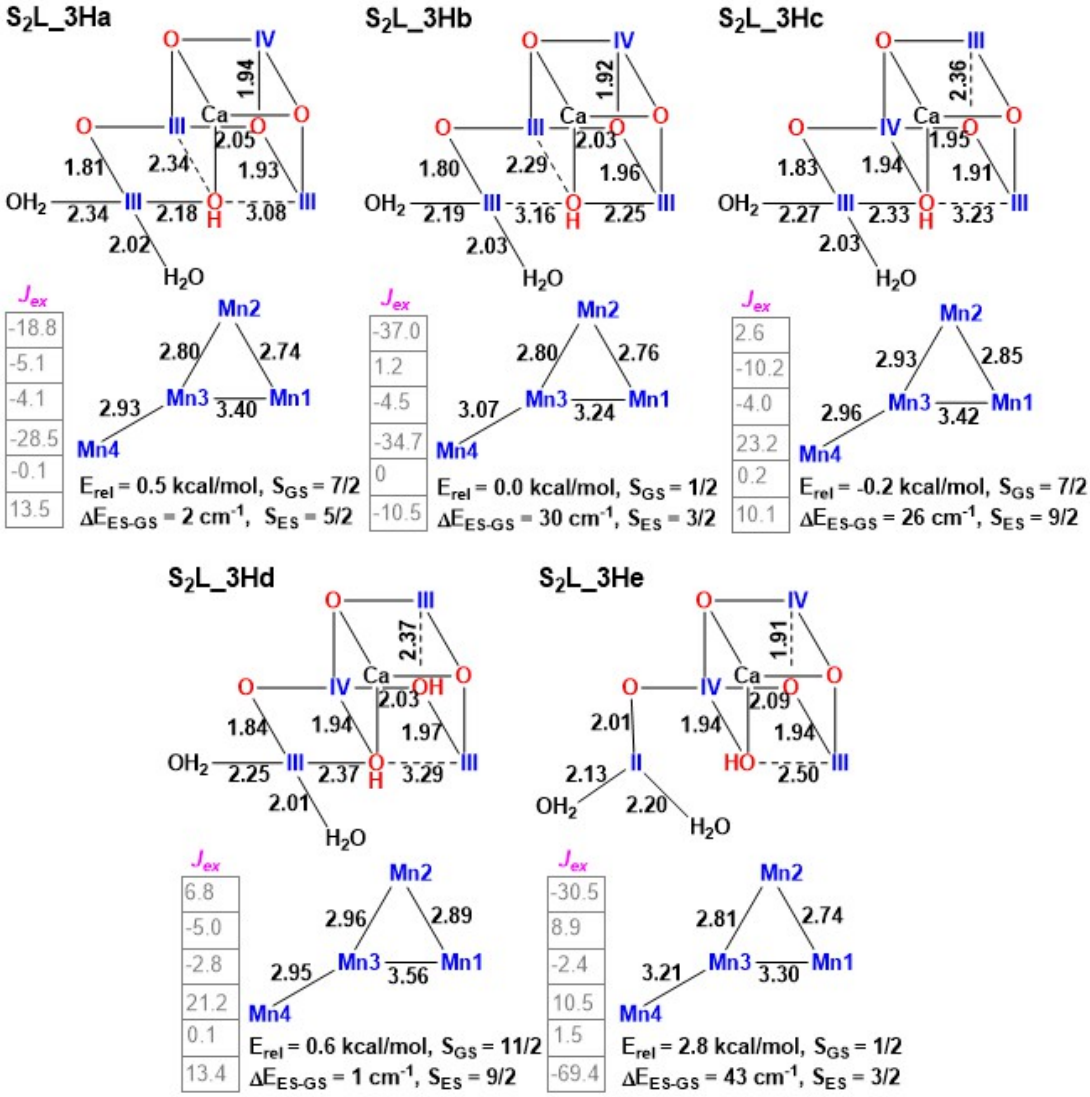

Figure 3.6: Geometries, energetics, and ground spin states of S_2L isomers with protonation state O5 (OH^-), W2 (H_2O) and positive His337 (HIP) for the low oxidation paradigm. The reference energy configuration is S_2L_3Hb.

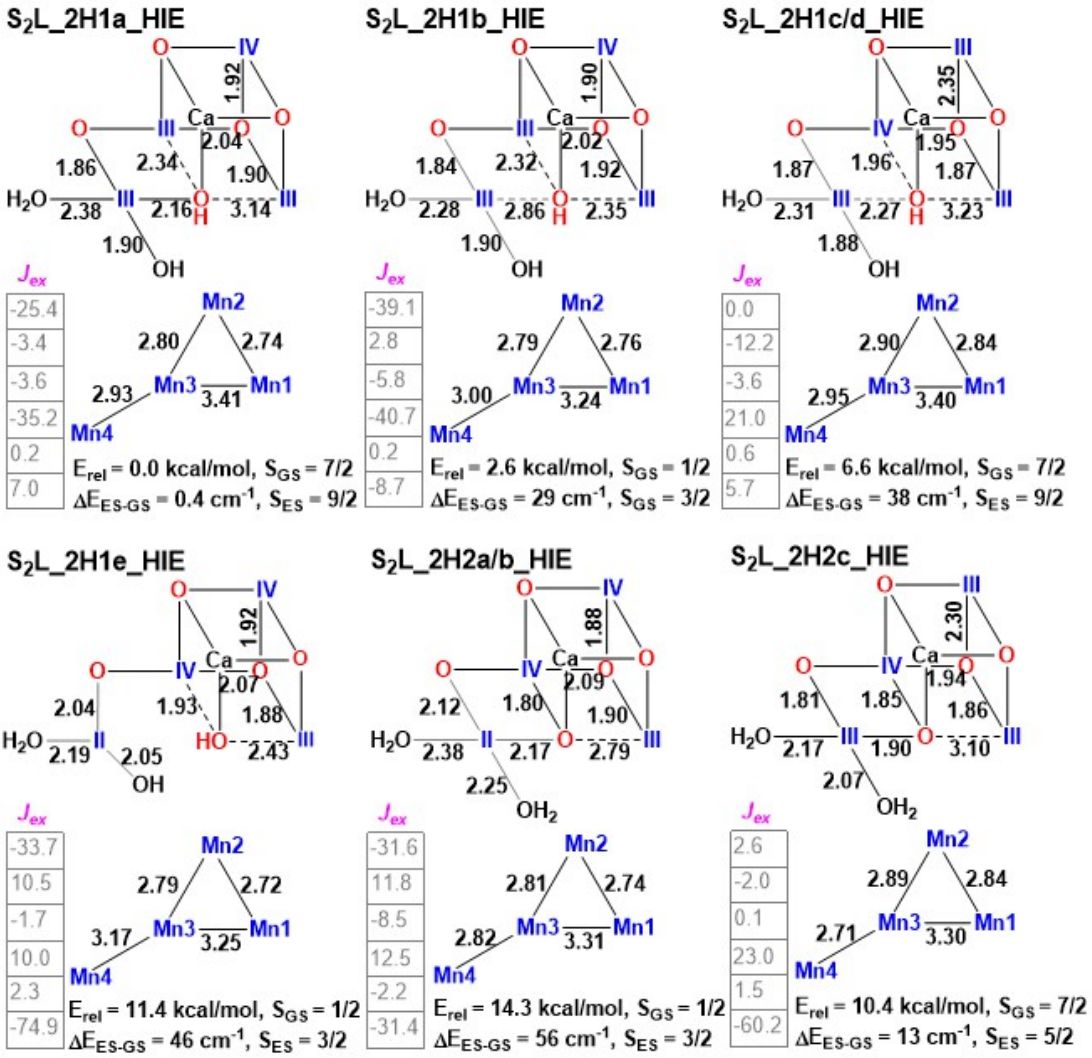

Figure 3.7: Geometries, energetics, and ground spin states of S_2L isomers with two protons distributed on O5 and W2, and neutral His337 (HIE) for the low oxidation paradigm. The reference energy configuration is S_2L_2H1a_HIE.

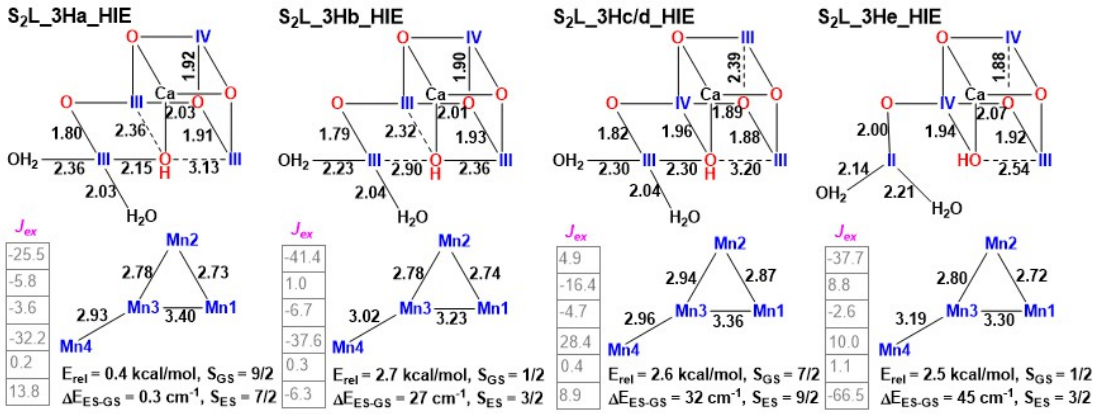

Figure 3.8: Geometries, energetics, and ground spin states of S_2L isomers with protonation state O5 (OH^-), W2 (H_2O) and neutral His337 (HIE) for the low oxidation paradigm. The reference energy configuration is S_2L_2H1a (Figure 3.2).

From Figure 3.8, we see that three other configurations are energetic accessible compared to the 2-proton configurations, including the Mn^{II}-containing S_2L_3He_HIE. S_2L_3Ha_HIE, S_2L_3Hb_HIE, and S_2L_3He_HIE have two short Mn-Mn distances, which agrees with the EXAFS data. The former two can also be assigned as "open" and "closed" forms with $S_{GS} = 9/2$ and $S_{GS} = 1/2$, respectively. However, the $S_{GS} = 5/2$ is not among the low energy states, which leaves unanswered how to account for the $g \approx 4.1$ signal. Similar to arguments given above, one may consider excited configurations of S_2L_3Ha with $S_{ES} = 7/2$ and $\Delta E_{ES-GS} = 0.3$ cm^{-1}, to explain the various $g \geq 4.1$ signals. Changes in the hydrogen-bonding network, i.e. $N_\delta H$ of His337 moves to W2 or O5, may lead to the various EPR spectral forms.

The Mn^{II}-containing configuration, S_2L_3He_HIE, has $S_{GS} = 1/2$ and $S_{ES} = 3/2$ at 45 cm^{-1}. It has a trigonal bipyramidal ligand field around Mn4 (similar to S_2L_2H1e), but with much lower energy. Clearly, H_2O is a much better ligand than OH^- for Mn^{II} and the lower coordination number of 5 provides a relatively weaker ligand field that is favored by the $3d^5$ high-spin electronic configuration of Mn^{II}. We conclude that the LOP structure S_2L_3He_HIE with $S_{GS} = 1/2$ is an energetically completely viable option for the S_2 MLS state. To account for the $g \approx 4.1$ signals as the alternative ground state, one needs to modify the exchange terms to lower either the $S = 3/2$ or

$S = 5/2$ states as new ground states. The HFCs of S_2L_3He_HIE are computed below.

3.4.5 Manganese Hyperfine Coupling Constants

We now compute the magnetic hyperfine coupling constants of Mn ions in S_2 of the OEC under the low paradigm. As pointed out by others[110, 114], the numerically calculated projection coefficients and hyperfine coupling constants depend heavily on the accuracy of the exchange coupling constants. Since we have relatively small J_{ij} (e.g. Figure 3.2, 3.8), the strong exchange limit assumption and neglect of ZFS (with typical values of D_i for Mn^{III} between 1 and 4 cm^{-1}) will lead to unreliable Heisenberg coupling constants[110]. It was reported by Orio *et al.* that for absolute exchange couplings of less than 75 cm^{-1}, neglect of ZFS in the spin projection calculation could introduce significant errors in the computed ^{55}Mn HFCs[87]. Moreover, the true magnetic anisotropies are generally smaller than the scalar (isotropic) values for ^{55}Mn. Therefore, we expect them to be less reliable than the isotropic HFCs. These severe limitations must be kept in mind when considering the reliability of the magnetic HFCs and the significance of the exact values obtained should not be over-rated.

We adopted the approach in which the intrinsic hyperfine constants (the scalar Fermi contact term of the individual ions) are extracted through the BS-DFT calculations as developed by Pantazis *et al.*[114]. It was shown that current density functional method tends to significantly underestimate the ^{55}Mn isotropic hyperfine couplings, which was attributed to the inadequate description of spin polarization[118, 123]. Fortunately, the deviation turns out to be systematic[109, 124] and can be compensated for a universal scaling factor, which was determined to be 1.53 for the TPSSh functional using the CP(PPP) and TZVP basis sets for Mn and remaining atoms, respectively[113]. It should be understood that such a large scaling factor should create skepticism in the absolute values.

Since the $S_{GS} = 5/2$ state is only recovered in S_2L_2H1b, we only examine the related isomers, i.e. 2-proton and 3-proton with His337 (HIE) configurations. The results of configurations with $S_{GS} = 1/2$ are discussed here. The ^{55}Mn hyperfine tensors obtained directly from the BS-DFT calculations are summarized in Table 3.2.

Table 3.2: ^{55}Mn hyperfine tensors (MHz) of different models with $S_{GS} = 1/2$, obtained directly from the lowest broken symmetry calculations (without scaling).

		S_2L_2H1b III,IV,III,III ($\alpha\beta\alpha\beta$)	S_2L_2H1e III,IV,IV,II ($\beta\alpha\beta\alpha$)	S_2L_2H2a III,IV,IV,II ($\beta\alpha\beta\alpha$)	S_2L_3Hb_HIE III,IV,III,III ($\alpha\beta\alpha\beta$)	S_2L_3He_HIE III,IV,IV,II ($\beta\alpha\beta\alpha$)
Mn1	A_{iso}	-489.0	461.6	395.8	-481.9	444.4
	A'_x	212.7	-207.9	-204.6	207.1	-206.8
	A'_y	-74.3	54.2	72.1	-58.9	57.8
	A'_z	-138.5	153.7	132.5	-148.2	148.9
Mn2	A_{iso}	475.6	-480.5	-478.7	482.6	-480.9
	A'_x	-20.7	14.2	15.0	-21.6	15.6
	A'_y	1.0	5.4	4.6	4.6	2.9
	A'_z	19.7	-19.7	-19.6	17.0	-18.5
Mn3	A_{iso}	-496.5	436.9	440.4	-528.6	446.7
	A'_x	218.8	-45.6	-39.6	218.7	-38.9
	A'_y	-94.7	-1.6	7.3	-81.0	-5.4
	A'_z	-124.1	47.2	32.3	-137.8	44.3
Mn4	A_{iso}	406.3	-786.0	-864.6	393.7	-771.6
	A'_x	-205.3	15.1	8.3	-217.0	11.5
	A'_y	61.2	5.6	-2.8	62.8	-0.3
	A'_z	144.2	-20.7	-5.5	154.2	-11.1

The scaled values of the calculated intrinsic site isotropic hyperfine coupling constants, which agrees with the experimental data qualitatively[32, 108]), and the corresponding spin projection coefficients for configurations with $S_{GS} = 1/2$ are shown in Table 3.3.

The calculated isotropic hyperfine couplings of Mn ions in the coupled cluster for models with ground spin state $S = 1/2$ are shown in Table 3.4. The isotropic cluster HFCs are in descending order of the absolute values. Note that, although the signs are shown here, neither sign information nor any assignment of the HFCs to specific manganese centers can be derived from published experiments. Four different sets of experimental HFCs from cyanobacteria (3) and spinach (1) PSIIs that were obtained in different simulations of the EPR and ENDOR spectra are also shown[3, 4, 5, 6]. The experiments on spinach PSII by Jin *et al.* were performed at 2.5 K, where relaxation effects that may hinder observation of the Mn ENDOR resonances at higher temperatures are suppressed. The differences among them reflect not only the different way in which the simulations were performed, but also aspects of sample preparation. Thus these data were regarded as a range to compare with.

Table 3.3: Scaled values of the calculated intrinsic isotropic hyperfine coupling constants (MHz) and the corresponding spin projection coefficients of individual Mn ions for electronic configurations with $S_{GS} = 1/2$.

	S_2L_2H1b	S_2L_2H1e	S_2L_2H2a	S_2L_3Hb_HIE	S_2L_3He_HIE
Mn1	-187	-176	-151	-184	-170
Mn2	-243	-245	-244	-246	-245
Mn3	-190	-223	-225	-202	-228
Mn4	-155	-240	-265	-150	-236
p_1	1.758	-1.016	-1.332	1.644	-0.938
p_2	-0.996	0.726	1.380	-1.000	0.628
p_3	1.562	-0.978	-0.734	1.688	-0.986
p_4	-1.324	2.268	1.684	-1.334	2.296

Table 3.4: Calculated isotropic HFCs of ^{55}Mn ions in the coupled cluster for different configurations with $S_{GS} = 1/2$ and the experimental cluster HFCs from different EPR/ENDOR simulations (MHz)[3, 4, 5, 6].

	^{55}Mn A_{iso}			
S_2L_2H1b	-328 (Mn1)	-296 (Mn3)	242 (Mn2)	206 (Mn4)
S_2L_2H1e	-544 (Mn4)	218 (Mn3)	179 (Mn1)	-178 (Mn2)
S_2L_2H2a	-445 (Mn4)	-337 (Mn2)	202 (Mn1)	165 (Mn3)
S_2L_3Hb_HIE	-341 (Mn3)	-303 (Mn1)	246 (Mn2)	200 (Mn4)
S_2L_3He_HIE	-542 (Mn4)	225 (Mn3)	159 (Mn1)	-154 (Mn2)
Exp. S_2[3]	297	245	217	200
Exp. S_2[5]	295	245	205	193
Exp. S_2[4]	329	257	243	186
Exp. S_2[6]	514	233	45	7

From Table 3.4, ^{55}Mn HFCs for S_2L_2H1b and S_2L_3Hb_HIE agree better with the earlier experimental pattern[3, 4, 5]. Using HIE instead of HIP as His337 changes the HFCs marginally. Two of the geometries, S_2L_2H1e and S_2L_3He_HIE, reproduce the unusually large HFC of Mn4 and the intermediate HFC of Mn3, reported by Jin *et al.*[6]. However, no configurations produce the complete pattern similar to that obtained from experiments by Jin *et al.*[6], in which there is one unusually large HFC, one medium size, one small size and one very small size. Moreover, the experiments by Jin *et al.*[6] also revealed that at least two and probably three Mn hyperfine couplings exhibit very large anisotropies, which they attributed to the existence of two or more Mn^{III}. However, their proposed HFC anisotropies (240(47), 180(77), 50(110), na; MHz (%) (obtained from the length of the arrows which they used in their figure showing the frequency range for each Mn atom)) are huge in comparison with the corresponding isotropic HFCs and therefore far beyond any reasonable magnetic dipolar anisotropy from individual ^{55}Mn tensors ($< 30\%$)[108]. Their assignment of anisotropies, if correct, confirms our foregoing caution about neglecting ZFS and small J_{ij}'s when interpreting the HFC anisotropies. All prior DFT calculations have assumed the strong exchange limit neglecting ZFS. Calculations of our selected electronic configurations, also ignoring ZFS while including solely magnetic dipolar anisotropy indeed show that Mn^{III} has HFC anisotropy typical of an isolated Mn^{III} (Table 3.2). Similarly, as expected,Mn^{II}-containing configurations show a large isotropic and small anisotropic component (S_2L_2H1e, S_2L_2H2a, and S_2L_3He_HIE in Table 3.2). One natural question to ask is whether Mn^{II} might be present in S_2 state under the low paradigm. A second question to ask is what is the contribution to HFC anisotropy arising from ZFS in the weak-intermediate exchange coupling.

Examples of dimanganese complexes illustrate the severity of this problem[108]. Although the strong exchange condition ($D_i/J_{ik} \ll 1$) occurs for many di-μ-oxo-bridged Mn_2(III,IV) complexes, Mn_2(II,III) complexes exhibit intermediate ($D_i/J_{ik} < 1$) or even weak coupling. Three examples of Mn_2(II,III) complexes including Manganese Catalase have $D/J \sim 0.5$ and the resulting ZFS contribution to the hyperfine anisotropy of Mn^{II} is 38-50% larger than the magnetic dipolar term[108].

Table 3.5: ^{55}Mn hyperfine tensors (MHz) of $[Mn_2(bpmp)\text{-}(\mu\text{-}OAc)_2]^{2+}$, obtained directly from the broken symmetry calculation.

	Mn1				Mn2			
III,II	A_{iso}	A'_x	A'_y	A'_z	A_{iso}	A'_x	A'_y	A'_z
$(\beta\alpha)$	522.3	-223.2	60.0	163.2	-772.1	6.1	1.9	-8.0

To examine this, we performed DFT calculations, described in Section 3.3.2, on an Mn_2(II/III) model compound $[Mn_2(bpmp)\text{-}(\mu\text{-}OAc)_2]^{2+}$[125], where the Mn^{II} is known to have unusually large HFC anisotropy[108]. The optimized structure is shown in Figure 3.9. In contrast to the experiments[108], our calculations in the strong exchange limit, e.g. ignoring ZFS, reveal the expected small anisotropies of an isolated Mn^{II}, with largest anisotropy about 1% of the isotropic HFC (Table 3.5). This implies that neglecting the consequences of ZFS and small J_{ij}'s cannot reproduce the large anisotropy of Mn^{II} in this Mn_2(II, III) model compound. Hence, we conclude it is possible that the S_2 state under the low paradigm which contains Mn^{II}, should indeed produce high HFC anisotropy arising form transferred ZFS. Unfortunately, this non-magnetic contribution cannot be calculated using current DFT methods. In this way, part of the results reported by Jin *et al.*[6] can be explained, i.e. Mn^{II} is correctly assigned based on the largest ^{55}Mn scalar HFC term, while Mn^{II} and Mn^{III} produce unusually large anisotropies owing to transferred ZFS. However, we still cannot reproduce the two smallest HFCs they report. One explanation that may account for the discrepancies between the 2.5 K and > 5 K ENDOR data is that at 2.5 K the relatively isotropic Mn^{IV} tensor will exhibit very slow nuclear spin relaxation compared to the highly anisotropic Mn^{II} and Mn^{III} tensors. Thus, while Mn^{II} tensors would be ENDOR-invisible at > 5 K due to fast nuclear relaxation, the Mn^{IV} tensor could be ENDOR-invisible at 2.5 K and below, due to slow relaxation.

3.5 Conclusions

We have studied several structural configurations for the S_2 state in the low paradigm. The interconversion between MLS and $g \approx 4.1$ signals can be realized with low barrier between two configurations ("open" and "closed" forms), which mainly differs at the

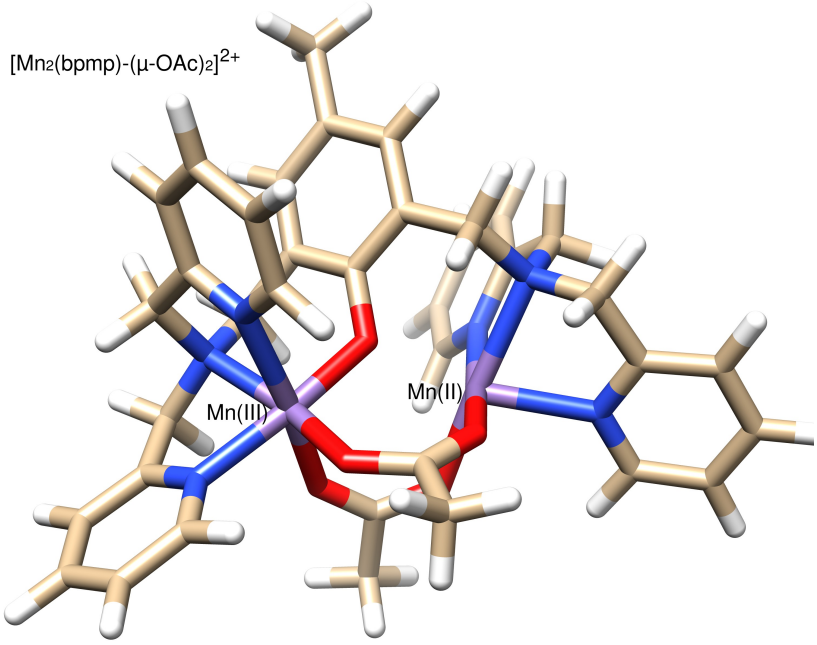

Figure 3.9: Optimized structure of model compound $[Mn_2(bpmp)\text{-}(\mu\text{-}OAc)_2]^{2+}$.

Table 3.6: Calculated spin Hamiltonian parameters for high-paradigm S_2 structures ("open/MLS" vs. "closed/$g \approx 4.1$") with O5 (O^{2-}), W2 (OH^-), and His337 (HIP). Unit for ΔE_{ES-GS} is cm^{-1}.

	J_{12}	J_{13}	J_{14}	J_{23}	J_{24}	J_{34}	S_{GS}	S_{ES}	ΔE_{ES-GS}
MLS	-19.2	0.5	0.4	15.9	2.2	-16.1	1/2	3/2	30
$g \approx 4.1$	24.1	11.0	4.0	25.5	1.6	-24.2	5/2	7/2	24

position of O5 (OH^-). Interestingly, the "open" form corresponds to $S_{GS} = 5/2$ and the "closed" form corresponds to $S_{GS} = 1/2$, which is the opposite of what is found in high paradigm models proposed by Pantazis *et al.*[47] (also confirmed by us, see Table 3.6). This distinction should not be viewed as a disagreement. Indeed, it is not unexpected since the inversion of relative energies of states is determined by the relative exchange energies and these are quite different for the LOP vs. HOP cases.

Two interconvertible Mn^{II}-containing configurations with positive His337 (HIP), "open" and "closed" forms, can also reproduce the $S_{GS} = 1/2$ and $S_{GS} = 5/2$, the same order compared to the high paradigm models[47]. But these two configurations have high energies, compared to low-paradigm models that contain only Mn^{III} and Mn^{IV}. The protonation and oxidation states of the cluster, together with the position of the bridging oxygen (O5), determine the exchange coupling constants, which in turn

establish the electronic properties of the OEC. This strong dependence on geometry and oxidation states gives the OEC high flexibility in terms of ground spin state, which is why we see the "open" form has $S_{GS} = 5/2$ in one configuration, while it is $S_{GS} = 1/2$ in another, e.g. S_2L_2H1a vs. S_2L_2H2a. These structures have either two or three short Mn-Mn distances, consistent with EXAFS data.

Moreover, we find that small perturbations, such as rearrangement of hydrogen-bonding network or position of O5, can produce energy accessible isomers with $S_{GS} = 1/2$ and $S_{GS} = 5/2$, corresponding to $g = 2.0$ and $g \approx 4.1$ EPR signals, but also provide with isomers with $S_{GS} = 7/2$, $9/2$ or $11/2$, which may be accounted for the $g = 10$ and 6 EPR signals. Hence, low paradigm models can easily explain the experimental observation that the EPR signals of PSII vary depending on the preparation conditions.

As for the hyperfine coupling tensors, there are two major classes of fits to experimental data. Earlier EPR experiments were fit to spin Hamiltonians with one large and three similar smaller isotropic HFCs[3, 4, 5]; more recently, Jin *et al.*[6] reported one very large, one medium, two very small hyperfine coupling constants, the first three with large anisotropies. We computed the ^{55}Mn HFCs of S_2 models under the low paradigm by calculating the spin-projection coefficients through diagonalization of the HVvD Hamiltonian matrix, which is constructed from the exchange coupling constants. The LOP configuration with three Mn^{III} and one Mn^{IV}, S_2L_2H1b, agrees reasonable well with earlier EPR and ENDOR interpretations using the HOP, than with those of Ref.[6]. By contrast, the Mn^{II}-containing LOP configurations, S_2L_2H1e and S_2L_3He_HIE, reproduce the unusually large HFC of Mn4 and the intermediate HFC of Mn3, reported by Jin *et al.*[6]. Hence, we conclude that the LOP is the preferred option as it accounts for more of the various HFC data than the HOP.

In conclusion, the low paradigm S_2 configurations can match all the EXAFS data and earlier EPR and ENDOR spectra (and some of the more recent HFC data from Jin *et al.*[6]). These calculations illuminate the debate between the low and high oxidation state paradigms, giving new physical insights into the origin of the HFCs and their anisotropies. Knowledge of the electron and proton count is indispensable to reaching a mechanism of the oxygen evolving complex in Photosystem II and artificial catalysts

which aim to mimic it.

Chapter 4

Higher S States and O–O Bond Formation Mechanism

4.1 Overview

The dioxygen is produced in the transition $S_3 \rightarrow (S_4) \rightarrow S_0$. Hence, the study of the S_3 and S_4 states is crucial in understanding the O–O bond formation mechanism.

Although the XRD structure of the S_3 state has been revealed, it is vigorously debated and there is little agreement on the coordination numbers of the four Mn ions, or the number of substrate water molecules bound to the OEC before the S_3 state[126, 2]. On one hand, Young *et al.* reported a S_3 structure at 2.25 Å resolution[127]. Overall, this structure is very similar to the 1.95 XFEL S_1 structure[58]. The key distances are summarized in Table 4.1. Importantly, this S_3 structure does not support models in which a new water or hydroxo binds to Mn1, as no corresponding electron density or distance changes were observed. For that reason, the popular O–O bond formation mechanism[80, 7], where radical coupling occurs between O5 and a terminal oxyl-radical from a non-crystallographic water, which first bind to Mn1 as terminal hydroxo ligand during the $S_2 \rightarrow S_3$ transition, is disqualified.

On the other hand, Suga *et al.* reported a S_3 structure at 2.35 Å resolution[11]. Unlike the 2F study of Young *et al.*, Suga *et al.* reported that there was an apparent positive peak around O5, hence suggesting the insertion of a new oxygen atom (O6) close to O5, providing an O–O bond distance of 1.5 Å between these two oxygen atoms (Figure 4.1). Note that, 1.5 Å is very close to the bond length of an peroxide. This result, however, seems to conflict with the kinetics of substrate exchange experiments[128, 129, 130, 131, 132, 133] (Table 1.2), where a "fast" and a "slow" rate are observed in S_3[132, 134]. Petrie *et al.* suggested that the 2.35 Å XRD S_3 structure may have some form of S_4, where O–O bonding has been initiated[135], while the 2.25

Table 4.1: Key distances (Å) for 1.95 Å XFEL S_1 and 2.25 Å XRD S_3 structures.

Parameter	1.95 Å S_1 XFEL	2.25 Å S_3 XRD
Mn1-Mn2	2.70	2.73
Mn2-Mn3	2.71	2.71
Mn1-Mn3	3.25	3.24
Mn3-Mn4	2.87	2.74
Mn1-Mn4	4.92	4.92
Ca-Mn1	3.50	3.45
Ca-Mn2	3.34	3.37
Ca-Mn3	3.44	3.44
Ca-Mn4	3.74	3.87
O5-Mn1	2.70	2.70
O5-Mn3	2.26	2.14
O5-Mn4	2.35	2.32

Å XRD S_3 structure represents the true physiological form.

As for the high and low paradigms debate, the 2.25 Å S_3 XRD structure does not favor most of the high paradigm models, in which O5 is models as an oxide and most of these models require binding of an additional water or hydroxo to either Mn1 or Mn4 in S_3[7, 136, 137]. It is not likely to reproduce the Mn3-O5 distance with O5 in the form of O^{2-}. Petrie *et al.* showed a model with O5 (OH^-) under the low paradigm can match the 2.25 Å S_3 XRD structure fairly well with oxidation state distribution (III, IV, IV, III)[135].

The S_4 state is an intermediate formed transiently of O_2 formation in the $S_3 \rightarrow S_0$ transition. Researchers have used X-ray technique, which can monitor redox and local structural changes in metal clusters[60], to investigate this transition. A deprotonation process was identified and subsequent electron transfer to $Y_z^\bullet$ would give an additional S_4' state, thus extending the fundamental S-state cycle[138]. However, this crucial transition ($S_3 \rightarrow S_0$) is still poorly understood because of lack of evidence for the elusive S_4 state.

In this chapter, we examine different S_3 configurations with various protonation and oxidation states under the low paradigm. S_4 and subsequent O–O bond formation mechanism are then investigated, with an aim to find a pathway with sufficient low barrier towards peroxide formation. Selected high paradigm results are also provided.

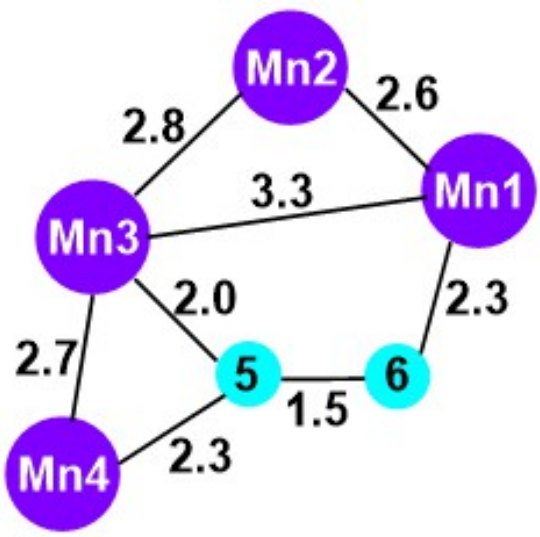

Figure 4.1: Position of the newly inserted oxygen atom O6 relative to its nearby atoms in the 2.35 Åstructure (reconstructed from Ref.[11]).

4.2 Methodology

Computational models and details are originated from Section 2.2.

4.3 Results and Discussion

4.3.1 S_3 State

The transition $S_2 \rightarrow S_3$ is suggested to be accompanied by the loss of proton[139], and most likely also by binding of an additional water molecule[126, 140]. This water molecule can be introduced as either H_2O or OH^-. As a result, various S_3 configurations are obtained based on whether or where to insert the additional water ligand. Two criterions are used for S_3 state models. One is the EXAFS data, which, under current interpretations, requiring the OEC to contain three short Mn-Mn distances[21, 59] (Table 1.1). The other criterion is based on earlier CW-EPR measurements[40, 7], which suggest that the S_3 state has a ground spin state of three ($S_{GS} = 3$) as mentioned earlier in Section 1.2.2.

Without Additional Water

We first examine configurations without additional water ligand. W2 is treated as either H_2O or OH^-. O5 can be one of H_2O, OH^-, and O^{2-}. The protonation state of His337 can be either HIP or HIE. The nomenclature refers to the S_i state, and the total number of protons distributed on O5 and W2. Optimized structures of selected configurations are shown in Figure 4.2. In general, these structures have Mn1(III), which orients the empty d orbital towards O5, resulting in long Mn1-O5 distance and an "open" Mn_3CaO_4 cube.

Two oxidation state patterns are revealed: III-IV-IV-III and III-IV-III-IV. The latter appears in configurations with O5 (H_2O), i.e. S_3L_3Hb and S_3L_3Hb_HIE, in which Mn-O5 distances are very large and Mn1(III), Mn3(III) and Mn4(IV) are pentacoordinate. One proton on W1 transfers to D1-Asp61 because of the repulsion of Mn4(IV). Note that, the J couplings of S_3L_3Hb and S_3L_3Hb_HIE are very similar, yet they have different ground spin states, $S_{GS} = 0$ and $S_{GS} = 3$ respectively, which implies the electronic properties of the OEC is sensitive to the exchange coupling parameters as already mentioned in Chapter 3. These two configurations have much higher energy and long Mn3-Mn4 distance (> 3.2 Å), hence are not further considered.

Configurations with O5 (O^{2-}) have three short Mn-Mn distances (≤ 2.8 Å). All of them (S_3L_1H, S_3L_2Ha, and S_3L_2Ha_HIE) show ground state $S_{GS} = 0$. Two configurations with O5 (OH^-) have $S_{GS} = 3$, i.e. S_3L_3Ha and S_3L_3Ha_HIE, and are included in the HFCs calculations later. However, these two only produce two short Mn-Mn distances with Mn3-Mn4 around 2.95 Å, hence are not ideal S_3L candidates.

Additional Water on Mn1

The additional water ligand (O6: H_2O or OH^-) can be introduced as a ligand to either Mn1 or Mn4. We first investigate the case with the additional water on Mn1. The optimized structures of selected S_3L isomers are shown in Figure 4.3. The nomenclature refers to the S_i state, the total number of protons distributed on O5, W2, and

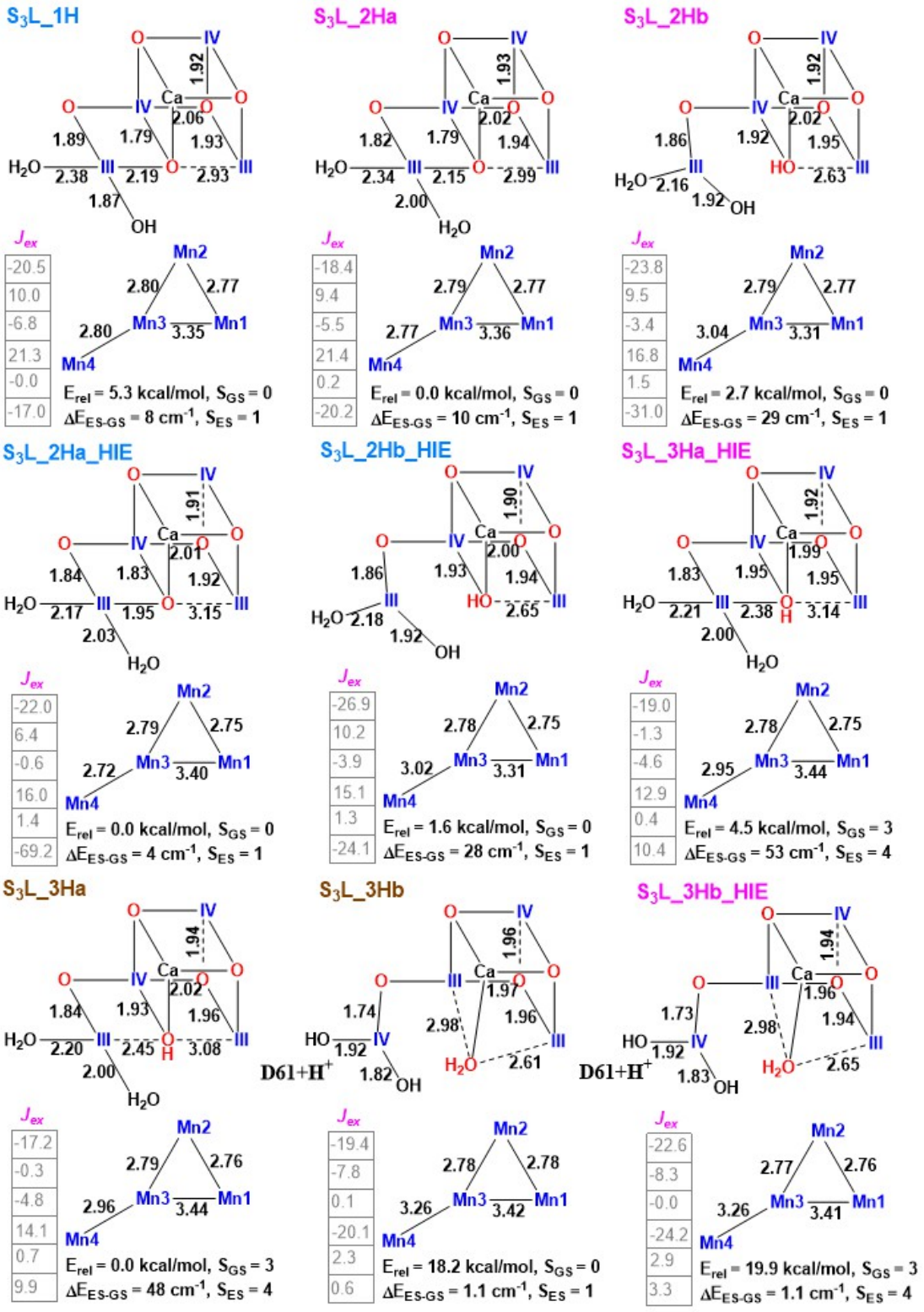

Figure 4.2: Geometries, energetic, and spectroscopic properties of S_3L isomers without additional water ligand in the low oxidation paradigm. The configurations with the same color of titles have the same numbers of electrons and atoms, and are grouped together to compare the relative energetics.

O6, and whether the additional water is on the right (Mn1) or left (Mn4). For example, S_3L_rw3Ha indicates a S_3 configuration under the low paradigm with 3 protons distributed on O5, W2, and O6, and O6 is bound to Mn1.

All structures in Figure 4.3 have oxidation state (III-IV-IV-III), short Mn3-Mn4 and reasonable short Mn2-Mn3 distances. The length of Mn1-Mn2 depends on the direction of the Jahn-Teller axis of Mn1(III). These configurations can be classified into two "classes" accordingly. In the first class, Mn1(III) orients its empty d orbital towards O3, resulting relatively longer Mn1-O3 and Mn1-Mn2 distances and ground state $S_{GS} = 3$. On the other hand, Jahn-Teller axis of Mn1 in the second class, S_3L_rw3Hc, S_3L_rw4H, and S_3L_rw4H_HIE, orients towards the additionally introduced water ligand (O6 (H_2O)) on Mn1, resulting in long Mn1-O6 and short Mn1-Mn2 distances and ground state $S_{GS} = 1$. As a consequence, three short Mn-Mn distances are obtained, which is consistent with the EXAFS data[21, 59]. S_3L_rw3Hc belongs to the second class and has the lowest energy among the corresponding isomers. However, the ground state $S_{GS} = 1$ does not agree with the EPR experiments[40, 7].

The reason we have different ground spin states for these two "classes", differing in Jahn-Teller direction of Mn1(III), is that the sign of the exchange coupling of Mn_2(III,IV) sub-unit (Mn1 and Mn2) flips when the direction of Jahn-Teller effect of Mn1(III) changes from towards O3 to O6. It implies that the Jahn-Teller direction of Mn^{III} not only determines the geometries (i.e. Mn-Mn distances) but also can change the electronic properties (J couplings) of the OEC significantly. Another factor that can affect the exchange couplings is the protonation state of the bridging oxygen. For example, S_3L_rw3Ha and S_3L_rw3Hb differ in the protonation state of O3; in the latter configuration, the N_ϵH of His337 moves to O3, resulting in O3 (OH^-). Meanwhile, J_{13} shrinks from -8.9 to 0.0 cm^{-1}.

It is also interesting to notice that the carboxylate of D1-Asp170, an adjacent bidentate ligand bridging between Mn4 and Ca in the S_1 XRD structure, rearranges to bidentate (W1 (H_2O), Ca) in some of the structures, e.g. S_3L_rw3Ha, leaving Mn4 pentacoordinate with a square pyramidal ligand field. As mentioned in Section 2.4, this is mechanistically significant, as it suggests a potential functional role for the two

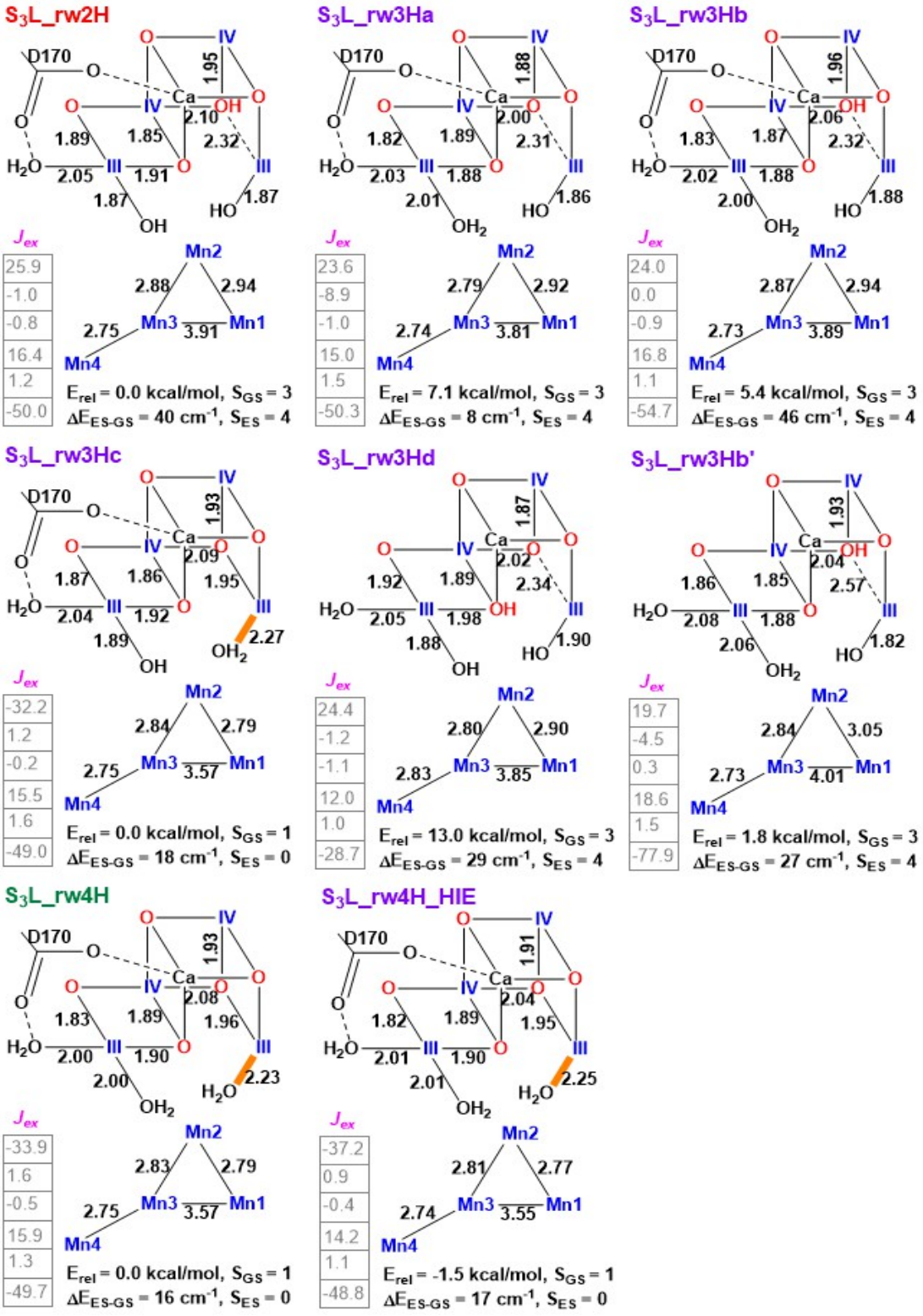

Figure 4.3: S_3L isomers with additional water ligand on Mn1 in the low oxidation paradigm. The orange bond indicates the direction of Jahn-Teller axis of Mn1.

carboxylate ligands to Mn4 in substrate water deprotonation. In this case, W1 and W2 may form a pair of geminal hydroxo-carboxylato on Mn4(W1)(W2), possibly involving D1-Asp61 that accepts and shuttles away protons from W1 or W2.

Additional Water on Mn4

With the additional water ligand on Mn4, several S_3L isomers with oxidation state (III-IV-IV-III) are obtained, shown in Figure 4.4. Compared with the corresponding isomers with addtional water ligand on Mn1 (Figure 4.3), these configurations tend to have higher energies, e.g. S_3L_rw4H vs. S_3L_lw4H. All configurations have short Mn2(IV)-Mn3(IV) distance. The additional water ligand on Mn4 always forms a hydrogen bond with O5. As a result, Mn4 is bridged with the Mn_3Ca cube only through O4 and both Mn4-O5 and Mn3-Mn4 become much longer, with $d_{\text{Mn3-Mn4}} > 3$ Å, which is not consistent with the EXAFS data[21, 59]. Moreover, the only configuration with $S_{GS} = 3$ (S_3L_lw2Ha) has relatively larger energy than others.

One interesting structure is S_3L_lw2Hb. The additional water ligand (OH^-) replaces D1-Asp170 and becomes a ligand to Ca and Mn4, while D1-Asp170 is bidentate to Ca and W1 (H_2O), forming a hydrogen bond interaction with W1. Again, this could be mechanistically significant, since it suggests a possible pathway to introduce an additional substrate water, i.e. by replacing D1-Asp170 and bounding to Mn4.

By no means we have sampled enough possible configurations and not all possible Jahn-Teller directions if Mn^{III} have been considered, but current S_3L models can not match the EXAFS data, requiring three short Mn-Mn distances, and EPR experiments, requiring $S_{GS} = 3$, at the same time.

^{55}Mn Hyperfine Coupling Constants

The scaled values of the calculated intrinsic site isotropic hyperfine coupling constants and the corresponding spin projection coefficients for S_3L configurations with $S_{GS} = 3$ are shown in Table 4.2. The calculated isotropic hyperfine couplings of ^{55}Mn ions in the coupled cluster are summarized in Table 4.3. Note that all the configurations considered here have oxidation state (III-IV-IV-III).

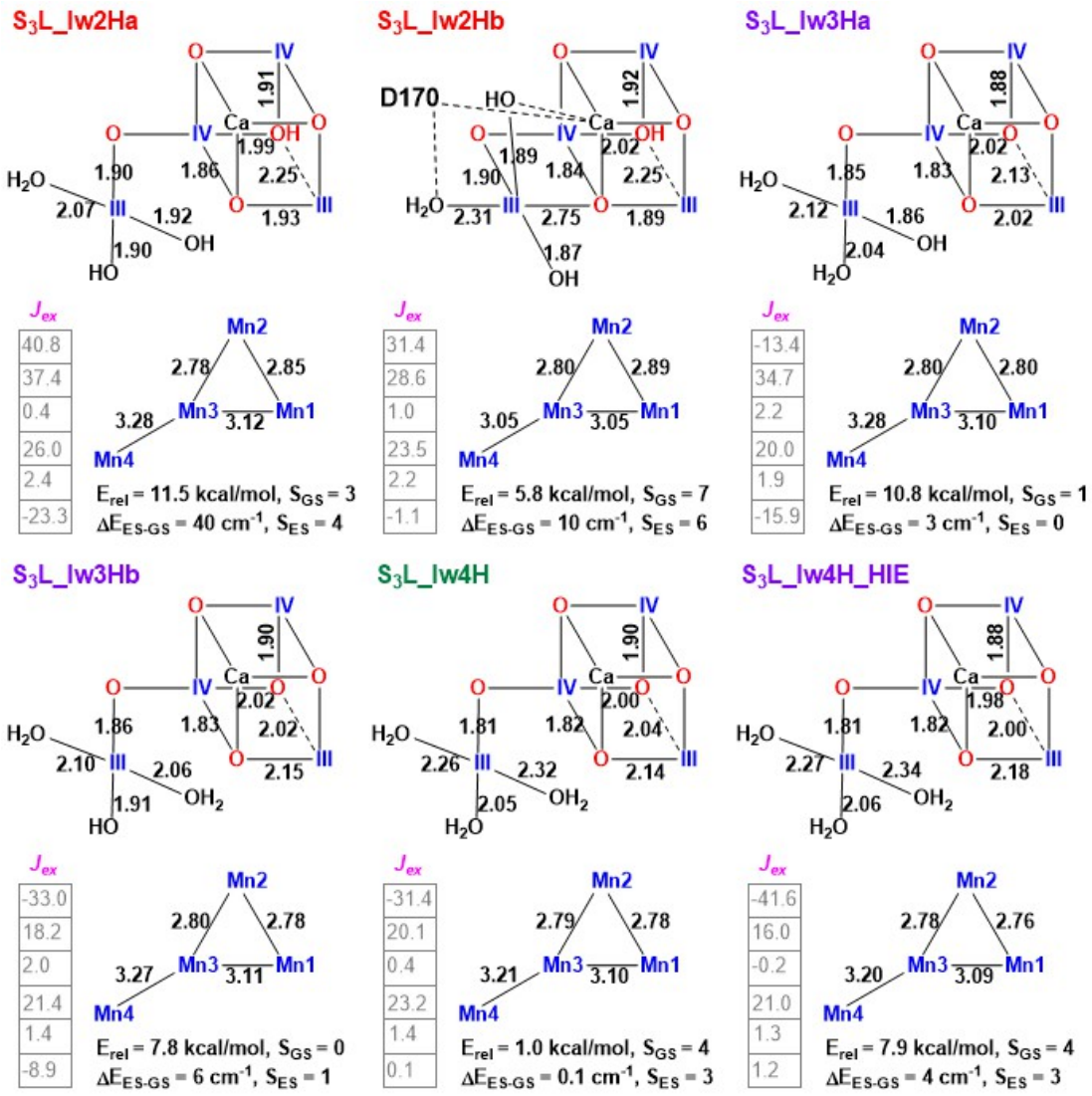

Figure 4.4: S_3L isomers with additional water ligand on Mn4 in the low oxidation paradigm. The reference energies are in Figure 4.3 with the same color.

Table 4.2: Scaled values of the calculated intrinsic isotropic hyperfine coupling constants (MHz) and the corresponding spin projection coefficients of individual Mn ions for S_3L electronic configurations with $S_{GS} = 3$.

	Mn1	Mn2	Mn3	Mn4	p_1	p_2	p_3	p_4
S_3L_3Ha	-161	-214	-196	-176	-0.476	0.387	0.470	0.619
S_3L_3Ha_HIE	-164	-213	-194	-188	-0.471	0.378	0.468	0.625
S_3L_rw2H	-186	-198	-202	-183	0.647	0.470	0.252	-0.369
S_3L_rw3Ha	-184	-184	-205	-178	0.657	0.459	0.132	-0.248
S_3L_rw3Hb	-186	-196	-212	-178	0.647	0.470	0.257	-0.374
S_3L_rw3Hd	-165	-187	-197	-238	0.643	0.472	0.276	-0.391
S_3L_rw3Hb'	-150	-195	-209	-237	0.658	0.456	0.179	-0.293
S_3L_lw2Ha	-195	-192	-182	-172	0.879	0.677	0.643	-0.198

Table 4.3: Calculated isotropic HFCs of ^{55}Mn ions in the coupled cluster for different S_3L configurations with $S_{GS} = 3$ and experimental values for the S_3 state[7], ordered high to low in terms of absolute values. Assignments to Mn ions are in indicated in parentheses. Positive sign for the HFC identifies the Mn ion with β spin.

	^{55}Mn A_{iso}			
S_3L_3Ha	-108 (Mn4)	-92 (Mn3)	-82 (Mn2)	76 (Mn1)
S_3L_3Ha_HIE	-117 (Mn4)	-90 (Mn3)	-80 (Mn2)	77 (Mn1)
S_3L_rw2H	-120 (Mn1)	-93 (Mn2)	67 (Mn4)	-50 (Mn3)
S_3L_rw3Ha	-120 (Mn1)	-85 (Mn2)	44 (Mn4)	-27 (Mn3)
S_3L_rw3Hb	-120 (Mn1)	-92 (Mn2)	66 (Mn4)	-54 (Mn3)
S_3L_rw3Hd	-106 (Mn1)	93 (Mn4)	-88 (Mn2)	-54 (Mn3)
S_3L_rw3Hb'	-98 (Mn1)	-88 (Mn2)	69 (Mn4)	-37 (Mn3)
S_3L_lw2Ha	-171 (Mn1)	-129 (Mn2)	-117 (Mn3)	34 (Mn4)
Exp. (Ref.[7])	-99.0 ($\frac{\text{Mn1}}{\text{Mn2}}$)	-95.6 ($\frac{\text{Mn1}}{\text{Mn2}}$)	-25.9 ($\frac{\text{Mn3}}{\text{Mn4}}$)	≤ 5 ($\frac{\text{Mn3}}{\text{Mn4}}$)

Experimentally, the ^{55}Mn hyperfine coupling constants of S_3 have been observed to fall into two classes (in terms of absolute magnitude): a large coupling class with $|A| \approx 100$ MHz displaying negative ^{55}Mn HFCs and a small coupling class with $|A| < 30$ MHz assigned as either positive or negative[7]. Configurations without additional water (S_3L_3Ha, S_3L_3Ha_HIE) and S_3L_lw2Ha are ruled out as S_3 candidates, since they do not reproduce two classes of isotropic HFCs. Configurations with additional water on Mn1 match the experiments better, except for S_3L_rw3Hd. The closest match is S_3L_rw3Ha, which has two short Mn-Mn distance (< 2.8 Å) and one slightly longer Mn1-Mn2 (2.92 Å). The second closest is S_3L_rw3Hb'.

We find that S_3L_rw3Ha can convert to S_3L_rw3Hc if the Jahn-Teller axis of Mn1(III) orients towards the additional water O6. Hence, one may argue that the S_3 state consists of at least two conformers, i.e. S_3L_rw3Ha and S_3L_rw3Hc, with the former matches the EPR ($S_{GS} = 3$) and HFCs requirements while the latter ($S_{GS} = 1$) produces three short Mn-Mn distances which is consistent with the EXAFS data. However, Cox *et al.*[7] claims the ^{55}Mn HFCs of S_3 are isotropic, suggesting octahedrally coordinated Mn^{IV} ions. The low-paradigm models do not match those experiments because of the existence of Mn^{III} ions.

4.3.2 S_4 State and O–O Bond Formation Mechanism

We investigate various S_4L configurations and proceed towards O–O bond formation. The goal is to find a reaction pathway with sufficiently low energy barrier under the low paradigm. Positive His337 (HIP) is assumed.

Without Additional Water

Three configurations are obtained without the additional water (Figure 4.5). S_4L_closed is in the "closed" form, in which O5 is close to Mn1, leaving Mn4 pentacoordinate. The other two configurations are in the "open" form, and one of them have one more proton on W2. Peroxide formation occurs between W2 and O5. The energy profiles are obtained by relaxed scan along the two substrate oxygens under two spin states: $S = 13/2$ and $S = 15/2$, corresponding to the high spin states of the reactant and product, respectively. Based on the Mulliken spin populations on the two substrate oxygens, oxyl-radicals are obtained with $S = 15/2$. The initial configuration with $S = 15/2$ will have much higher energy, but the corresponding energy barrier is much lower. The transition state can be estimated by the intersection point of the two relaxed scans with $S = 13/2$ and $S = 15/2$. None of them has sufficiently low energy barrier towards peroxide formation.

With Additional Water

One-proton configurations. With an additional water (O6) introduced, three S_4L configurations with one proton distributed among W2, O5, and O6 are obtained (Figure 4.6). The configuration with the lowest energy, S_4L_1Hc, has oxidation state (IV-IV-III-IV) with the Jahn-Teller axis of Mn3(III) orienting towards O5/O6. Other two configurations, S_4L_1Ha and S_4L_1Hb, have oxidation state (III-IV-IV-IV).

For S_4L_1Ha, the peroxide is formed between W2 and O6 (pink dashed line in Figure 4.6). For S_4L_1Hb, the energy scan is also performed with a broken-symmetry state ($S = 7/2$) by "flipping" the spin of Mn4. However, the peroxide products have more than 30 kcal/mol energies than the reactants and none of scans show a low energy

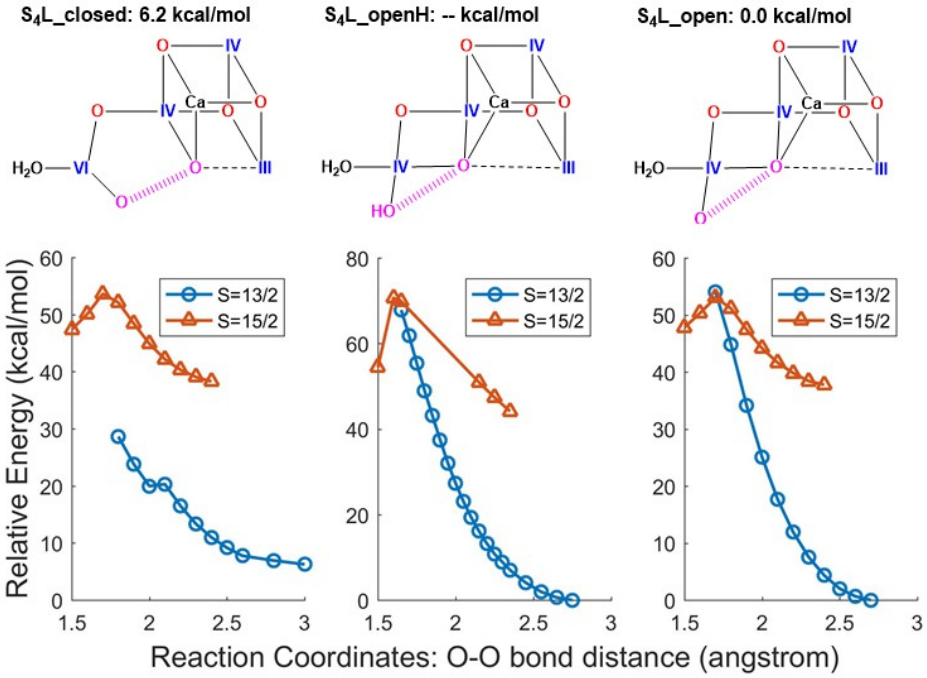

Figure 4.5: Relative energetics, oxidation states, and energy profiles of peroxide formation of S_4L configurations without additional water introduced. The pink thick dashed lines indicate the two substrate water. Peroxide formations are investigated with different spin states.

barrier.

Two-protons configurations. We examine configurations with one more proton than the previous section. These configurations (Figure 4.7) differ not only in geometries but also in the oxidation state pattern, i.e. where the Mn^{III} resides (on Mn1, Mn3, or Mn4). For example, S_4L_2H1d and S_4L_2H1e have the same protonation states, but the former has Mn4(III) with the Jahn-Teller direction towards the carboxylates of D1-Asp170 and D1-Glu333 while the latter has Mn3(III) with the Jahn-Teller direction towards O5. S_4L_2H1d' and S_4L_2H1h' have relative lower energies compared with others, which may be caused by the additional hydrogen bonds introduced by different coordinates of D1-Asp170, e.g. H-bond between D1-Asp170 and W1. These two configurations are not considered further.

Similar to S_2L configurations, both "open" (S_4L_2H1a, 2H1b, 2H1c, 2H1f, 2H2, and 2H3) and "closed" (S_4L_2H1d, 2H1e, and 2H1h) forms are observed. Moreover, a third geometric form is obtained, i.e. S_4L_2H1g, which is semi open closed ("SOC"

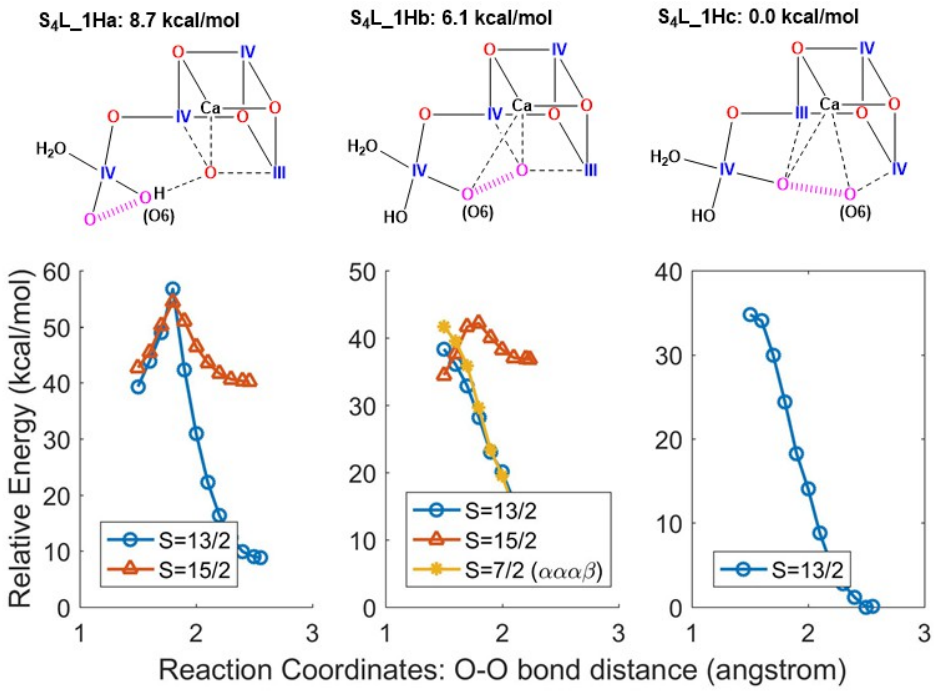

Figure 4.6: Relative energetics, oxidation states, and energy profiles of peroxide formation of S_4L configurations with one proton distributed among W2, O5, and O6. The pink thick dashed lines indicate the two substrate water. Peroxide formations are investigated with different spin states.

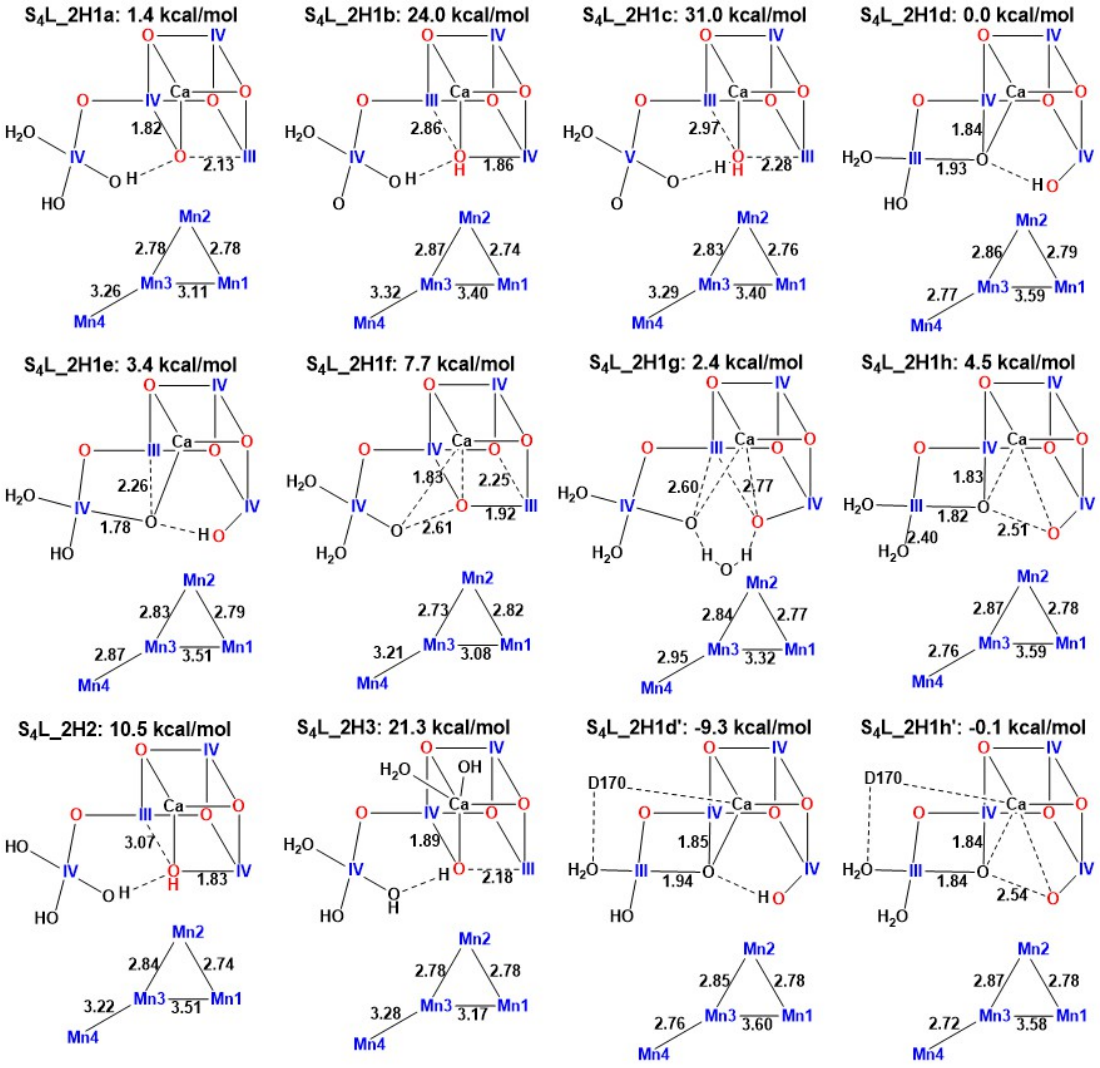

Figure 4.7: Geometries and energetic properties of S_4L isomers without additional water ligand (OH^-) in the low oxidation paradigm.

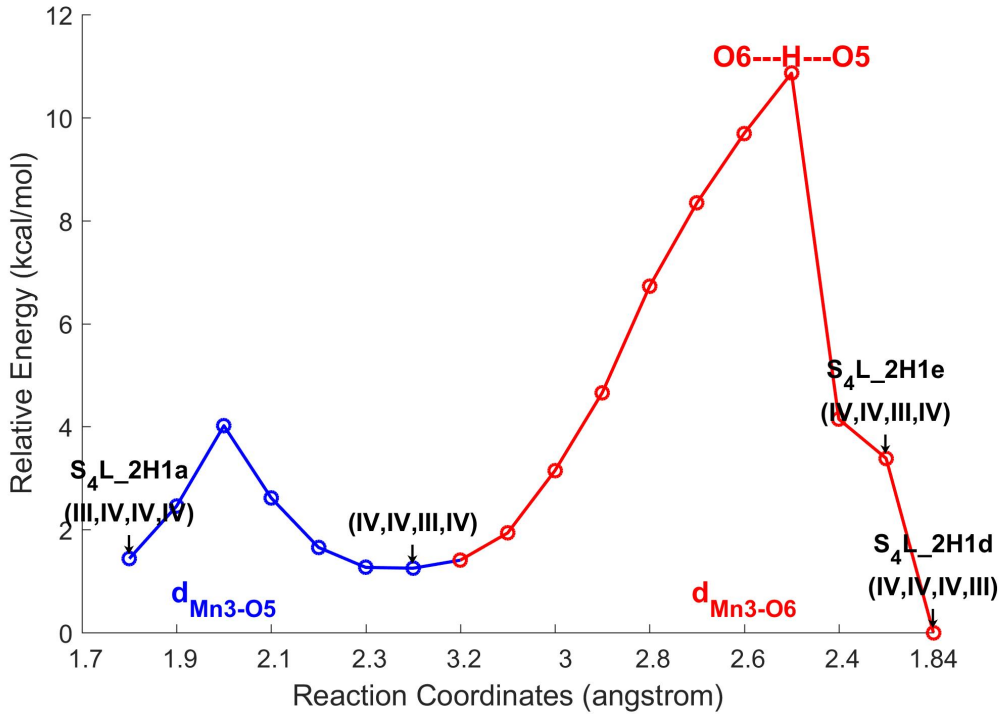

Figure 4.8: Energy profile of the transition between two S_4 configurations: left and right inserted OH^- ligand.

in abbreviation). The Jahn-Teller axis of Mn3(III) of S_4L_2H1g orients the empty *d* orbital towards O5/O6. These two substrate oxygens not only forms strong bond with Mn1 and Mn4, respectively, but also have relatively short distances with Ca (around 2.4 Å).

S_4L_2H1a and S_4L_2H1d are another pair of "open" and "closed" forms with the same protonation state. The corresponding "SOC" form may be regarded as S_4L_2H1e. To investigate the transitions among "open", "closed" and "SOC" forms in S_4 state, we perform relaxed scans by first scanning the Mn3-O5 distance from S_4L_2H1a to reach a state with (IV-IV-III-IV) (blue line in Figure 4.8), followed by relaxed scan along Mn3-O6 to reach S_4L_2H1d (red line in Figure 4.8). It turns out the rate-determining step is the proton transfer process between O6 and O5. The potential energy barrier is smaller than 10 kcal/mol.

As a result, we have proved that the "open" (one additional hydroxyl ligand on

Mn1) and "closed" (one additional hydroxyl ligand on Mn4) S_4L forms are interconvertible. This large flexibility of the O5/O6 not only suggests the possibility of an additional water molecule entering this space[44, 120], but also implies that the OEC can reorganize its connectivity to reach a "better" form after accepting the additional water ligand. For example, the additional water ligand may first be introduced on Mn4 because of the easy access to water, followed by the reorganization OEC to the "open" form which has a lower energy.

Energy profiles of peroxide formations of selected configurations, S_4L_2H1a, S_4L_2H1b, and S_4L_2H1g, are shown in Figure 4.9. For S_4L_2H1a and S_4L_2H1b, it is a mono Mn mechanism, in which the coupling occurs between the two terminal water ligands on Mn4. For S_4L_2H1g, the coupling occurs between O5, bonding to Mn1, Mn3, and Ca, and O6, bonding to Mn4, Mn3, and Ca. A crystallographic water forms two hydrogen bonds with O5 and O6 to stabilize the OEC. The energy scan is performed with $S = 13/2$, a broken-symmetry state ($S = 1/2$) by flipping the spins of Mn1 and Mn2, and two other states with $S = 15/2$. These two states ($S = 15/2$) differ in where the oxyl-radical resides, i.e. one has (IV-IV-III-III) plus Mn4-O$\cdot$, and the other has (III-IV-III-IV) and Mn1-O$\cdot$. However, similar to Figure 4.6, none of them has low energy peroxide product or barrier.

S_4L_2H2 and S_4L_3H3 have quite different protonation states from others by including protonation states of W1 and W4. They have relatively higher energies and are related to peroxide formations of W1-W2 and W3-W4.

Two-protons peroxide products. Various peroxides products based on the configurations in Figure 4.7 have been obtained (Figure 4.10). The peroxide can be formed by couplings of W1 plus W2 (peroxo_L1, L2, L3, L4), W2 plus O6 (peroxo_L5, L6, L7), O6 plus W3 (peroxo_L8, L9), W3 plus W4 (peroxo_L10, L11, L12), and O6 plus O5 (peroxo_L13, L14). Two oxidation state patterns have been observed, (III-IV-IV-II) and (III-IV-III-III), which are also seen in S_2 state in Chapter 3. Again, all of them have significantly higher energies than S_4L_2H1d, one of the reactant candidates.

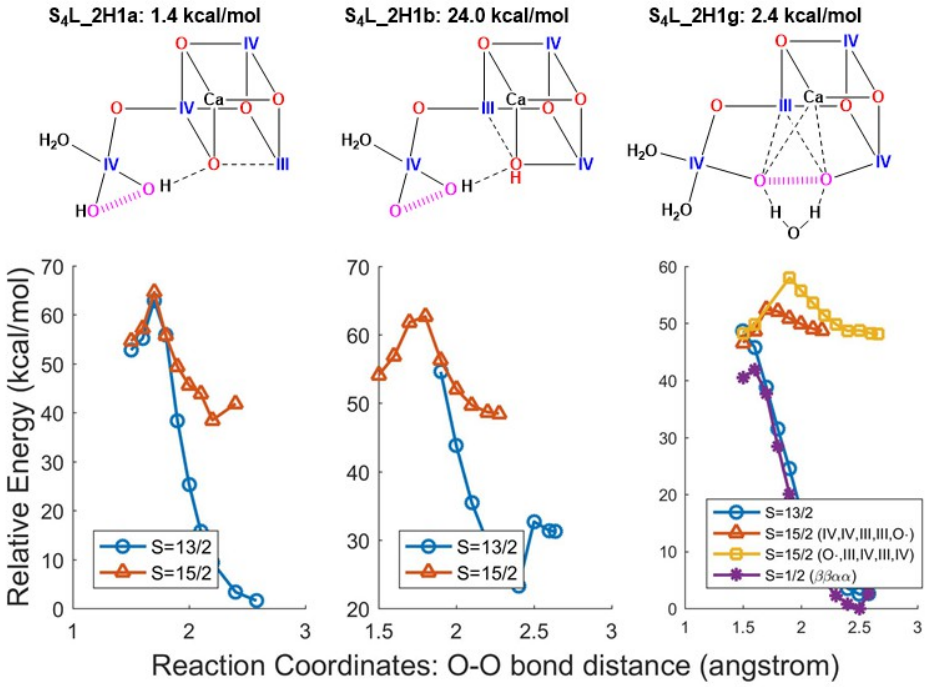

Figure 4.9: Relative energetics, oxidation states, and energy profiles of peroxide formation of selected S_4L configurations with two protons distributed among W2, O5, and O6. The pink thick dashed lines indicate the two substrate water. Peroxide formations are investigated with different spin states.

4.3.3 High paradigm

As a comparison, S_4 high paradigm models are also considered towards the peroxide formation (Figure 4.11). S_4H_lO and S_4H_rO differ in the position of the additional oxide ligand, with the former having it on Mn4 and the latter having it on Mn1. The oxidation states are (IV-IV-IV-V) and (V-IV-IV-IV), respectively.

Both configurations can proceed to peroxide with reasonable energy barrier (< 16 kcal/mol) (Figure 4.11). The energy profile is obtained by scanning along the O–O distance with broken symmetry states, $S = 7/2$ for S_4H_lO and $S = 5/2$ for S_4H_rO, i.e. the spin of Mn4 is flipped. Upon the peroxide forms, two electrons transfer from the two oxygens to Mn1 and Mn4, resulting in (III-IV-IV-IV) and (IV-IV-IV-III), respectively. The mechanism is similar to the radical coupling mechanism[80], where O5 and a terminal oxyl-radical from a non-crystallographic water form the peroxide. However, there is no significant spin observed on the two substrate oxygens, i.e. no oxyl-radical is observed during the energy scans in both configurations in our calculations.

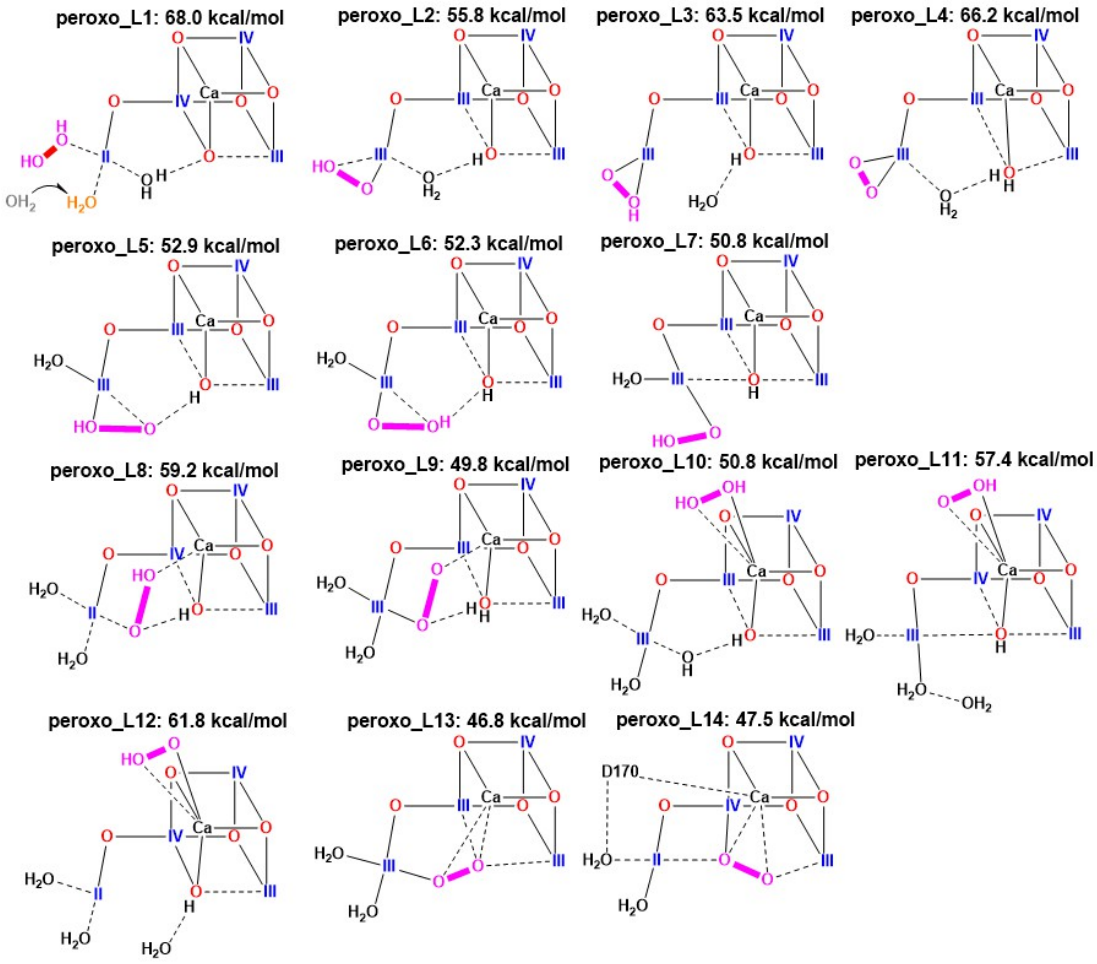

Figure 4.10: Peroxide products of various configurations under the low paradigm. The pink atoms are directly involved in the O–O bond formation. The reference energy configuration is S_4L_2H1d in Figure 4.7.

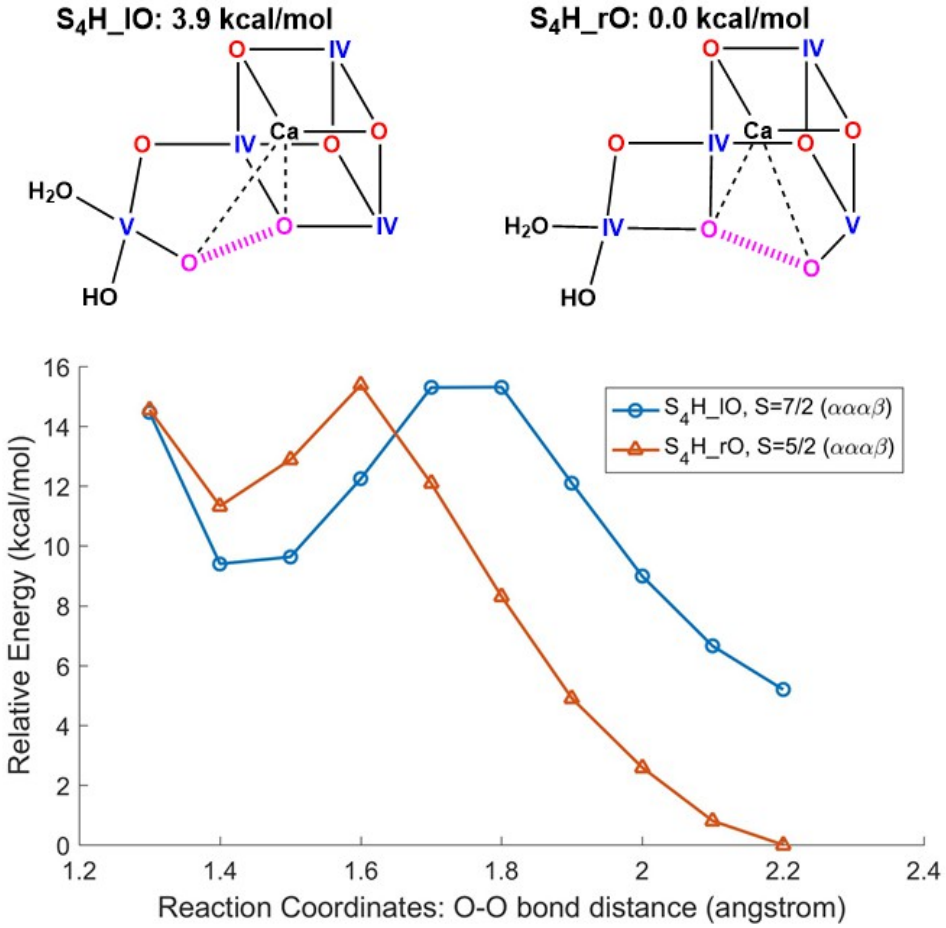

Figure 4.11: Peroxide formation under the high paradigm. The pink atoms are directly involved in the O–O bond formation.

4.4 Conclusions

We have studied geometric, energetic, and spectroscopic properties of several structural configurations of the S_3 state in the low paradigm and S_4 state in both the low and high paradigms. The complexity arises from a variety of protonation states and the choice of the additional water (H_2O or OH^-).

For S_3L configurations without the additional water, three short Mn-Mn distances can be obtained, e.g. S_3L_2Ha, consistent with the EXAFS data. However, the configurations with ground state $S_{GS} = 3$ have only two short Mn-Mn distances (Mn1-Mn2 and Mn2-Mn3 < 2.8 Å) and relatively long Mn3-Mn4 (> 2.95 Å), e.g. S_3L_3Ha in Figure 4.2. Two configurations (S_3L_3Hb, S_3L_3Hb_HIE) transfer one proton from W1 to D1-Asp61, which indicates a possible pathway of proton transfer towards the lumen.

For configurations with the additional water on Mn4 (S_3_lw), long Mn3-Mn4 is produced (> 3.0 Å), which is not consistent with the EXAFS data. Configurations with O6 on Mn1 (S_3_rw) tend to have lower energies compared with the corresponding S_3_lw models, e.g. S_3_rw4H has 1.0 kcal/mol lower energy than S_3_lw4H. Although we have not found S_3_rw configurations that satisfy both the EXAFS requirement and EPR experiments ($S = 3$) simultaneously, these two criteria can be reached with different configurations. More importantly, the Jahn-Teller direction of the Mn^{III} ion has significant influence on the Mn-Mn distances and exchange coupling parameters. Since we have not exhausted all the possibilities, such as all possible directions of Jahn-Teller axis, we can not exclude low paradigm assumption.

We observe that D1-Asp170 may rearrange from bidentate (Mn4, Ca) to bidentate (W1 (H_2O, Ca). It implies the important role of D1-Asp170 as a proton acceptor for substrate water deprotonation. In addition, the additional water ligand O6 (OH^-) can replace D1-Asp170 and bond to Ca and Mn4 (S_3L_lw2Hb), which indicates a possible pathway of introduction of new substrate water.

^{55}Mn HFCs of S_3 state with ground state $S_{GS} = 3$ are calculated. With an additional water ligand on Mn1, the HFCs fall into two classes: large coupling (Mn1/Mn2) and small coupling (Mn3/Mn4). Although S_3L_3Ha matches the HFCs fairly well, it has

only two short Mn-Mn distances and Mn3-Mn4 (2.92 Å). We propose a rearrangement of the Jahn-Teller axis of Mn1(III) together with a proton transfer from W2 (H_2O) to O6 (OH^-) to convert S_3L_3Ha into S_3L_3Hc, which has lower energy and three short Mn-Mn distances, to explain the EXAFS data.

S_4L configurations have also been examined extensively, either with or without the additional water (O6). We have proved that the "open" and "closed" forms of the S_4L configurations, i.e. S_4L_2H1a and S_4L_2H1d, are interconvertible with a energy barrier (< 10 kcal/mol) that is rate-determined by a proton transfer from O6 to O5. However, all the attempts towards the peroxide formation in the low paradigm fail to produce a reasonably low energy barrier. We conclude that it is still lack of a computationally feasible mechanism in the low paradigm and a different peroxide formation mechanism is needed, possibly with significant rearrangements of the amino acid ligands, e.g. D1-Asp170 or D1-Glu333.

Chapter 5

O–O Bond Formation of Cobalt Catalyst

5.1 Overview

Artificial catalysts aim to mimic the oxygen evolving complex in Photosystem II by developing simplified but efficient routes from earth abundant metals to generate chemical fuels, e.g. H_2, directly from sunlight. First row transition ions have been widely sought as water oxidation catalysts, e.g. Mn[81, 141], Ru[141, 142], and Co[143, 12, 13], to replace noble catalysts. To better understand their basis for catalysis, molecular cobalt clusters have been developed, especially clusters containing a Co_4O_4 "cubane"[144, 143, 145, 13], which poses large similarity with the OEC and appeared in synthetic water oxidation catalysts repeatedly[81].

The study of peroxide and dioxygen formation of cobalt catalysts have been ongoing for decades. Mattioli *et al.*[12] applied *ab initio* DFT+U molecular dynamics calculations on a cobalt-based catalyst (CoCat) in explicit water solution and proposed a pathway for oxygen evolution (Figure 5.1), in which the formation of Co(IV)-oxyl species was identified as the driving ingredient for the activation of the catalytic mechanism, followed by their geminal coupling with oxygen atoms coordinated by the same Co. They also claimed that the nucleophilic attack processes of external water molecules to the oxyl radicals have high potential energy barriers, hence are discouraged.

Similar mechanism is also suggested by Smith *et al.* on a cobalt cluster containing a Co_4O_4 "cubane" core[13]. They applied DFT calculations to predict the energetics of formation of intermediates with progressive addition or exchange of ligands for water and hydroxide. They showed that $Co_4O_4(OAc)_4(py)_4(ClO_4)$ ($\mathbf{1A}^+$) is able to react with hydroxide (OH^-) to produce O_2 (Figure 5.2). The Co_4O_4 "cubane" architecture is proposed to allow thermodynamically accessible oxidation to Co^{4+}.

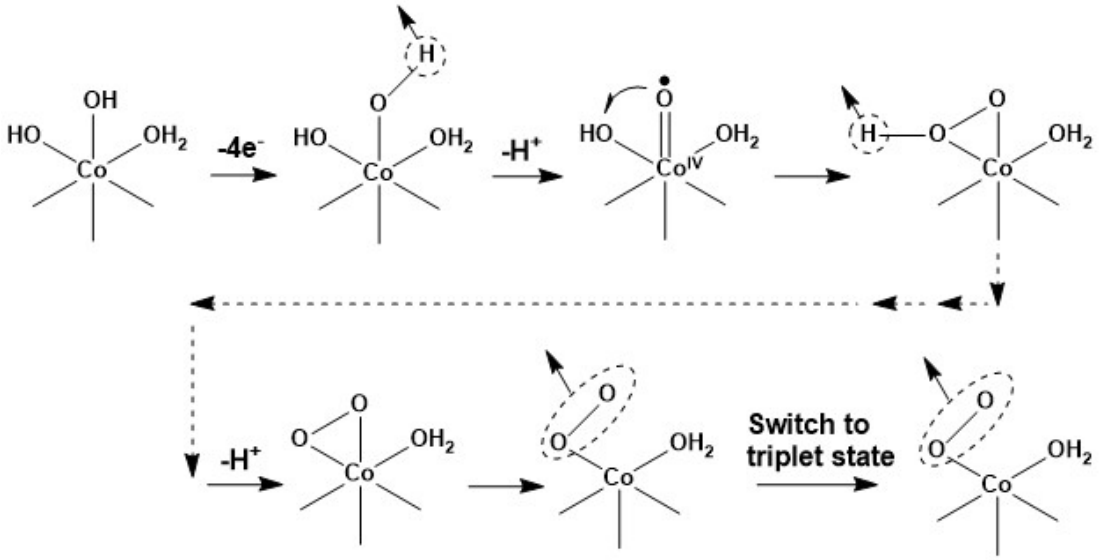

Figure 5.1: Reaction path for oxygen evolution of a cobalt-based catalyst proposed by Mattioli *et al.*. The scheme is reconstructed from Ref.[12].

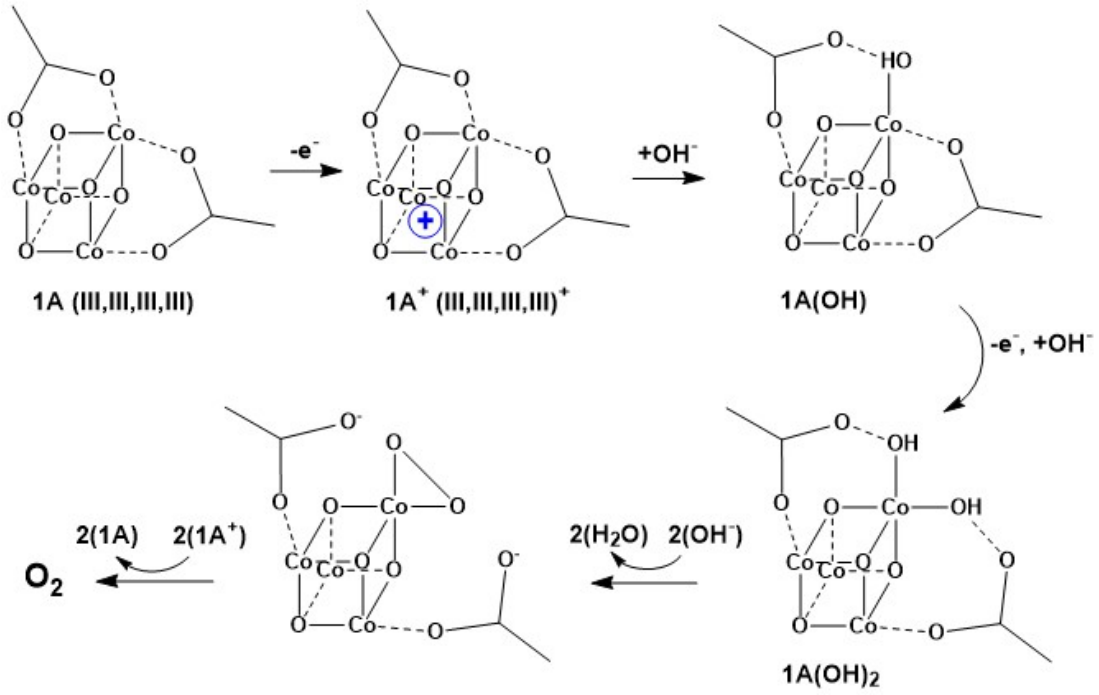

Figure 5.2: Proposed mechanism of hydroxide oxidation by of **1A** by Smith *et al.*[13]. The scheme is reconstructed from Ref.[13].

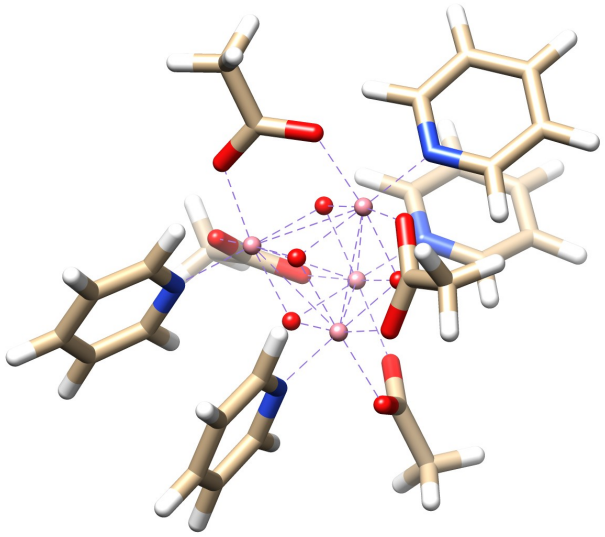

Figure 5.3: Structure of $Co_4O_4(OAc)_4(py)_4$.

We find that Smith *et al.*[13] did not have enough computational studies of the peroxide and oxygen formations of the cobalt cluster. Since it is important to investigate those details to reveal the fundamentals of O–O formation mechanism of the Co_4O_4 cubane, we now perform quantum chemical calculations on intermediates along the O–O formation of **1A** and compare it with the corresponding mechanism on the OEC in PSII.

5.2 Methodology

5.2.1 Structural Models

The optimized structure of $Co_4O_4(OAc)_4(py)_4$ (**1A**), using the quantum chemical calculations described below, is shown in Figure 5.3. The optimized *gem*-dihydroxo intermediate $[\mathbf{1A}(OH)_2]^0$ and labeling scheme are shown in Figure 5.4.

5.2.2 Computational Details

QM calculations were performed with ORCA[85]. Geometry optimizations were carried out with BP86 functional[86, 28], which often yields more realistic structural parameters than hybrid functionals[87]. Polarized valence double-zeta basis sets (def2-SVP)[88]

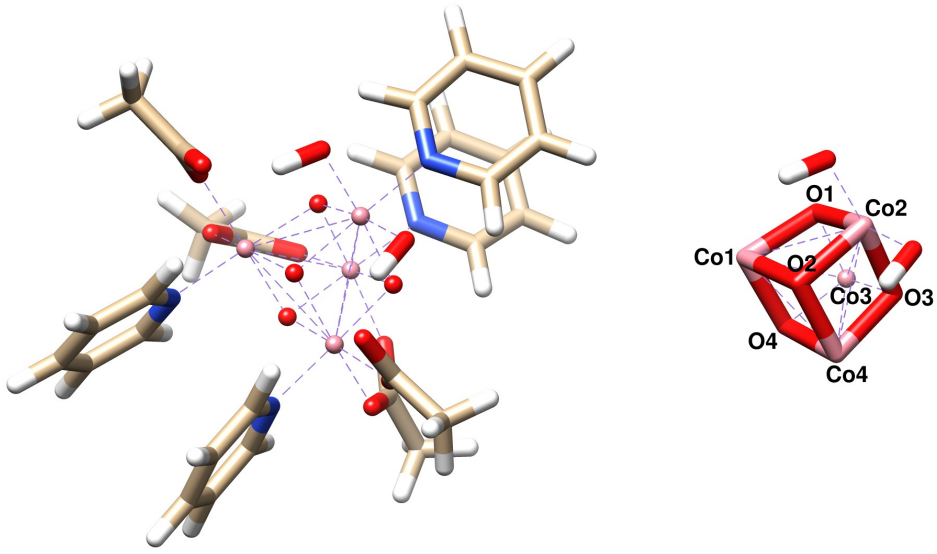

Figure 5.4: Structure of *gem*-type $Co_4O_4(OAc)_4(py)_4(OH)_2$ and the labeling scheme, in which two OH^- bound to Co2.

were used for all elements. The calculations take advantage of the resolution of identity (RI) approximation with the auxiliary def2-SVP/J Coulomb fitting basis sets[88] as implemented in ORCA. Tight convergence, increased integration grids (Grid4 in ORCA convention) and an unrestricted Kohn-Sham method were used. The influence of the environment was simulated using the conductor-like screening model (COSMO)[90] assuming a permittivity of 80.0, i.e. for water.

For the energy scans towards peroxide formation, different possible spin states are applied and the lowest energies are chosen to construct the energy profile.

5.3 Results and Discussion

5.3.1 Geometric and Electronic Properties of Co_4O_4

The Co-Co distances and Mulliken spin populations of different structures of the cobalt cluster are summarized in Table 5.2 and Table 5.1, respectively. The ground state of **1A** is $S_{GS} = 0$, where all Co ions are in low spin configuration. The Co_4O_4 cubane has a highly symmetric geometry. For **1A** and $\mathbf{1A}^+$, we have $d_{\text{Co1-Co2}} = d_{\text{Co1-Co3}} = d_{\text{Co2-Co4}} = d_{\text{Co3-Co4}}$ and $d_{\text{Co1-Co4}} = d_{\text{Co2-Co3}}$. The spin populations of $\mathbf{1A}^+$ ($S_{GS} = 1/2$) distribute almost evenly among four Co ions. The spin populations of the bridging

Table 5.1: Mulliken spin populations of different states of the cobalt cluster.

	Co1	Co2	Co3	Co4	O1	O2	O3	O4	OH^-	OH^-
$\mathbf{1A}^+$	0.21	0.21	0.21	0.20	0.047	0.046	0.046	0.046	–	–
$\mathbf{1A}(OH)^0$	0.08	0.55	0.05	0.05	0.048	-0.021	0.021	0.012	0.22	–
$\mathbf{1A}(OH)^+$	0.33	0.67	0.22	0.18	0.034	0.073	0.029	0.055	0.32	–
$\mathbf{1A}(OH)_2{}^0$	0.25	0.75	0.16	0.25	0.027	0.126	0.028	0.021	0.17	0.17

Table 5.2: Co-Co distances of different states of the cobalt cluster.

	1A	$\mathbf{1A}^+$	**1A**(OH)	$\mathbf{1A}(OH)^+$	$\mathbf{1A}(OH)_2$
Co1-Co2	2.72	2.68	2.83	2.84	2.84
Co1-Co3	2.72	2.68	2.72	2.73	2.73
Co1-Co4	2.84	2.84	2.85	2.88	2.90
Co2-Co3	2.84	2.84	2.89	2.88	2.92
Co2-Co4	2.72	2.68	2.71	2.72	2.84
Co3-Co4	2.72	2.68	2.70	2.70	2.73

oxides of $\mathbf{1A}^+$ are negligible.

With the addition of one hydroxide ($\mathbf{1A}$(OH)), one OAc (labeled as OAc1) rearranges from bidentate (Co1 and Co2) to only bound to Co1 while forming a hydrogen bond with the added OH^-. The resulting geometry is also distorted, e.g. Co1-Co2 becomes much longer. The corresponding Mulliken spin population changes significantly, where most of the spin populations are distributed among the added OH^- and Co2, the cobalt ion that connects it.

Losing another electron leads us to $\mathbf{1A}(OH)^+$ with ground state $S_{GS} = 1$. The geometry does not change much compared with $\mathbf{1A}$(OH). The additional spin is distributed among four Co ions and the added OH^-. Adding the second OH^- gives $\mathbf{1A}(OH)_2$, in which Co2 has two OH^- ligands and the highest spin populations among all Co ions (Table 5.1). It also possesses high symmetry, e.g. $d_{\text{Co1-Co2}} = d_{\text{Co2-Co4}}$, $d_{\text{Co1-Co3}} = d_{\text{Co3-Co4}}$, and $d_{\text{Co1-Co4}} < d_{\text{Co2-Co3}}$. It is interesting to note that O2 also shows significant spin populations compared with other bridging oxides, which most likely arises from its unique position in $\mathbf{1A}(OH)_2$.

5.3.2 O–O Bond Formation

Cobalt Cubane

Peroxide formation. To investigate the O–O bond formation mechanism of **1A**, we start with **1A**$(OH)_2$, which has 3.5 average oxidation states. The complexity comes from the choice of whether removing more protons before the O–O formation. Hence, we examined three cases: 0 proton removed, 1 proton removed, and both protons of the additional hydroxides removed. Moreover, we are not sure how many electrons should have been extracted from the Co_4O_4 cubane when the peroxide formation occurs. Hence, three different average oxidation states are also considered: 2 electrons removed (-2e) from **1A**, 3 electrons removed (-3e), and 4 electrons removed (-4e). As a result, nine different configurations with different protonation or oxidation states are considered. Making it more complex, we need to perform energy scans along the O–O distance with different possible spin states in order to calculate the energy profile. For example, **1A**$(OH)_2$ has two spins, hence the spin states can be either $S = 0$ or $S = 1$. The lowest energy among all calculations with different spin states for the same O–O distance is chosen for the construction of the energy profiles. The energy profiles are grouped according to protonation states and shown in Figure 5.5, 5.6, and 5.7.

From Figure 5.5, 5.6, and 5.7, we see that the potential energy barrier towards peroxide formation decreases as more electrons are removed. As an example, configurations with two hydroxides shows the energy barrier is reduced from about 25 kcal/mol to less than 10 kcal/mol along with more electrons extracted from the Co_4O_4 cubane (Figure 5.5). Upon the formation of peroxide, the protons (if any) of OH^- moves to nearby OAc, which in turn forms hydrogen bond with O2. With 4 electrons removed, e.g. $[\mathbf{1A}(OH)_2]^{2+}$, the peroxide product automatically forms superoxide (the summation of the spin populations on the two corresponding oxygens ≈ 1.0). Configurations with one proton removed show similar characters (Figure 5.6). For configurations with two protons removed (Figure 5.7), peroxide formation becomes energy accessible even for "-2e" state. The decrease of potential energy barrier as more electrons are removed is not significant any more.

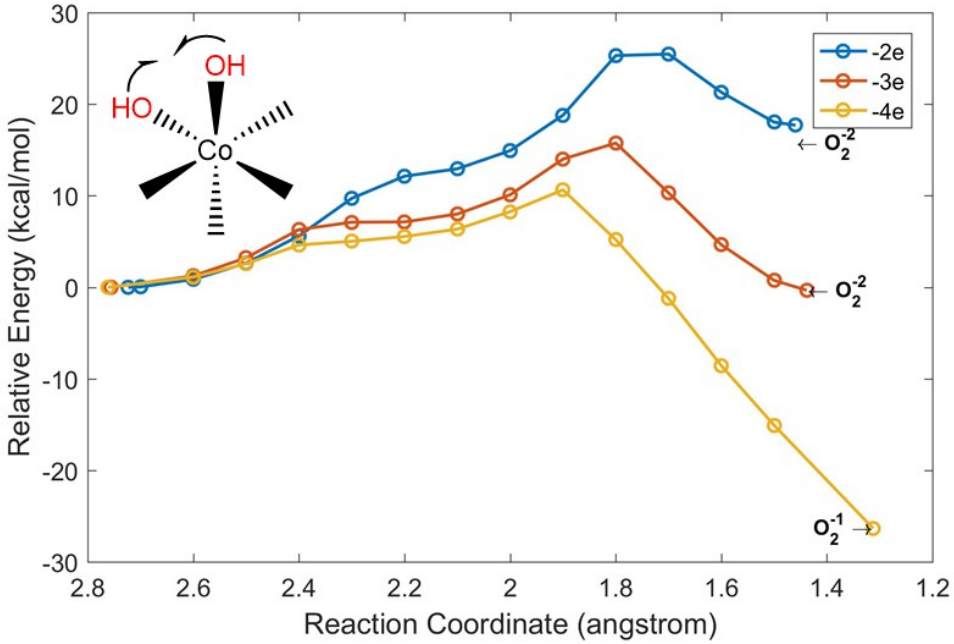

Figure 5.5: Energy profile of peroxide formation between two hydroxides of the cobalt cluster with 2, 3, and 4 electrons removed.

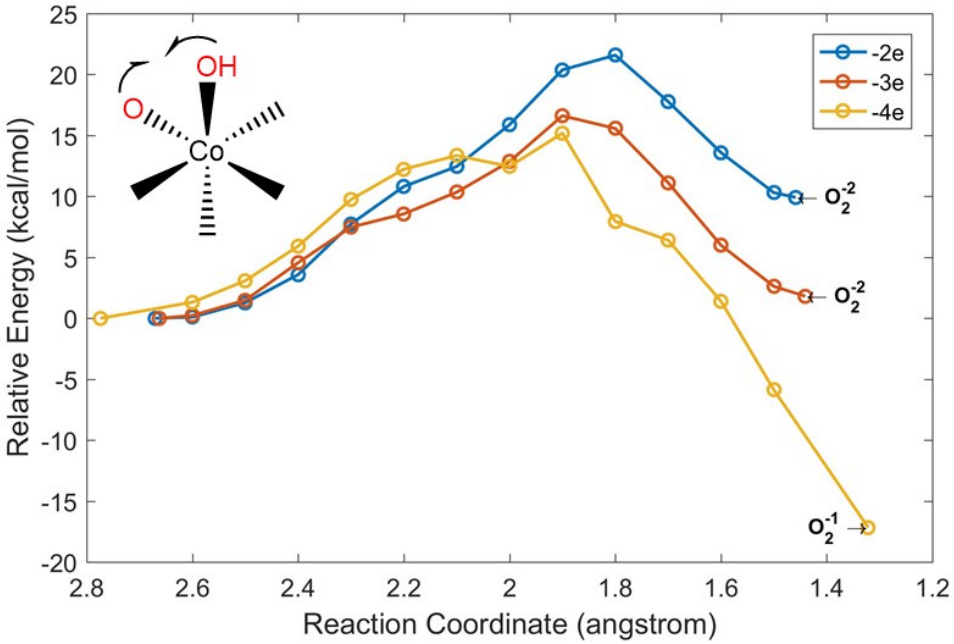

Figure 5.6: Energy profile of peroxide formation between one hydroxide and one oxide of the cobalt cluster with 2, 3, and 4 electrons removed.

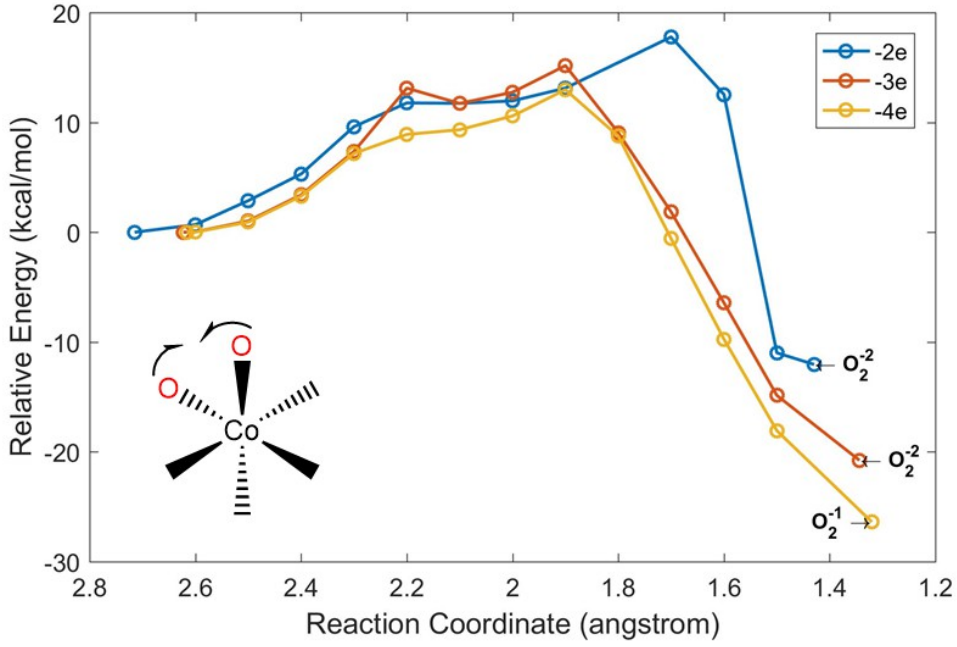

Figure 5.7: Energy profile of peroxide formation between two oxides of the cobalt cluster with 2, 3, and 4 electrons removed.

Dioxygen formation. To form dioxygen, it requires four electrons in total. Configurations with four electrons removed can produce peroxide with energy barrier less than 15 kcal/mol and the peroxide automatically gets oxidized to generate superoxide. However, further decrease of O–O bond distance does not produce dioxygen directly. In order to do so, it is necessary to detach the O-O species from the Co_4O_4 cubane while keeping the spin state as $S = 1$, i.e. a triplet state. One way to detach the O-O species is to increase the Co2-O distance directly. The other way is to use OAc to substitute the O-O species and bound to Co2. To simplify the presentation, we adopt the second approach and focus on $[\mathbf{1A}O_2]^0$.

The Mulliken spin populations and energy profile are shown in Figure 5.8. The spin populations are two summations over the O–O species and four Co ions. We first perform relaxed scan along OAc1-Co2 (blue line in Figure 5.8B). From the corresponding spin populations, the O–O species stays as superoxide with spin population ≈ 1.0. OAc1 substitutes one of the oxygens and becomes the new ligand to Co2 with a potential energy barrier < 5 kcal/mol. After this process, a relaxed scan along OAc2-Co2

is conducted. The final product is O_2, which can be verified by the spin population analysis showing spin ~ 2.0 on the O–O species. After OAc2 replaces O–O and bound to Co2, the cobalt cluster returns back to **1A** with ground state $S = 0$. The transition state indicates the process of spin transfer from the Co_4O_4 to the O–O species and the energy barrier is < 13 kcal/mol.

Oxygen Evolving Complex

We now examine the behavior of the OEC in terms of peroxide formation when more electrons are extracted from the cluster. The configuration under consideration is S_4L_2H1a. Two more configurations are obtained with one and two electrons removed. The role of the dangle Mn4 is similar to that of Co2, i.e. connecting to two substrate hydroxides. O5 (O^{2-}) can be regarded one of the proton acceptors, while a nearby water molecule is the other one. Hence, they mimic the role of the OAc in the cobalt cluster. Again, we performed relaxed scan along the O–O bond distance with two spin states, corresponding to the high spin states of the reactant and product, and the resulting energy profiles are shown in Figure 5.9. Similar to the case of cobalt cluster, with more electrons removed from the cluster, the peroxide formation tends to have lower energy barrier and the peroxide product tends to have lower energy. However, the energy barrier is not sufficiently low, hence this mechanism is rejected for the OEC.

Besides the geometric differences between the cobalt cluster and OEC, they also show quite different electronic properties. In the cobalt cluster, spin populations are distributed among all Co ions in the cubane and the two hydroxides, and the Co ion that connects the two hydroxides has relatively higher spin population than other Co ions. This special pattern, i.e. two hydroxides with radical character and high spin population connecting Co ion, may facilitate the formation of a peroxide species, consistent with the argument that the Co_4O_4 "cubane" architecture allows thermodynamically accessible oxidation to Co^{4+}[13]. In the OEC cluster, the spin populations are more localized and the substrate hydroxides have lower spin populations than the corresponding hydroxides in cobalt cluster. This may explain why the very similar mechanism does not work on the OEC.

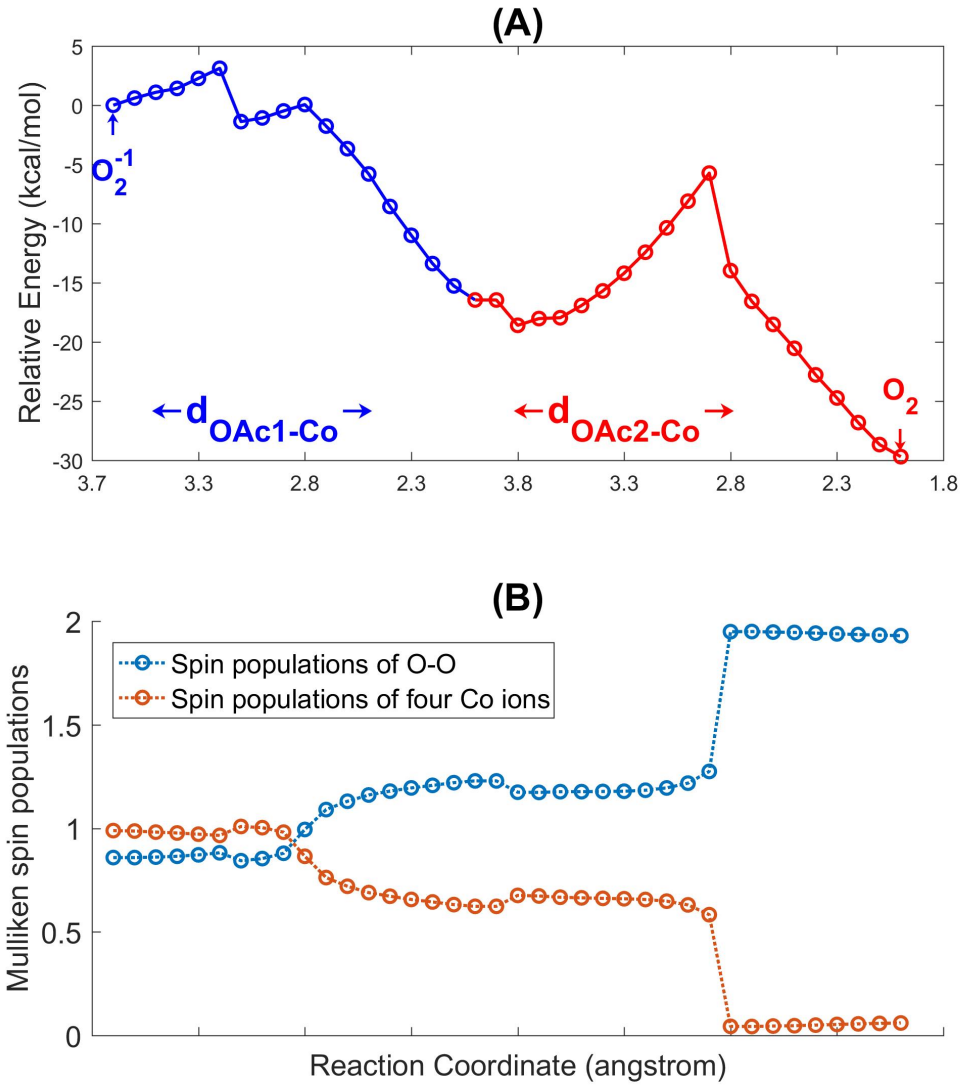

Figure 5.8: Mulliken spin populations and energy profile of dioxygen formation in cobalt cluster $[\mathbf{1A}O_2]^0$.

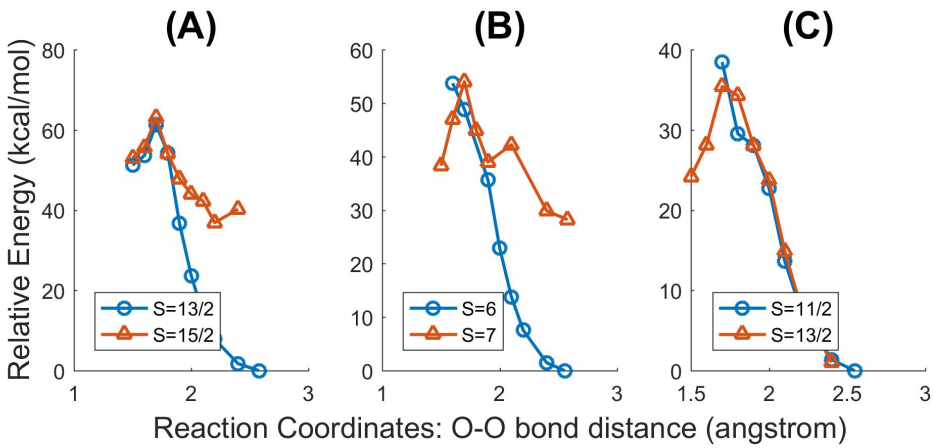

Figure 5.9: Energy profiles of peroxide formation in the oxygen evolving complex with different oxidation states. (A): $[S_4L\_2H1a]^0$, (B): $[S_4L\_2H1a]^+$, (C): $[S_4L\_2H1a]^{2+}$.

5.4 Conclusions

In conclusion, we have studied geometric and electronic properties of the cubane cluster $Co_4O_4(OAc)_4(py)_4$. The introduction of two hydroxides breaks the symmetry of the structure. The spin populations are distributed among the cubane and the two hydroxides. Peroxide formation is energy accessible when two protons are removed in advance or more than two electrons are extracted. The following dioxygen formation is revealed through DFT relaxed scans starting from a superoxide species for $[\mathbf{1A}O_2]^0$. It basically consists of two steps. In the first step, one OAc substitutes one oxyl-radical and becomes a ligand to the Co ion while the O–O species stays as superoxide. In the second step, the second OAc substitutes the other oxyl-radical, bounds to Co, and the Co_4O_4 cubane transfers its spin populations to the O–O species, resulting in O_2. We applied the same scheme on the dangle Mn in the OEC with various average oxidation states. The energy barrier does decrease as the more electrons are removed from the OEC cluster. However, no sufficiently low energy barrier is found. This difference most likely arises from the fact that spin populations are more localized and less spins reside on the substrate oxygens in the OEC. Further investigations may involve models with more protons removed from the OEC.

Chapter 6

Concluding Remarks and Future Directions

In this dissertation, the OEC in PSII under the low paradigm is studied extensively from S_0 to S_4 states.

For S_0 and S_1 states, we adopt QM/MM method to examine numerous protonation and oxidation states. The protonation states of O1, O2, and O4 are determined to be O^{2-} in the S_1 state. The protonation state of O3 is affected by the protonation state of His337. For S_1 state, we choose His337 as HIE and O3 in the form of O^{2-}. As for O5, we find that the position of O5 in the XFEL structure is more consistent with an OH^- under the low paradigm. Our calculations also reconcile the differences between 1.9 Å XRD and 1.95 Å XFEL structures by oxidation state redistribution together with simple proton relocation at His337 under the low paradigm. Moreover, the protonation states of the bridging oxygens and His337 determines the elongation or shortending Mn-Mn distances. Two short Mn-Mn distances are obtained with the oxidation state (III-IV-III-II), which is consistent with the results by Petrie *et al.*[61].

For S_2 state, geometric, energetic, and spectroscopic properties have been examined. Two interconvertible configurations, corresponding to MLS and $g \approx 4.1$ signals, have been discovered under the low paradigm with low energy barrier. These two configurations differ in the position of O5 (OH^-), resulting in "open" and "closed" forms. Similarly, two interconvertible Mn^{II}-containing configurations with positive His337 (HIP) have been observed, reproducing the $S_{GS} = 1/2$ (open) and $S_{GS} = 5/2$ (closed). Those configurations have the same number of atoms with the chosen S_1 models and one less electron, which is consistent with the argument that the two states differ only by a redox event, suggested by electrochromic measurements and the pH-insensitivity of the transition[146, 24]. We find that small perturbations, such as rearrangement of

hydrogen bonding network or position of O5, can produce energy accessible isomers with many different ground spin states, e.g. $S_{GS} = 7/2$, $9/2$, or $11/2$, which may be accounted for the $g = 10$ and 6 EPR signals. This evidence explains the experimental observation that the S_2 EPR signals vary depending on the preparation conditions. Hyperfine coupling tensors of S_2 configurations with $S_{GS} = 1/2$ under the low paradigm have been calculated and agree with earlier EPR experiments[3, 4, 5]. Energy accessible Mn^{II}-containing isomers are also considered and match partly the ENDOR experiments by Jin *et al.*[6]. Further investigations are needed to understand the effect of zero-field splitting of $Mn^{II/III}$ in S_2 state on the hyperfine coupling tensors.

For S_3 state, we studied various configurations with or without additional water ligand (H_2O or OH^-) bounding to Mn1 or Mn4. Three short Mn-Mn distances are obtained in some structures, but the same structures do not have the $S_{GS} = 3$ ground state. On the other hand, structures have ground state $S_{GS} = 3$ does not produce three short Mn-Mn distances. We find the direction of Jahn-Teller axis of Mn^{III} affects the related Mn-Mn distance and exchange coupling parameter (ground spin state). Since we have not exhausted all possible combinations of directions Jahn-Teller axis, we can not exclude low paradigm assumption. The ^{55}Mn HFCs of S_3 state with $S_{GS} = 3$ of configurations with an additional water ligand on Mn1 fall into two classes: large coupling (Mn1 and Mn2) and small coupling (Mn3 and Mn4). The best match is S_3L_3Ha with isotropic HFCs: -120 (Mn1), -85 (Mn2), 44 (Mn4), and -27 (Mn3). One may use two configurations for S_3 state: one has $S_{GS} = 3$ and matches isotropic HFCs (S_3L_rw3Ha), while the other matches EXAFS data (S_3L_rw3Hc). Further studies are still needed, since the low-paradigm models have signficant anisotropies which is inconsistent with experiments by Cox *et al.* indicating the ^{55}Mn HFCs of S_3 are isotropic.

For S_4 state and O–O bond formation, we examined various configurations with or without additional water ligand (O6). Currently, it is still lack of a computationally feasible mechanism in the low paradigm. Further study may focus on peroxide formation with different coordination environments around Mn4.

Besides oxygen evolving complex, a study on $Co_4O_4(OAc)_4(py)_4$ cubane cluster has been conducted. Peroxide and dioxygen formation mechanisms are revealed using

DFT calculations. However, OEC seems to show quite different property from the cobalt cubane and further investigations may concern the relationship between spin populations distribution (localized vs. delocalized) and peroxide formation.

Appendix A

Programs for Exchange Coupling Calculation and Hamiltonian Matrix Diagonalization

- **Program 1: compute the exchange coupling parameters given the energies and the "flips" scheme.**

```
# this script will compute the exchange coupling of OEC
# the hamiltonian is: H = -2*(J12*S1*S2 + J13*S1*S3 +
#      J14*S1*S4 + J23*S2*S3 + J24*S2*S4 + J34*S3*S4)

import sys
import numpy as np

HartreeToCM = 219474.6313705

def Hamiltonian(positions, spin):
    ''' it returns the coefficients of a Hamiltonian
        whose broken symmetry is determined by 'positions'
    '''
    coe = []
    for i in range(3):
        for j in range(i+1, 4):
            # negative sign is necessary
            coeValue = -2*spin[i]*spin[j]
            if positions[i] == 1:
                coeValue = -1 * coeValue
```

```
            if positions[j] == 1:
                coeValue = -1 * coeValue
            coe.append(coeValue)
    return coe

def buildHamiltonianMatrix(flips, spins):
    ''' build the coefficient matrix '''
    HH = []
    for item in flips:
        # 'positions' indicates which sites are flipped
        positions = [0, 0, 0, 0]
        for it in item:
            positions[it] = 1
        # 'coe[0] = 1' indicates an extra parameter
        coe = [1]
        for s in Hamiltonian(positions, spins):
            coe.append(s)
        HH.append(coe)
    return HH

def hartreeTocm(energies):
    ''' transfer hatree to cm-1 '''
    y = np.array([])
    for i in range(len(energies)):
        y = np.append(y, energies[i] * HartreeToCM)
    return y

def computeJex(num_site, spins, flips, energies):
    # convert hartree to cm-1
    energies = hartreeTocm(energies)
```

```
    # compute coefficient matrix
    HH = buildHamiltonianMatrix(flips, spins)
    # compute the least square solutions
    result = np.linalg.lstsq(HH, energies, rcond=-1)
    # print results
    print ('sum of residuals: ', result[1])
    print ('rank of coefficient matrix: ', result[2])
    print ('solutions:')
    print ('Constant offset: ' + str(result[0][0]))
    # 'JJ' is only valid for systems with four ions
    JJ = ['J12', 'J13', 'J14', 'J23', 'J24', 'J34']
    for i in range(len(JJ)):
        print (JJ[i] + ': ' + str(result[0][i+1]))

    return result[0][1:]

if __name__ == "__main__":
  # number of ions
  num_site = 4
  # spin values: Mn1-Mn4 (III, IV, III, III)
  spins    = [2, 1.5, 2, 2]
  # broken symmetry flips
  # order: high-spin, flip one site, flip two site, ...
  flips    = [[], [0], [1], [2], [3] ,[0,1], [1,2], [1,3]]
  energies = [-10493.901584764850, # high-spin configuration
              -10493.903231843165, # flip Mn1
              -10493.904504002987, # flip Mn2
              -10493.903126575717, # flip Mn3
              -10493.901474579234, # flip Mn4
              -10493.903894205421, # flip Mn1, Mn2
```

```
                -10493.902466717154, # flip Mn2, Mn3
                -10493.904381443350] # flip Mn2, Mn4
    # compute J couplings
    jcouplings = computeJex(num_site, spins, flips, energies)
    # compute: -2 * J
    hamiltonian = -2 * jcouplings
    print (hamiltonian)
```

- **Program 2: diagonalize the Hamiltonian matrix and compute the energy level spin ladder given the exchange coupling parameters.**

```
# this script computes the HDvV Hamiltonian - Perturbation
# matrixi given the spin of each individual site
# the perturbation is epsilon * Sz,
# where epsilon is a small positive number

import math
import numpy as np
from numpy import linalg as LA

# perturbation term, choose magic number 1e-5
epsilon = 1e-5
# threshold to determine whether two energies are degenerate
threshold = 1e-3

# "ladderUp" and "ladderDown" implements
# Ladder-Operator Method:
# => raising operator and lowering operator
# s: the spin number S
# m: Ms
def ladderUp(s, m):
```

```
    if m + 1 > s:
        return 0
    ss = float(s)
    mm = float(m)
    return math.sqrt(ss * (ss + 1) - mm * (mm + 1))

def ladderDown(s, m):
    if m - 1 < -s:
        return 0
    ss = float(s)
    mm = float(m)
    return math.sqrt(ss * (ss + 1) - mm * (mm - 1))

# Example: two ions with spins:
# => S1 = 1, S2 = 1.5
# the number of basisfunctions should be:
# => (2 * S1 + 1) * (2 * S2 + 1) = 12
def numberBasisFunction(num_site, spins):
    """ num_site: number of ions
        spins:    an array of spin numbers

        return the number of basis functions """
    dim = 1
    for i in range(num_site):
        dim = dim * (2 * float(spins[i]) + 1)
    return int(dim)

# Example: two ions with spins S1 = 1, S2 = 1.5
# then the Mss should be:
# => [[-1.0, 0.0, 1.0], [-1.5, -0.5, 0.5, 1.5]]
```

```
def buildMss(num_site, spins):
    """ num_site: number of ions
        spins:    an array of spin numbers

        return an array of arrays of all Ms """
    Mss = []
    for i in range(num_site):
        tmp = []
        ms  = -float(spins[i])
        while ms <= float(spins[i]):
            tmp.append(ms)
            ms = ms + 1
        Mss.append(tmp)
    return Mss

# "basisFunction" Example: there are two ions:
# => S1 = 1, S2 = 1.5
# spins = [1, 1.5]
# Mss   = [[-1.0, 0.0, 1.0], [-1.5, -0.5, 0.5, 1.5]]
# n     = 0
# this will have basis functions:
# [[1, -1.0, 1.5, -1.5],
#  [1, -1.0, 1.5, -0.5],
#  [1, -1.0, 1.5, 0.5],
#  [1, -1.0, 1.5, 1.5],
#  [1, 0.0, 1.5, -1.5],
#  [1, 0.0, 1.5, -0.5],
#  [1, 0.0, 1.5, 0.5],
#  [1, 0.0, 1.5, 1.5],
#  [1, 1.0, 1.5, -1.5],
```

```
#  [1, 1.0, 1.5, -0.5],
#  [1, 1.0, 1.5, 0.5],
#  [1, 1.0, 1.5, 1.5]]
def basisFunction(spins, Mss, n):
    """ spins: an array of the spin numbers
        Mss:   an array of arrays of all Ms of all Mn ions
        n:     depth of the recursive
               (input value should be 0,
                and the recursion stops when n == len(Mss))

        return: all possible basis functions
        The basis function has the format:
        => [S1, MS1, S2, MS2, ..., Sn, MSn] """
    if n == len(Mss):
        return []

    # recursive call
    partial_basis = basisFunction(spins, Mss, n+1)
    ans = []
    for ms in Mss[n]:
        if len(partial_basis) == 0:
            ans.append([spins[n], ms])
        else:
            for item in partial_basis:
                tmp = [spins[n], ms] + item
                ans.append(tmp)
    return ans

# "buildSteps" builds step lengths for locating the index
# For example, given two ions with S1 = 1, S2 = 1.5,
```

```
# the 12 basis functions are as follows:
# basis = [[1, -1.0, 1.5, -1.5],
#          [1, -1.0, 1.5, -0.5],
#          [1, -1.0, 1.5, 0.5],
#          [1, -1.0, 1.5, 1.5],
#          [1, 0.0, 1.5, -1.5],
#          [1, 0.0, 1.5, -0.5],
#          [1, 0.0, 1.5, 0.5],
#          [1, 0.0, 1.5, 1.5],
#          [1, 1.0, 1.5, -1.5],
#          [1, 1.0, 1.5, -0.5],
#          [1, 1.0, 1.5, 0.5],
#          [1, 1.0, 1.5, 1.5]]
# The "steps" array is:
# steps = [4, 1]
# With the same MS2, the index distance between two basis
# functions with adjacent MS1 is steps[0] = 4.
# i.e. basis[0] = [1, -1.0, 1.5, -1.5], basis[0 + steps[0]]
#                = [1, 0.0, 1.5, -1.5]
#      MS2 for basis[0] and basis[4] is -1.5, while MS1
#      for basis[0] and basis[4] are -1.0 and 0.0
def buildSteps(num_site, spins):
    """ num_site: number of ions
        spins:    an array of spin numbers

        return an array of numbers for locating the idx """
    steps = []
    for i in range(num_site):
        tmp = 1
        for j in range(i+1, num_site):
```

```
            tmp = tmp * (2 * spins[j] + 1)
        steps.append(int(tmp))
    return steps

def applyHamiltonian(spins, steps, hamilt, base, dim, b_idx):
    """ it apply the hamiltonian on to a basis function
        return the coefficients
        S_i * S_j = (S_i+ * S_j-)/2 + (S_i- * S_j+)/2
                    + S_iz * S_jz
        three steps in total

        spins: an array of the spin numbers
        steps: used for locating indices
        hamilt: -2 * Js
        base: basis functions
        dim: num of basis functions
        b_idx: offset of the index
    """
    # build the index pairs of the spins in hamiltonian
    # for OEC, indices:
    # => [[0, 1], [0, 2], [0, 3], [1, 2], [1, 3], [2, 3]]
    indices = []
    for i in range(len(spins)-1):
        for j in range(i+1, len(spins)):
            indices.append([i, j])

    # apply hamiltonian
    ans = dim * [0]
    for i in range(len(indices)):
        si = indices[i][0]
```

```
            sj = indices[i][1]
            # perform the S_i+ * S_j-
            index1 = b_idx + steps[si] - steps[sj]
            coe1 = ladderUp(spins[si], base[si*2 + 1]) *\
                   ladderDown(spins[sj], base[sj*2 + 1]) / 2
            # perform the S_i- * S_j+
            index2 = b_idx - steps[si] + steps[sj]
            coe2 = ladderDown(spins[si], base[si*2 + 1]) *\
                   ladderUp(spins[sj], base[sj*2 + 1]) / 2
            # perform S_iz * S_ij
            coe3 = base[si*2+1] * base[sj*2+1]
            if index1 >= 0 and index1 < len(ans):
                ans[index1] = ans[index1] + coe1 * hamilt[i]
            if index2 >= 0 and index2 < len(ans):
                ans[index2] = ans[index2] + coe2 * hamilt[i]
            ans[b_idx] = ans[b_idx] + coe3 * hamilt[i]

        return ans

    def applyPerturbation(epsilon, basis):
        """ epsilon: small perturbation value
            basis:   all the basis functions

            return the perturbation matrix """
        perturb_array = []
        for i in range(len(basis)):
            ms = 0
            for j in range(len(basis[i])//2):
                ms += basis[i][2*j+1]
            perturb_array.append(epsilon * ms)
```

```
    return np.diag(perturb_array)


def checkSym(m):
    """ check the symmetry of matrix m
        assume the elements are real numbers """
    d = len(m)
    for i in range(d):
        for j in range(i, d):
            if m[i][j] != m[j][i]:
                print ("i: " + str(i) + " j: " + str(j)\
                       + " => Not Equal!")
                return False
    return True


def computeSz(coe, ind, basis):
    """ compute the expected value on site S_z """
    ans = 0
    for i in range(len(coe)):
        if coe[i] != 0:
            ans = ans + coe[i]*coe[i]*basis[i][2*ind+1]
    return ans


def computeMs(coe, basis):
    """ compute the Ms """
    ans = []
    for i in range(len(coe)):
        if coe[i] != 0:
            tmp = 0
            for j in range(len(basis[i])//2):
                tmp = tmp + basis[i][2*j+1]
```

```
            ans.append(tmp)
    return ans

def computeMultiplicity(w):
    """ w: sorted eigen values of the hamiltonian matrix

        return the spin multiplicity of the ground state """
    ground_energy = w[0]
    multiplicity = 1
    # since we introduced a perturbation term,
    # we expect a small energy gap among the
    # eigen values of the same state
    for i in range(1,len(w)):
        if (w[i] - w[i-1] < threshold):
            multiplicity += 1
        else:
            break
    return multiplicity

def computeEnergyGap(w, Nlevels):
    """ w: sorted eigen values of the hamiltonian matrix
        Nlevels: number of energy levels needed """
    i          = 0
    index      = 0
    tot_s      = []
    energies   = []
    # since we introduced a perturbation term, we expect a
    # small energy gap among the eigen values of
    # the same state
    while index < Nlevels and i < len(w):
```

```
            tmp     = 0
            energy = w[i]
            while i < len(w):
                if (w[i] - energy < threshold):
                    tmp += 1
                    i += 1
                else:
                    break
            energies.append(energy)
            tot_s.append((tmp-1)/2.0)
            index += 1
        print ("Tot_s: ")
        print (tot_s)
        print ("Energy_gaps:")
        for i in range(len(energies)):
            print (energies[i] - energies[0])
        print


def extractInfo(hamilt_perturbation_matrix, basis, verb):
    """ extract information from hamiltonian matrix and basis
        functions """
    # diagonalize the hamiltonian matrix
    w, v = LA.eig(hamilt_perturbation_matrix)

    # sort w, v according to eigen values in ascending order
    sort_perm = w.argsort()
    w.sort()
    v = v[:, sort_perm]

    if verb == True:
```

```
        print ("eigen values: ")
        print (w)

    # determine the multiplicity of the ground spin state
    multiplicity = computeMultiplicity(w)
    print ("Multiplicity of the Ground Spin States: " +\
            str(multiplicity))
    if verb == True:
        print ("Energies:")
        print (w[0:multiplicity])

    # compute Ms and on-site Sz
    if verb == True:
        for i in range(multiplicity):
            print ("computeMs for " + str(i)\
                    + "-th eigenstate: ")
            print (computeMs(v[:, i], basis))
    for i in range(multiplicity):
        print ("expected on-site S using " + str(i) +\
                "-th eigenstate: ")
        for j in range(num_site):
            print ("Mn" + str(j) + ": " + \
                    str(computeSz(v[:,i], j, basis)))

    # compute the energy different of the five lowest levels:
    # => magic number 5
    Nlevels  = 5
    computeEnergyGap(w, Nlevels)

def computeEnergyLevel(num_site, spins, hamilt, verb=False):
```

```
    """ num_site: num of ions
        spins: spin values
        hamiltonian: -2 * J
        verb: indicates whether need more outputs """
    # compute the number of basis functions
    dim = numberBasisFunction(num_site, spins)

    # build vectors to hold all Ms
    Mss = buildMss(num_site, spins)

    # build the basis functions
    basis = basisFunction(spins, Mss, 0)

    # build steps for later use for locating the index
    steps = buildSteps(num_site, spins)

    # HDvV = sum (J_ij * S_i * S_j) = sum (J_ij *
    # ((S_i+ * S_j-)/2 + (S_i- * S_j+)/2 + S_iz * S_jz))
    Hnket = []
    for i in range(len(basis)):
        Hnket.append(applyHamiltonian(spins, steps, \
                    hamilt, basis[i], dim, i))

    # build the perturbation matrix with perturbation term:
    # epsilon * Sz, choose magic number 1e-5
    perturbation_matrix = applyPerturbation(epsilon, basis)

    # build the hamiltonian matrix, which is just the
    # coefficents matrix we just built
    hamilt_perturbation_matrix = Hnket + perturbation_matrix
```

```
    # hamiltonian matrix should be symmetric
    assert checkSym(hamilt_perturbation_matrix)

    # extract information from the hamiltonian matrix
    # and basis functions
    extractInfo(hamilt_perturbation_matrix, basis, verb)

if __name__ == "__main__":
    # Example
    # number of ions: 4
    num_site = 4
    # spins
    spins = [2, 1.5, 2, 2]
    hamiltonian = [41.18698825, 5.312322,
    8.91622866, 65.36981545, 0.13605338, -12.10883357]

    computeEnergyLevel(num_site, spins, hamiltonian, False)
```

References

[1] V. Krewald, M. Retegan, N. Cox, J. Messinger, W. Lubitz, S. DeBeer, F. Neese, and D. A. Pantazis, "Metal oxidation states in biological water splitting," *Chem. Sci.*, vol. 6, pp. 1676–1695, 2015.

[2] N. Cox and J. Messinger, "Reflections on substrate water and dioxygen formation," *Biochimica et Biophysica Acta (BBA) - Bioenergetics*, vol. 1827, no. 8, pp. 1020 – 1030, 2013. Metals in Bioenergetics and Biomimetics Systems.

[3] J. M. Peloquin, K. A. Campbell, D. W. Randall, M. A. Evanchik, V. L. Pecoraro, W. H. Armstrong, and R. D. Britt, "55mn endor of the s2-state multiline epr signal of photosystem ii: Implications on the structure of the tetranuclear mn cluster," *Journal of the American Chemical Society*, vol. 122, no. 44, pp. 10926–10942, 2000.

[4] M.-F. Charlot, A. Boussac, and G. Blondin, "Towards a spin coupling model for the mn4 cluster in photosystem ii," *Biochimica et Biophysica Acta (BBA) - Bioenergetics*, vol. 1708, no. 1, pp. 120 – 132, 2005.

[5] L. V. Kulik, B. Epel, W. Lubitz, and J. Messinger, "55mn pulse endor at 34 ghz of the s0 and s2 states of the oxygen-evolving complex in photosystem ii," *Journal of the American Chemical Society*, vol. 127, no. 8, pp. 2392–2393, 2005. PMID: 15724984.

[6] L. Jin, P. Smith, C. J. Noble, R. Stranger, G. R. Hanson, and R. J. Pace, "Electronic structure of the oxygen evolving complex in photosystem ii, as revealed by 55mn davies endor studies at 2.5 k," *Phys. Chem. Chem. Phys.*, vol. 16, pp. 7799–7812, 2014.

[7] N. Cox, M. Retegan, F. Neese, D. A. Pantazis, A. Boussac, and W. Lubitz, "Electronic structure of the oxygen-evolving complex in photosystem ii prior to o-o bond formation," *Science*, vol. 345, no. 6198, pp. 804–808, 2014.

[8] B. KOK, B. FORBUSH, and M. McGLOIN, "Cooperation of charges in photosynthetic o2 evolution-i. a linear four step mechanism," *Photochemistry and Photobiology*, vol. 11, no. 6, pp. 457–475, 1970.

[9] B. FORBUSH, B. KOK, and M. P. McGLOIN, "Cooperation of charges in photosynthetic o2 evolution-ii. damping of flash yield oscillation, deactivation*," *Photochemistry and Photobiology*, vol. 14, no. 3, pp. 307–321, 1971.

[10] Y. Umena, K. Kawakami, J.-R. Shen, and N. Kamiya, "Crystal structure of oxygen-evolving photosystem ii at a resolution of 1.9 ," *Nature*, vol. 473, pp. 55–60, May 2011.

[11] M. Suga, F. Akita, M. Sugahara, M. Kubo, Y. Nakajima, T. Nakane, K. Yamashita, Y. Umena, M. Nakabayashi, T. Yamane, T. Nakano, M. Suzuki, T. Masuda, S. Inoue, T. Kimura, T. Nomura, S. Yonekura, L.-J. Yu, T. Sakamoto, T. Motomura, J.-H. Chen, Y. Kato, T. Noguchi, K. Tono, Y. Joti, T. Kameshima, T. Hatsui, E. Nango, R. Tanaka, H. Naitow, Y. Matsuura, A. Yamashita, M. Yamamoto, O. Nureki, M. Yabashi, T. Ishikawa, S. Iwata, and J.-R. Shen, "Light-induced structural changes and the site of o=o bond formation in psii caught by xfel," *Nature*, vol. 543, pp. 131–135, Feb 2017.

[12] G. Mattioli, P. Giannozzi, A. Amore Bonapasta, and L. Guidoni, "Reaction pathways for oxygen evolution promoted by cobalt catalyst," *Journal of the American Chemical Society*, vol. 135, no. 41, pp. 15353–15363, 2013. PMID: 24044778.

[13] P. F. Smith, L. Hunt, A. B. Laursen, V. Sagar, S. Kaushik, K. U. D. Calvinho, G. Marotta, E. Mosconi, F. De Angelis, and G. C. Dismukes, "Water oxidation by the [co4o4(oac)4(py)4]+ cubium is initiated by oh addition," *Journal of the American Chemical Society*, vol. 137, no. 49, pp. 15460–15468, 2015. PMID: 26593692.

[14] M. Hambourger, G. F. Moore, D. M. Kramer, D. Gust, A. L. Moore, and T. A. Moore, "Biology and technology for photochemical fuel production," *Chem. Soc. Rev.*, vol. 38, pp. 25–35, 2009.

[15] A. W. Rutherford and T. A. Moore, "Mimicking photosynthesis, but just the best bits," *Nature*, vol. 453, pp. 449 EP –, May 2008. Correspondence L3 -.

[16] A. Zouni, H.-T. Witt, J. Kern, P. Fromme, N. Krauss, W. Saenger, and P. Orth, "Crystal structure of photosystem ii from synechococcus elongatus at 3.8 resolution," *Nature*, vol. 409, pp. 739–743, Feb 2001.

[17] N. Kamiya and J.-R. Shen, "Crystal structure of oxygen-evolving photosystem ii from thermosynechococcus vulcanus at 3.7 resolution," *Proceedings of the National Academy of Sciences*, vol. 100, no. 1, pp. 98–103, 2003.

[18] K. N. Ferreira, T. M. Iverson, K. Maghlaoui, J. Barber, and S. Iwata, "Architecture of the photosynthetic oxygen-evolving center," *Science*, vol. 303, no. 5665, pp. 1831–1838, 2004.

[19] B. Loll, J. Kern, W. Saenger, A. Zouni, and J. Biesiadka, "Towards complete cofactor arrangement in the 3.0 resolution structure of photosystem ii," *Nature*, vol. 438, pp. 1040–1044, Dec 2005.

[20] A. Guskov, J. Kern, A. Gabdulkhakov, M. Broser, A. Zouni, and W. Saenger, "Cyanobacterial photosystem ii at 2.9 resolution and the role of quinones, lipids, channels and chloride," *Nat Struct Mol Biol*, vol. 16, pp. 334–342, Mar 2009.

[21] M. Haumann, C. Mller, P. Liebisch, L. Iuzzolino, J. Dittmer, M. Grabolle, T. Neisius, W. Meyer-Klaucke, and H. Dau, "Structural and oxidation state changes of the photosystem ii manganese complex in four transitions of the water oxidation cycle (s0 $\rightarrow$ s1, s1 $\rightarrow$ s2, s2 $\rightarrow$ s3, and s3,4 $\rightarrow$ s0) characterized by x-ray absorption spectroscopy at 20 k and room temperature," *Biochemistry*, vol. 44, no. 6, pp. 1894–1908, 2005. PMID: 15697215.

[22] J. Yano, Y. Pushkar, P. Glatzel, A. Lewis, K. Sauer, J. Messinger, U. Bergmann, and V. Yachandra, "High-resolution mn exafs of the oxygen-evolving complex in photosystem ii: Structural implications for the mn4ca cluster," *Journal of the American Chemical Society*, vol. 127, no. 43, pp. 14974–14975, 2005. PMID: 16248606.

[23] J. Yano, J. Kern, K. Sauer, M. J. Latimer, Y. Pushkar, J. Biesiadka, B. Loll, W. Saenger, J. Messinger, A. Zouni, and V. K. Yachandra, "Where water is oxidized to dioxygen: Structure of the photosynthetic mn4ca cluster," *Science*, vol. 314, no. 5800, pp. 821–825, 2006.

[24] H. Dau, A. Grundmeier, P. Loja, and M. Haumann, "On the structure of the manganese complex of photosystem ii: extended-range exafs data and specific atomic-resolution models for four s-states," *Philosophical Transactions of the Royal Society of London B: Biological Sciences*, vol. 363, no. 1494, pp. 1237–1244, 2008.

[25] G. C. Dismukes and Y. Siderer, "Intermediates of a polynuclear manganese center involved in photosynthetic oxidation of water," *Proc Natl Acad Sci U S A*, vol. 78, pp. 274–278, Jan 1981. 16592949[pmid].

[26] rjan Hansson and L.-E. Andrasson, "Epr-detectable magnetically interacting manganese ions in the photosynthetic oxygen-evolving system after continuous illumination," *Biochimica et Biophysica Acta (BBA) - Bioenergetics*, vol. 679, no. 2, pp. 261 – 268, 1982.

[27] J. C. De Paula and G. W. Brudvig, "Magnetic properties of manganese in the photosynthetic oxygen-evolving complex," *Journal of the American Chemical Society*, vol. 107, no. 9, pp. 2643–2648, 1985.

[28] W. F. Beck, J. C. De Paula, and G. W. Brudvig, "Ammonia binds to the manganese site of the oxygen-evolving complex of photosystem ii in the s2 state," *Journal of the American Chemical Society*, vol. 108, no. 14, pp. 4018–4022, 1986.

[29] D. W. Randall, B. E. Sturgeon, J. A. Ball, G. A. Lorigan, M. K. Chan, M. P. Klein, W. H. Armstrong, and R. D. Britt, "55mn ese-endor of a mixed valence mn(iii)mn(iv) complex: Comparison with the mn cluster of the photosynthetic oxygen-evolving complex," *Journal of the American Chemical Society*, vol. 117, no. 47, pp. 11780–11789, 1995.

[30] A. Boussac, J.-J. Girerd, and A. W. Rutherford, "Conversion of the spin state of the manganese complex in photosystem ii induced by near-infrared light," *Biochemistry*, vol. 35, no. 22, pp. 6984–6989, 1996. PMID: 8679522.

[31] P. Smith and R. Pace, "Evidence for two forms of the g = 4.1 signal in the s2 state of photosystem ii. two magnetically isolated manganese dimers," *Biochimica et Biophysica Acta (BBA) - Bioenergetics*, vol. 1275, no. 3, pp. 213 – 220, 1996.

[32] M. Zheng and G. C. Dismukes, "Orbital configuration of the valence electrons, ligand field symmetry, and manganese oxidation states of the photosynthetic water oxidizing complex: analysis of the s2 state multiline epr signals," *Inorganic Chemistry*, vol. 35, no. 11, pp. 3307–3319, 1996. PMID: 11666533.

[33] A. Boussac, H. Kuhl, S. Un, M. Rgner, and A. W. Rutherford, "Effect of near-infrared light on the s2-state of the manganese complex of photosystem ii from synechococcus elongatus," *Biochemistry*, vol. 37, no. 25, pp. 8995–9000, 1998. PMID: 9636042.

[34] A. Boussac, S. Un, O. Horner, and A. W. Rutherford, "High-spin states ($s \geq 5/2$) of the photosystem ii manganese complex," *Biochemistry*, vol. 37, no. 12, pp. 4001–4007, 1998. PMID: 9565450.

[35] J. M. Peloquin and R. Britt, "Epr/endor characterization of the physical and electronic structure of the oec mn cluster," *Biochimica et Biophysica Acta (BBA) - Bioenergetics*, vol. 1503, no. 12, pp. 96 – 111, 2001. Photosynthetic water oxidation.

[36] A. Haddy, K. V. Lakshmi, G. W. Brudvig, and H. A. Frank, "Q-band epr of the s(2) state of photosystem ii confirms an $s = 5/2$ origin of the x-band $g = 4.1$ signal," *Biophys J*, vol. 87, pp. 2885–2896, Oct 2004. 40238[PII].

[37] N. Ioannidis, G. Zahariou, and V. Petrouleas, "Trapping of the s2 to s3 state intermediate of the oxygen-evolving complex of photosystem ii," *Biochemistry*, vol. 45, no. 20, pp. 6252–6259, 2006. PMID: 16700536.

[38] A. Haddy, "Epr spectroscopy of the manganese cluster of photosystem ii," *Photosynthesis Research*, vol. 92, no. 3, pp. 357–368, 2007.

[39] L. V. Kulik, B. Epel, W. Lubitz, and J. Messinger, "Electronic structure of the mn4oxca cluster in the s0 and s2 states of the oxygen-evolving complex of photosystem ii based on pulse 55mn-endor and epr spectroscopy," *Journal of the American Chemical Society*, vol. 129, no. 44, pp. 13421–13435, 2007. PMID: 17927172.

[40] A. Boussac, M. Sugiura, A. W. Rutherford, and P. Dorlet, "Complete epr spectrum of the s3-state of the oxygen-evolving photosystem ii," *Journal of the American Chemical Society*, vol. 131, no. 14, pp. 5050–5051, 2009.

[41] N. Cox, L. Rapatskiy, J.-H. Su, D. A. Pantazis, M. Sugiura, L. Kulik, P. Dorlet, A. W. Rutherford, F. Neese, A. Boussac, W. Lubitz, and J. Messinger, "Effect of ca2+/sr2+ substitution on the electronic structure of the oxygen-evolving complex of photosystem ii: A combined multifrequency epr, 55mn-endor, and dft study of the s2 state," *Journal of the American Chemical Society*, vol. 133, no. 10, pp. 3635–3648, 2011. PMID: 21341708.

[42] J.-H. Su, N. Cox, W. Ames, D. A. Pantazis, L. Rapatskiy, T. Lohmiller, L. V. Kulik, P. Dorlet, A. W. Rutherford, F. Neese, A. Boussac, W. Lubitz, and J. Messinger, "The electronic structures of the s2 states of the oxygen-evolving complexes of photosystem ii in plants and cyanobacteria in the presence and absence of methanol," *Biochimica et Biophysica Acta (BBA) - Bioenergetics*, vol. 1807, no. 7, pp. 829 – 840, 2011.

[43] L. Rapatskiy, N. Cox, A. Savitsky, W. M. Ames, J. Sander, M. M. Nowaczyk, M. Rgner, A. Boussac, F. Neese, J. Messinger, and W. Lubitz, "Detection of the

water-binding sites of the oxygen-evolving complex of photosystem ii using w-band 17o electronelectron double resonance-detected nmr spectroscopy," *Journal of the American Chemical Society*, vol. 134, no. 40, pp. 16619–16634, 2012. PMID: 22937979.

[44] P. E. M. Siegbahn, "Oo bond formation in the s4 state of the oxygen-evolving complex in photosystem ii," *Chemistry A European Journal*, vol. 12, no. 36, pp. 9217–9227, 2006.

[45] A. R. Jaszewski, S. Petrie, R. J. Pace, and R. Stranger, "Toward the assignment of the manganese oxidation pattern in the water-oxidizing complex of photosystem ii: A time-dependent dft study of xanes energies," *Chemistry A European Journal*, vol. 17, no. 20, pp. 5699–5713, 2011.

[46] S. Luber, I. Rivalta, Y. Umena, K. Kawakami, J.-R. Shen, N. Kamiya, G. W. Brudvig, and V. S. Batista, "S1-state model of the o2-evolving complex of photosystem ii," *Biochemistry*, vol. 50, no. 29, pp. 6308–6311, 2011. PMID: 21678908.

[47] D. A. Pantazis, W. Ames, N. Cox, W. Lubitz, and F. Neese, "Two interconvertible structures that explain the spectroscopic properties of the oxygen-evolving complex of photosystemii in the s2 state," *Angewandte Chemie International Edition*, vol. 51, no. 39, pp. 9935–9940, 2012.

[48] D. R. Kolling, N. Cox, G. M. Ananyev, R. J. Pace, and C. G. Dismukes, "What are the oxidation states of manganese required to catalyze photosynthetic water oxidation?," *Biophysical Journal*, vol. 103, no. 2, pp. 313 – 322, 2012.

[49] L. Zaltsman, G. M. Ananyev, E. Bruntrager, and G. C. Dismukes, "Quantitative kinetic model for photoassembly of the photosynthetic water oxidase from its inorganic constituents: requirements for manganese and calcium in the kinetically resolved steps,," *Biochemistry*, vol. 36, no. 29, pp. 8914–8922, 1997. PMID: 9220979.

[50] W. Hillier and T. Wydrzynski, "Oxygen ligand exchange at metal sites implications for the o2 evolving mechanism of photosystem ii," *Biochimica et Biophysica Acta (BBA) - Bioenergetics*, vol. 1503, no. 1, pp. 197 – 209, 2001. Photosynthetic water oxidation.

[51] T. Kuntzleman and C. F. Yocum, "Reduction-induced inhibition and mn(ii) release from the photosystem ii oxygen-evolving complex by hydroquinone or nh2oh are consistent with a mn(iii)/mn(iii)/mn(iv)/mn(iv) oxidation state for the dark-adapted enzyme," *Biochemistry*, vol. 44, no. 6, pp. 2129–2142, 2005. PMID: 15697239.

[52] J. Messinger, "Evaluation of different mechanistic proposals for water oxidation in photosynthesis on the basis of mn4oxca structures for the catalytic site and spectroscopic data," *Phys. Chem. Chem. Phys.*, vol. 6, pp. 4764–4771, 2004.

[53] G. C. Dismukes, K. Ferris, and P. Watnick, "Epr spectroscopic evidence for a tetranuclear manganese cluster as the site for photosynthetic oxygen evolution," *Photobiochemistry and Photobiophysics*, vol. 3, pp. 243–256, 1982.

[54] D. J. Vinyard, G. M. Ananyev, and G. C. Dismukes, "Photosystem ii: The reaction center of oxygenic photosynthesis," *Annual Review of Biochemistry*, vol. 82, no. 1, pp. 577–606, 2013. PMID: 23527694.

[55] W. Ames, D. A. Pantazis, V. Krewald, N. Cox, J. Messinger, W. Lubitz, and F. Neese, "Theoretical evaluation of structural models of the s2 state in the oxygen evolving complex of photosystem ii: Protonation states and magnetic interactions," *Journal of the American Chemical Society*, vol. 133, no. 49, pp. 19743–19757, 2011. PMID: 22092013.

[56] A. Galstyan, A. Robertazzi, and E. W. Knapp, "Oxygen-evolving mn cluster in photosystem ii: The protonation pattern and oxidation state in the high-resolution crystal structure," *Journal of the American Chemical Society*, vol. 134, no. 17, pp. 7442–7449, 2012. PMID: 22489676.

[57] A. Grundmeier and H. Dau, "Structural models of the manganese complex of photosystem ii and mechanistic implications," *Biochimica et Biophysica Acta (BBA) - Bioenergetics*, vol. 1817, no. 1, pp. 88 – 105, 2012. Photosystem II.

[58] M. Suga, F. Akita, K. Hirata, G. Ueno, H. Murakami, Y. Nakajima, T. Shimizu, K. Yamashita, M. Yamamoto, H. Ago, and J.-R. Shen, "Native structure of photosystem ii at 1.95 resolution viewed by femtosecond x-ray pulses," *Nature*, vol. 517, pp. 99–103, Jan 2015. Letter.

[59] C. Glckner, J. Kern, M. Broser, A. Zouni, V. Yachandra, and J. Yano, "Structural changes of the oxygen-evolving complex in photosystem ii during the catalytic cycle," *Journal of Biological Chemistry*, vol. 288, no. 31, pp. 22607–22620, 2013.

[60] H. Dau, P. Liebisch, and M. Haumann, "X-ray absorption spectroscopy to analyze nuclear geometry and electronic structure of biological metal centers—potential and questions examined with special focus on the tetra-nuclear manganese complex of oxygenic photosynthesis," *Analytical and Bioanalytical Chemistry*, vol. 376, pp. 562–583, Jul 2003.

[61] P. Gatt, S. Petrie, R. Stranger, and R. J. Pace, "Rationalizing the 1.9 crystal structure of photosystem ii–a remarkable jahn–teller balancing act induced by a single proton transfer," *Angewandte Chemie International Edition*, vol. 51, no. 48, pp. 12025–12028, 2012.

[62] S. Petrie, R. J. Pace, and R. Stranger, "Resolving the differences between the 1.9 and 1.95 crystal structures of photosystem ii: A single proton relocation defines two tautomeric forms of the water-oxidizing complex," *Angewandte Chemie International Edition*, vol. 54, no. 24, pp. 7120–7124, 2015.

[63] M. Shoji, H. Isobe, S. Yamanaka, M. Suga, F. Akita, J.-R. Shen, and K. Yamaguchi, "Theoretical studies of the damage-free s1 structure of the camn4o5 cluster in oxygen-evolving complex of photosystem ii," *Chemical Physics Letters*, vol. 623, pp. 1 – 7, 2015.

[64] N. M. Atherton, *Principles of Electron Spin Resonance*. Prentice Hall, New York, 1993.

[65] D. Koulougliotis, D. J. Hirsh, and G. W. Brudvig, "The oxygen-evolving center of photosystem ii is diamagnetic in the s1 resting state," *Journal of the American Chemical Society*, vol. 114, no. 21, pp. 8322–8323, 1992.

[66] S. L. Dexheimer and M. P. Klein, "Detection of a paramagnetic intermediate in the s1 state of the photosynthetic oxygen-evolving complex," *Journal of the American Chemical Society*, vol. 114, no. 8, pp. 2821–2826, 1992.

[67] K. A. Campbell, W. Gregor, D. P. Pham, J. M. Peloquin, R. J. Debus, and R. D. Britt, "The 23 and 17 kda extrinsic proteins of photosystem ii modulate the magnetic properties of the s1-state manganese cluster," *Biochemistry*, vol. 37, no. 15, pp. 5039–5045, 1998. PMID: 9548734.

[68] J. L. Casey and K. Sauer, "Epr detection of a cryogenically photogenerated intermediate in photosynthetic oxygen evolution," *Biochimica et Biophysica Acta (BBA) - Bioenergetics*, vol. 767, no. 1, pp. 21 – 28, 1984.

[69] J. C. de Paula, W. F. Beck, A.-F. Miller, R. B. Wilson, and G. W. Brudvig, "Studies of the manganese site of photosystem ii by electron spin resonance spectroscopy," *J. Chem. Soc., Faraday Trans. 1*, vol. 83, pp. 3635–3651, 1987.

[70] J. Messinger, J. H. Robblee, U. Bergmann, C. Fernandez, P. Glatzel, H. Visser, R. M. Cinco, K. L. McFarlane, E. Bellacchio, S. A. Pizarro, S. P. Cramer, K. Sauer, M. P. Klein, and V. K. Yachandra, "Absence of mn-centered oxidation in the s(2) - s(3) transition: Implications for the mechanism of photosynthetic water oxidation," *J Am Chem Soc*, vol. 123, pp. 7804–7820, Aug 2001. 11493054[pmid].

[71] P. Glatzel, J. Yano, U. Bergmann, H. Visser, J. H. Robblee, W. Gu, F. M. de Groot, S. P. Cramer, and V. K. Yachandra, "Resonant inelastic x-ray scattering (rixs) spectroscopy at the mn k absorption pre-edge–a direct probe of the 3d orbitals," *J Phys Chem Solids*, vol. 66, pp. 2163–2167, Dec 2005. 25308999[pmid].

[72] I. Zaharieva, P. Chernev, G. Berggren, M. Anderlund, S. Styring, H. Dau, and M. Haumann, "Room-temperature energy-sampling k x-ray emission spectroscopy of the mn4ca complex of photosynthesis reveals three manganese-centered oxidation steps and suggests a coordination change prior to o2 formation," *Biochemistry*, vol. 55, no. 30, pp. 4197–4211, 2016. PMID: 27377097.

[73] J. P. McEvoy and G. W. Brudvig, "Structure-based mechanism of photosynthetic water oxidation," *Phys. Chem. Chem. Phys.*, vol. 6, pp. 4754–4763, 2004.

[74] E. M. Sproviero, J. A. Gascon, J. P. McEvoy, G. W. Brudvig, and V. S. Batista, "Characterization of synthetic oxomanganese complexes and the inorganic core of the o2-evolving complex in photosystem ii: Evaluation of the dft/b3lyp level of theory," *Journal of Inorganic Biochemistry*, vol. 100, no. 4, pp. 786 – 800, 2006. High-valent iron intermediates in biologyHigh-valent iron intermediates in biology.

[75] Y. Pushkar, J. Yano, K. Sauer, A. Boussac, and V. K. Yachandra, "Structural changes in the mn4ca cluster and the mechanism of photosynthetic water splitting," *Proceedings of the National Academy of Sciences*, vol. 105, no. 6, pp. 1879–1884, 2008.

[76] T. Saito, S. Yamanaka, K. Kanda, H. Isobe, Y. Takano, Y. Shigeta, Y. Umena, K. Kawakami, J.-R. Shen, N. Kamiya, M. Okumura, M. Shoji, Y. Yoshioka, and K. Yamaguchi, "Possible mechanisms of water splitting reaction based on proton and electron release pathways revealed for camn4o5 cluster of psii refined to 1.9 x-ray resolution," *International Journal of Quantum Chemistry*, vol. 112, no. 1, pp. 253–276, 2012.

[77] M. Kusunoki, "Mono-manganese mechanism of the photosytem ii water splitting reaction by a unique mn4ca cluster," *Biochimica et Biophysica Acta (BBA) - Bioenergetics*, vol. 1767, no. 6, pp. 484 – 492, 2007. Structure and Function of Photosystems.

[78] M. Kusunoki, "S1-state mn4ca complex of photosystem {II} exists in equilibrium between the two most-stable isomeric substates: {XRD} and {EXAFS} evidence," *Journal of Photochemistry and Photobiology B: Biology*, vol. 104, no. 12, pp. 100 – 110, 2011. Special Issue on Recent Progress in the Studies of Structure and Function of Photosystem {II}.

[79] S. Yamanaka, H. Isobe, K. Kanda, T. Saito, Y. Umena, K. Kawakami, J.-R. Shen, N. Kamiya, M. Okumura, H. Nakamura, and K. Yamaguchi, "Possible mechanisms for the o-o bond formation in oxygen evolution reaction at the camn4o5(h2o)4 cluster of psii refined to 1.9 x-ray resolution," *Chemical Physics Letters*, vol. 511, pp. 138–145, 7 2011.

[80] P. E. M. Siegbahn, "Structures and energetics for o2 formation in photosystem ii," *Accounts of Chemical Research*, vol. 42, no. 12, pp. 1871–1880, 2009. PMID: 19856959.

[81] G. C. Dismukes, R. Brimblecombe, G. A. N. Felton, R. S. Pryadun, J. E. Sheats, L. Spiccia, and G. F. Swiegers, "Development of bioinspired mn4o4-cubane water oxidation catalysts: Lessons from photosynthesis," *Accounts of Chemical Research*, vol. 42, no. 12, pp. 1935–1943, 2009. PMID: 19908827.

[82] R. Pal, C. F. A. Negre, L. Vogt, R. Pokhrel, M. Z. Ertem, G. W. Brudvig, and V. S. Batista, "S0-state model of the oxygen-evolving complex of photosystem ii," *Biochemistry*, vol. 52, no. 44, pp. 7703–7706, 2013. PMID: 24125018.

[83] D. Bovi, D. Narzi, and L. Guidoni, "The s2 state of the oxygen-evolving complex of photosystem ii explored by qm/mm dynamics: Spin surfaces and metastable states suggest a reaction path towards the s3 state," *Angewandte Chemie International Edition*, vol. 52, no. 45, pp. 11744–11749, 2013.

[84] M. Retegan, F. Neese, and D. A. Pantazis, "Convergence of qm/mm and cluster models for the spectroscopic properties of the oxygen-evolving complex in photosystem ii," *Journal of Chemical Theory and Computation*, vol. 9, no. 8, pp. 3832–3842, 2013. PMID: 26584129.

[85] F. Neese, "The orca program system," *Wiley Interdisciplinary Reviews: Computational Molecular Science*, vol. 2, no. 1, pp. 73–78, 2012.

[86] J. P. Perdew, "Erratum: Density-functional approximation for the correlation energy of the inhomogeneous electron gas," *Phys. Rev. B*, vol. 34, pp. 7406–7406, Nov 1986.

[87] M. Orio, D. A. Pantazis, and F. Neese, "Density functional theory," *Photosynthesis Research*, vol. 102, no. 2, pp. 443–453, 2009.

[88] F. Weigend and R. Ahlrichs, "Balanced basis sets of split valence, triple zeta valence and quadruple zeta valence quality for h to rn: Design and assessment of accuracy," *Phys. Chem. Chem. Phys.*, vol. 7, pp. 3297–3305, 2005.

[89] F. Weigend, "Accurate coulomb-fitting basis sets for h to rn," *Phys. Chem. Chem. Phys.*, vol. 8, pp. 1057–1065, 2006.

[90] A. Klamt and G. Schuurmann, "Cosmo: a new approach to dielectric screening in solvents with explicit expressions for the screening energy and its gradient," *J. Chem. Soc., Perkin Trans. 2*, pp. 799–805, 1993.

[91] A. Schfer, H. Horn, and R. Ahlrichs, "Fully optimized contracted gaussian basis sets for atoms li to kr," *The Journal of Chemical Physics*, vol. 97, no. 4, pp. 2571–2577, 1992.

[92] A. Schfer, C. Huber, and R. Ahlrichs, "Fully optimized contracted gaussian basis sets of triple zeta valence quality for atoms li to kr," *The Journal of Chemical Physics*, vol. 100, no. 8, pp. 5829–5835, 1994.

[93] A. W. Gtz, M. A. Clark, and R. C. Walker, "An extensible interface for qm/mm molecular dynamics simulations with amber," *Journal of Computational Chemistry*, vol. 35, no. 2, pp. 95–108, 2014.

[94] W. L. Jorgensen, J. Chandrasekhar, J. D. Madura, R. W. Impey, and M. L. Klein, "Comparison of simple potential functions for simulating liquid water," *The Journal of Chemical Physics*, vol. 79, no. 2, pp. 926–935, 1983.

[95] J. A. Maier, C. Martinez, K. Kasavajhala, L. Wickstrom, K. E. Hauser, and C. Simmerling, "ff14sb: Improving the accuracy of protein side chain and backbone parameters from ff99sb," *Journal of Chemical Theory and Computation*, vol. 11, no. 8, pp. 3696–3713, 2015. PMID: 26574453.

[96] S. C. Hoops, K. W. Anderson, and K. M. Merz, "Force field design for metalloproteins," *Journal of the American Chemical Society*, vol. 113, no. 22, pp. 8262–8270, 1991.

[97] H. J. C. Berendsen, J. P. M. Postma, W. F. van Gunsteren, A. DiNola, and J. R. Haak, "Molecular dynamics with coupling to an external bath," *The Journal of Chemical Physics*, vol. 81, no. 8, pp. 3684–3690, 1984.

[98] P. E. M. Siegbahn, "Water oxidation energy diagrams for photosystem ii for different protonation states, and the effect of removing calcium," *Phys. Chem. Chem. Phys.*, vol. 16, pp. 11893–11900, 2014.

[99] M. Askerka, D. J. Vinyard, J. Wang, G. W. Brudvig, and V. S. Batista, "Analysis of the radiation-damage-free x-ray structure of photosystem ii in light of exafs and qm/mm data," *Biochemistry*, vol. 54, no. 9, pp. 1713–1716, 2015. PMID: 25710258.

[100] R. Chatterjee, G. Han, J. Kern, S. Gul, F. D. Fuller, A. Garachtchenko, I. D. Young, T.-C. Weng, D. Nordlund, R. Alonso-Mori, U. Bergmann, D. Sokaras, M. Hatakeyama, V. K. Yachandra, and J. Yano, "Structural changes correlated with magnetic spin state isomorphism in the s2 state of the mn4cao5 cluster in the oxygen-evolving complex of photosystem ii," *Chem. Sci.*, vol. 7, pp. 5236–5248, 2016.

[101] J.-Z. Wu, F. De Angelis, T. G. Carrell, G. P. A. Yap, J. Sheats, R. Car, and G. C. Dismukes, "Tuning the photoinduced o2-evolving reactivity of mn4o47+, mn4o46+, and mn4o3(oh)6+ manganeseoxo cubane complexes," *Inorganic Chemistry*, vol. 45, no. 1, pp. 189–195, 2006. PMID: 16390055.

[102] R. Terrett, S. Petrie, R. Stranger, and R. J. Pace, "What computational chemistry and magnetic resonance reveal concerning the oxygen evolving centre in photosystem ii," *Journal of Inorganic Biochemistry*, vol. 162, pp. 178 – 189, 2016.

[103] A. Abragam and B. Bleaney, *Electron Paramagnetic Resonance of Transition Ions*. Clarendon Press, Oxford, 1970.

[104] A. Bencini and D. Gatteschi, *Electron Paramagnetic Resonance of Exchange Coupled Systems*. Springer, Berlin, Heidelberg, 1990.

[105] F. E. Mabbs and D. Collison, *Electron Paramagnetic Resonance of d Transition Metal Compounds*. Elsevier, Amsterdam, 1992.

[106] L. Noodleman, "Valence bond description of antiferromagnetic coupling in transition metal dimers," *The Journal of Chemical Physics*, vol. 74, no. 10, pp. 5737–5743, 1981.

[107] L. Noodleman, D. A. Case, and A. Aizman, "Broken symmetry analysis of spin coupling in iron-sulfur clusters," *Journal of the American Chemical Society*, vol. 110, no. 4, pp. 1001–1005, 1988.

[108] M. Zheng, S. V. Khangulov, G. C. Dismukes, and V. V. Barynin, "Electronic structure of dimanganese(ii,iii) and dimanganese(iii,iv) complexes and dimanganese catalase enzyme: a general epr spectral simulation approach," *Inorganic Chemistry*, vol. 33, no. 2, pp. 382–387, 1994.

[109] S. Sinnecker, F. Neese, L. Noodleman, and W. Lubitz, "Calculating the electron paramagnetic resonance parameters of exchange coupled transition metal complexes using broken symmetry density functional theory: application to a mniii/mniv model compound," *Journal of the American Chemical Society*, vol. 126, no. 8, pp. 2613–2622, 2004. PMID: 14982471.

[110] S. Schinzel, J. Schraut, A. Arbuznikov, P. Siegbahn, and M. Kaupp, "Density functional calculations of 55mn, 14n and 13c electron paramagnetic resonance parameters support an energetically feasible model system for the s2 state of the

oxygen-evolving complex of photosystem ii," *Chemistry A European Journal*, vol. 16, no. 34, pp. 10424–10438, 2010.

[111] K.-O. Schfer, R. Bittl, W. Zweygart, F. Lendzian, G. Haselhorst, T. Weyhermller, K. Wieghardt, and W. Lubitz, "Electronic structure of antiferromagnetically coupled dinuclear manganese (mniiimniv) complexes studied by magnetic resonance techniques," *Journal of the American Chemical Society*, vol. 120, no. 50, pp. 13104–13120, 1998.

[112] T. Lohmiller, W. Ames, W. Lubitz, N. Cox, and S. K. Misra, "Epr spectroscopy and the electronic structure of the oxygen-evolving complex of photosystem ii," *Applied Magnetic Resonance*, vol. 44, pp. 691–720, Jun 2013.

[113] D. A. Pantazis, M. Orio, T. Petrenko, S. Zein, W. Lubitz, J. Messinger, and F. Neese, "Structure of the oxygen-evolving complex of photosystem ii: information on the s2 state through quantum chemical calculation of its magnetic properties," *Phys. Chem. Chem. Phys.*, vol. 11, pp. 6788–6798, 2009.

[114] D. Pantazis, M. Orio, T. Petrenko, S. Zein, E. Bill, W. Lubitz, J. Messinger, and F. Neese, "A new quantum chemical approach to the magnetic properties of oligonuclear transition-metal complexes: Application to a model for the tetranuclear manganese cluster of photosystemii," *Chemistry A European Journal*, vol. 15, no. 20, pp. 5108–5123, 2009.

[115] V. N. Staroverov, G. E. Scuseria, J. Tao, and J. P. Perdew, "Comparative assessment of a new nonempirical density functional: Molecules and hydrogen-bonded complexes," *The Journal of Chemical Physics*, vol. 119, no. 23, pp. 12129–12137, 2003.

[116] F. Neese, F. Wennmohs, A. Hansen, and U. Becker, "Efficient, approximate and parallel hartreefock and hybrid dft calculations. a chain-of-spheres algorithm for the hartreefock exchange," *Chemical Physics*, vol. 356, no. 1, pp. 98 – 109, 2009. Moving Frontiers in Quantum Chemistry:.

[117] F. Neese, "Prediction and interpretation of the 57fe isomer shift in mssbauer spectra by density functional theory," *Inorganica Chimica Acta*, vol. 337, pp. 181 – 192, 2002. Protagonists in Chemistry: Karl Wieghardt.

[118] F. Neese, "Metal and ligand hyperfine couplings in transition metal complexes: The effect of spinorbit coupling as studied by coupled perturbed kohnsham theory," *The Journal of Chemical Physics*, vol. 118, no. 9, pp. 3939–3948, 2003.

[119] P. E. Siegbahn, "Water oxidation mechanism in photosystem ii, including oxidations, proton release pathways, oo bond formation and o2 release," *Biochimica et Biophysica Acta (BBA) - Bioenergetics*, vol. 1827, no. 8, pp. 1003 – 1019, 2013. Metals in Bioenergetics and Biomimetics Systems.

[120] N. Cox, D. A. Pantazis, F. Neese, and W. Lubitz, "Biological water oxidation," *Accounts of Chemical Research*, vol. 46, no. 7, pp. 1588–1596, 2013. PMID: 23506074.

[121] rjan Hansson, R. Aasa, and T. Vnngard, "The origin of the multiline and g = 4.1 electron paramagnetic resonance signals from the oxygen-evolving system of photosystem ii," *Biophysical Journal*, vol. 51, no. 5, pp. 825 – 832, 1987.

[122] G. A. Lorigan and R. D. Britt, "Temperature-dependent pulsed electron paramagnetic resonance studies of the s2 state multiline signal of the photosynthetic oxygen-evolving complex.," *Biochemistry*, vol. 33, no. 40, pp. 12072–12076, 1994. PMID: 7918427.

[123] M. Munzarov and M. Kaupp, "A critical validation of density functional and coupled-cluster approaches for the calculation of epr hyperfine coupling constants in transition metal complexes," *The Journal of Physical Chemistry A*, vol. 103, no. 48, pp. 9966–9983, 1999.

[124] S. Schinzel and M. Kaupp, "Validation of broken-symmetry density functional methods for the calculation of electron paramagnetic resonance parameters of dinuclear mixed-valence mnivmniii complexes," *Canadian Journal of Chemistry*, vol. 87, no. 10, pp. 1521–1539, 2009.

[125] H. Diril, H. R. Chang, M. J. Nilges, X. Zhang, J. A. Potenza, H. J. Schugar, S. S. Isied, and D. N. Hendrickson, "Simulation strategies for unusual epr spectra of binuclear mixed-valence manganese complexes: synthesis, properties, and x-ray structures of the mniimniii complexes [mn2(bpmp)(.mu.-oac)2](clo4)2.cntdot.h2o and [mn2(bcmp)(.mu.-oac)2](clo4)2.cntdot.ch2cl2," *Journal of the American Chemical Society*, vol. 111, no. 14, pp. 5102–5114, 1989.

[126] T. Noguchi, "Ftir detection of water reactions in the oxygen-evolving centre of photosystem ii," *Philos Trans R Soc Lond B Biol Sci*, vol. 363, pp. 1189–1195, Mar 2008. rstb20072214[PII].

[127] I. D. Young, M. Ibrahim, R. Chatterjee, S. Gul, F. D. Fuller, S. Koroidov, A. S. Brewster, R. Tran, R. Alonso-Mori, T. Kroll, T. Michels-Clark, H. Laksmono, R. G. Sierra, C. A. Stan, R. Hussein, M. Zhang, L. Douthit, M. Kubin, C. de Lichtenberg, L. Vo Pham, H. Nilsson, M. H. Cheah, D. Shevela, C. Saracini, M. A. Bean, I. Seuffert, D. Sokaras, T.-C. Weng, E. Pastor, C. Weninger, T. Fransson, L. Lassalle, P. Bräuer, P. Aller, P. T. Docker, B. Andi, A. M. Orville, J. M. Glownia, S. Nelson, M. Sikorski, D. Zhu, M. S. Hunter, T. J. Lane, A. Aquila, J. E. Koglin, J. Robinson, M. Liang, S. Boutet, A. Y. Lyubimov, M. Uervirojnangkoorn, N. W. Moriarty, D. Liebschner, P. V. Afonine, D. G. Waterman, G. Evans, P. Wernet, H. Dobbek, W. I. Weis, A. T. Brunger, P. H. Zwart, P. D. Adams, A. Zouni, J. Messinger, U. Bergmann, N. K. Sauter, J. Kern, V. K. Yachandra, and J. Yano, "Structure of photosystem ii and substrate binding at room temperature," *Nature*, vol. 540, pp. 453–457, Nov 2016.

[128] J. Messinger, M. Badger, and T. Wydrzynski, "Detection of one slowly exchanging substrate water molecule in the s3 state of photosystem ii.," *Proceedings of the National Academy of Sciences*, vol. 92, no. 8, pp. 3209–3213, 1995.

[129] W. Hillier, J. Messinger, and T. Wydrzynski, "Kinetic determination of the fast exchanging substrate water molecule in the s3 state of photosystem ii,," *Biochemistry*, vol. 37, no. 48, pp. 16908–16914, 1998. PMID: 9836583.

[130] W. Hillier and T. Wydrzynski, "The affinities for the two substrate water binding sites in the o2 evolving complex of photosystem ii vary independently during s-state turnover," *Biochemistry*, vol. 39, no. 15, pp. 4399–4405, 2000. PMID: 10757989.

[131] G. Hendry and T. Wydrzynski, "The two substratewater molecules are already bound to the oxygen-evolving complex in the s2 state of photosystem ii," *Biochemistry*, vol. 41, no. 44, pp. 13328–13334, 2002. PMID: 12403635.

[132] G. Hendry and T. Wydrzynski, "18o isotope exchange measurements reveal that calcium is involved in the binding of one substrate-water molecule to the oxygen-evolving complex in photosystem ii," *Biochemistry*, vol. 42, no. 20, pp. 6209–6217, 2003. PMID: 12755624.

[133] W. Hillier and T. Wydrzynski, "Substrate water interactions within the photosystem ii oxygen evolving complex," *Phys. Chem. Chem. Phys.*, vol. 6, pp. 4882–4889, 2004.

[134] H. Nilsson, T. Krupnik, J. Kargul, and J. Messinger, "Substrate water exchange in photosystem ii core complexes of the extremophilic red alga cyanidioschyzon merolae," *Biochimica et Biophysica Acta (BBA) - Bioenergetics*, vol. 1837, no. 8, pp. 1257 – 1262, 2014.

[135] S. Petrie, R. Stranger, and R. J. Pace, "Rationalizing the 2.25 resolution crystal structure of the water oxidising complex of photosystemii in the s3 state," *ChemPhysChem*, vol. 18, no. 20, pp. 2924–2931, 2017.

[136] X. Li and P. E. M. Siegbahn, "Alternative mechanisms for o2 release and o-o bond formation in the oxygen evolving complex of photosystem ii," *Phys. Chem. Chem. Phys.*, vol. 17, pp. 12168–12174, 2015.

[137] M. Retegan, V. Krewald, F. Mamedov, F. Neese, W. Lubitz, N. Cox, and D. A. Pantazis, "A five-coordinate mn(iv) intermediate in biological water oxidation: spectroscopic signature and a pivot mechanism for water binding," *Chem. Sci.*, vol. 7, pp. 72–84, 2016.

[138] M. Haumann, P. Liebisch, C. Müller, M. Barra, M. Grabolle, and H. Dau, "Photosynthetic o2 formation tracked by time-resolved x-ray experiments," *Science*, vol. 310, no. 5750, pp. 1019–1021, 2005.

[139] A. Klauss, M. Haumann, and H. Dau, "Alternating electron and proton transfer steps in photosynthetic water oxidation," *Proceedings of the National Academy of Sciences*, vol. 109, no. 40, pp. 16035–16040, 2012.

[140] H. Suzuki, M. Sugiura, and T. Noguchi, "Monitoring water reactions during the s-state cycle of the photosynthetic water-oxidizing center: Detection of the dod bending vibrations by means of fourier transform infrared spectroscopy," *Biochemistry*, vol. 47, no. 42, pp. 11024–11030, 2008. PMID: 18821774.

[141] X. Liu and F. Wang, "Transition metal complexes that catalyze oxygen formation from water: 19792010," *Coordination Chemistry Reviews*, vol. 256, no. 11, pp. 1115 – 1136, 2012.

[142] H. Dau, C. Limberg, T. Reier, M. Risch, S. Roggan, and P. Strasser, "The mechanism of water oxidation: From electrolysis via homogeneous to biological catalysis," *ChemCatChem*, vol. 2, no. 7, pp. 724–761.

[143] S. Berardi, G. La Ganga, M. Natali, I. Bazzan, F. Puntoriero, A. Sartorel, F. Scandola, S. Campagna, and M. Bonchio, "Photocatalytic water oxidation: Tuning light-induced electron transfer by molecular co4o4 cores," *Journal of the American Chemical Society*, vol. 134, no. 27, pp. 11104–11107, 2012. PMID: 22716164.

[144] N. S. McCool, D. M. Robinson, J. E. Sheats, and G. C. Dismukes, "A co4o4 cubane water oxidation catalyst inspired by photosynthesis," *Journal of the American Chemical Society*, vol. 133, no. 30, pp. 11446–11449, 2011. PMID: 21739983.

[145] P. F. Smith, C. Kaplan, J. E. Sheats, D. M. Robinson, N. S. McCool, N. Mezle, and G. C. Dismukes, "What determines catalyst functionality in molecular water oxidation? dependence on ligands and metal nuclearity in cobalt clusters," *Inorganic Chemistry*, vol. 53, no. 4, pp. 2113–2121, 2014. PMID: 24498959.

[146] M. Haumann, O. Bögershausen, D. Cherepanov, R. Ahlbrink, and W. Junge, "Photosynthetic oxygen evolution: H/d isotope effects and the coupling between electron and proton transfer during the redox reactions at the oxidizing side of photosystem ii," *Photosynthesis Research*, vol. 51, pp. 193–208, Mar 1997.